N72-13861

NASA CR-72800
SRI-R-59

FINAL REPORT

METEOROID-BUMPER INTERACTIONS PROGRAM

by

P. S. GOUGH

Prepared for

NATIONAL AERONAUTICS AND SPACE ADMINISTRATION

NOVEMBER 1970

Contract NAS 3-10299

SPACE RESEARCH INSTITUTE
2055 Peel Street Suite 175
Montreal, Canada

Requests for copies of this report should be referred to

National Aeronautics & Space Administration
Scientific and Technical Information Facility
P. O. Box 33
College Park, Md. 20740

SRI-R-59

NASA CR-72800

FINAL REPORT

METEOROID-BUMPER INTERACTIONS PROGRAM

by

P.S. GOUGH

Prepared for

NATIONAL AERONAUTICS AND SPACE ADMINISTRATION

November, 1970

Contract NAS3-10299

Space Research Institute
2055 Peel Street, Suite 175
Montreal, Canada

FOREWORD

This report summarizes a research program at the Space Research Institute in hypervelocity impact and meteoroid-bumper interaction phenomena, conducted during the period September 1967 through December 1969. The program was sponsored by the National Aeronautics and Space Administration under contract NAS3-10299 "Meteoroid-Bumper Interactions Program". The technical monitor for the program was Mr. Gordon T. Smith of NASA Lewis Research Center, Liquid Rocket Technology Branch. The program reported herein has been a continuation and extension of work performed under contracts NAS3-4190 and NAS3-7946 and reviewed in the final reports for those programs, NASA CR-54857 and NASA CR-54848 respectively.

The program reported herein was conducted under the guidance of Mr. W.H. Friend, principal investigator. The author wishes to acknowledge the assistance of Mr. G.W. Kraak and Mr. L. McCourt in the performance of the experimental program and to express his indebtedness to Dr. G.V. Bull for his continued support and guidance throughout the program.

SUMMARY

An investigation has been made of the interaction of meteoroids with shielded structures. The interaction has been simulated by the impact of Lexan cylinders onto lead shields in order to provide the vaporous debris believed to be created by meteoroid impact on a space vehicle.

The investigation has included several different, but related tasks. The first of these has consisted of determining shock compression data for Lexan. This, in combination with the known shock compression data for the lead shield, has permitted the definition of the initial high pressure states in the impacted projectile and shield.

The debris from such impact events has been permitted to interact with aluminum main walls. The walls were chosen to be sufficiently large to be effectively infinite in diameter compared to the loaded area. The thickness of the wall and the spacing from the shield were varied to determine the effect of these parameters. In addition, the effect of having a body of water behind the wall has been assessed. Measurements of the stagnation pressure in the debris cloud have been made and correlated with the response of the main wall.

The response of cryogenic insulation panels to impact debris has been studied. A nominal no-damage threshold has been defined and used with extrapolated debris cloud pressure data to provide design data appropriate to the near-earth environment. The protection provided to the main wall by a face-mounted cryogenic panel has been assessed.

The data from events involving the impacts of Lexan projectiles onto lead grids have been examined and compared with data determined from impacts onto equivalent weight per unit frontal area solid shields. Little difference has been found in the protection potential of solid and perforated shields, indicating that the interference of the shield with the radiation balancing of a vehicle can be reduced without sacrificing protection and with no additional weight penalty. Finally, an attempt has been made to understand the structure of the debris cloud generated by impact onto a Grid-Bumper.

TABLE OF CONTENTS

LIST OF ILLUSTRATIONS

LIST OF ILLUSTRATIONS CONT'D

LIST OF ILLUSTRATIONS CONT'D

LIST OF SYMBOLS

A	constant
c	shock compression constant
c_o	sound speed in undisturbed material
d	projectile diameter
D	shock wave velocity
e	internal energy
E	mission area-time product
E_o	energy release of blast wave
f	non-dimensional pressure
g	non-dimensional internal energy
g_o	gravitational acceleration at earth's surface
h	main wall thickness
h_m	momentum scaled main wall thickness
$h_{B.L.}$	main wall ballistic limit thickness
H	Hugoniot relation
I	impulse, $I = \int p dt$
I^*	non-dimensional total energy integral
j	geometrical parameter
k_j	geometrical parameter
M	projectile mass
M_s	shock wave Mach number
N	cumulative mass flux
p	pressure
p_{max}	maximum center line pressure
$P(n)$	probability of n successes
r	radial coordinate

LIST OF SYMBOLS CONT'D

R_s	radial coordinate of shock front
s	shock compression constant
S	spacing from shield
t	time
T	time of debris cloud loading
T_1, T_2	reference times
u	particle velocity
$uesc,r$	radial escape velocity of debris cloud
$uesc,z$	axial escape velocity of debris cloud
V	impact velocity
z	axial coordinate
β_1,β_2,β_3	function in solution of blast wave problem
γ	polytropic exponent (ratio of specific heats)
Δ	constant in Gaussian distribution
ΔR	radial expansion of debris cloud
Δz	axial expansion of debris cloud
ε_θ	hoop strain
ε_r	radial strain
ε_o	ultimate strain
ξ	similarity variable, $\xi = r/R_s$
ρ	density
ρ_w	density of main wall
σ_o	yield stress
ϕ	non-dimensional velocity
ψ	non-dimensional density

The subscripts 0 and 1 have been used to designate conditions ahead of and behind the shock wave respectively.

A dot over a quantity indicates differentiation with respect to time.

1.0 INTRODUCTION

In the design of space vehicles, an account must be taken of the risk due to meteoroids. This aspect of the design confronts the engineer with several difficulties: the environment is still not well known and the physics which govern the response of the spacecraft structure to impact by a meteoroid are not yet fully understood. Most meteoroids are very small, having masses of the order of 10^{-6} gms, or less. The probability of encountering a large meteoroid (one having a mass of the order of one gram) is very small, in the near-earth environment. However, the expectation of such an impact cannot be neglected when dealing with a vehicle of large area, such as a space station, which is exposed to the environment for a long time. Early investigations have made it clear that protection by pure armor requires very heavy structures for missions involving large area-time products. Alternative solutions have been sought and the concept of a sacrificial exterior skin or shield was first proposed by Whipple (reference 1).

It was suggested by Whipple that a thin shield spaced some distance from the main wall of a space vehicle would completely fragment a fast moving meteoroid and disperse the debris over a large area on the main wall. At the relative impact velocity believed to be typical of meteoroids in the near-earth environment 20 km/sec (65,600 ft/sec), the fragmentation is expected to be complete to the point of total vaporization of the meteoroid together with a local portion of the shield. The ensuing load in the main wall would then be substantially lower than that experienced in direct impact.

It is generally believed that the total weight per unit frontal area required to defeat a sufficiently fast moving meteoroid is less in a double wall structure than in a single wall structure. Clearly this can only be true when the velocity at which the meteoroid impacts the shield is sufficiently high to produce good fragmentation and when the spacing between the shield and the main wall is made sufficiently large to permit expansion of the debris. It is believed that both these requirements can be satisfied in practical structures. The possibility of saving weight in a structure is always attractive to a designer; particularly so when preliminary estimates of the thickness of single wall armor required for lengthy missions indicate excessive weight. Accordingly, considerable attention has been given to the possibility of utilizing double wall structures in space vehicles.

A continuing hypervelocity impact research program directed towards double-wall meteoroid protection systems for space vehicles has been carried out since 1961 at McGill University, the Space Research Institute of McGill University and presently at the Space Research Institute (Quebec) Inc.

The early development of the impact research from the Spring of 1961 to the Spring of 1964 is outlined in the introduction of reference 2. The period June 15, 1964 to September 15, 1965 is reported to the text of reference 2. In reference 3 is given an account of the work performed in the period December 1965 to June 1967. The report presented here covers the period September 1967 until December 1969.

The work reported herein has consisted primarily of experimental investigations into various aspects of hypervelocity impact phenomena. Accordingly, the work has been divided into several different but related tasks. Each major section of the report deals with one such task and each such section is more or less self contained. In addition, we provide some background material in sub sections 1.1 and 1.2.

In section 2.0 we report on testing to define shock compression data for Lexan. A considerable body of such information exists for most metals, ceramics and a large number of plastics (references 4, 5, 6, 7, 8, 9, 10). However, data of this type was lacking for Lexan. Since the bulk of the test projectiles used at SRI has consisted of Lexan cylinders, it was considered desirable to obtain this information, especially where it was required by earlier theoretical investigations (reference 11). Lexan targets were fabricated with metallic sensors which registered the passage of the impact shock wave. Subsequent analysis of the shock trajectory permitted a calculation of the pressure and density in the shocked material.

In section 3.0 of the report we discuss the results of investigations into the nature of the debris cloud and the response of the main wall to the debris. Measurements were made of the detailed distribution of stagnation pressure near the centre of the asymmetric debris cloud. These revealed a departure of the radial distributions of stagnation pressure and impulse from the Gaussian form reported by the coarser measurements of reference 3.

The dependence on spacing from the shield of the ballistic limit thickness of main walls constructed of 2024-T3 aluminum was established for a fixed impact configuration. The ballistic limit thickness was found to vary as the spacing to the -1.67 power and was found to correlate linearly with the total impulse in the centre line of the debris cloud. An explanation for this correlation was advanced by considering energy balancing at the centre of the main wall.

The Beckman and Whitley 192 series framing camera was used to provide quantitative data concerning the response and failure mode of the main wall. It was observed that for main walls fabricated from 2024-T3 aluminum failure occurred only after considerable deformation. Comparison with records of the load history showed that the time to failure was comparable to the loading time.

The effect of having a body of water behind the main wall was studied. The deflection of the main wall when loaded by the debris cloud was found to be greatly reduced. A brief investigation of the ballistic limit thickness indicated that a water backed wall need be approximately one half the thickness of the unsupported wall. However, this conclusion requires further testing over a wide range of impact conditions before it can be accepted as a design recommendation.

In section 4.0 we report on the response of cryogenic insulation panels to debris cloud loading. The panels were of two types, SEMI (Self Evacuated Multilayer Insulation) and aluminized mylar. Both types of panel consisted of alternating layers of high thermal conductivity and low thermal conductivity. Such a structure will then have high conductivity in a direction tangential to its surface and low conductivity normal to its surface. Solar radiation incident on a cryogenic tank shrouded with insulation will be conducted tangentially to the shaded side of the tank where it will be re-radiated into space, thus keeping the fuel cold.

Both types of insulation were found to be capable of sustaining a gaseous debris pulse having a maximum stagnation pressure equal to 63.5 kg/cm^2 (900 psi). The damage changed rapidly at this threshold from complete penetration of the panel to tearing of the outer sheet. Further reduction of the debris load intensity (effected by increasing of the spacing from the shield) produced no further reduction in damage. Particulate penetration was present at all spacings.

Some ballistic limit tests were performed in which the aluminized mylar panels were face-mounted on 2024-T3 aluminum main walls. No detectable protection was provided by the panel when loaded by vaporous debris. The same conclusion was reached when the main wall was supported from behind by a body of water. The resistance of the cryogenic insulation panels as defined by laboratory tests was used together with an extrapolation of the peak cloud pressure into the meteoroid regime to provide design data for cryogenic panels in the near-earth environment.

In section 5.0 we report on an analysis of the direct impact of a projectile onto a main wall supported by a body of water. The projectile was assumed to penetrate the wall completely and the blast wave in the water is analysed by a quasi-similarity technique due to Rae (reference 12). A comparison was made with the experimental data of reference 13 and good agreement was observed when not too close to the shield.

In section 6.0 we evaluate the performance of a Grid-Bumper used as a shield. The Grid-Bumper was suggested in reference 3 as a refinement of the solid shield which would provide less interference with the radiation field. The Grid-Bumpers used in the current studies have been woven out of fine lead wire in such a way as to provide the same mass per unit frontal area as a solid lead shield having a thickness equal to 0.25 mm (0.010 in). The characteristics of the debris formed by impact onto a Grid-Bumper have been evaluated and compared with those typical of the solid shield. Little difference was observed in the maximum cloud stagnation pressures and,as one might therefore expect,in the protection provided to a main wall. The Grid-Bumper was observed to produce a debris cloud having a much greater axial escape velocity than the solid shield. An explanation has been advanced in the form of the interaction of material jetting through the interstitial gaps in the grid. Some substantiation for this theory was provided by the results of a detailed experimental study of the interaction process.

1.1 Simulation of the Debris Cloud Due to Meteoroid Impact

In order to simulate meteoroid impact, it is desirable to select experimental parameters which provide a vaporous debris after the impact event. Consideration of the manner in which the original kinetic energy of the projectile is redistributed among the various energy modes of the projectile and target indicates that a like material impact will only produce fully vaporized debris when the kinetic energy is an order of magnitude greater than the tabulated vaporization energy of the impacting materials. For a discussion of this vaporization requirement, we refer to reference 10.

It is desirable to use a gram sized projectile in order to facilitate observation of the impact phenomena. A gram sized projectile may be easily detected and photographed to verify integrity and orientation. Under the current limitations on the velocity to which gram sized projectiles may be coherently launched (∿10 km/sec (32,800 ft/sec)), the experimentalist must therefore sacrifice other material properties in favor of low vaporization energies, since even at 10 km/sec (32,800 ft/sec) only a few materials may be expected to vaporize upon impact. Lead, cadmium and Lexan polycarbonate have been used extensively in meteoroid simulation studies as these materials are believed to provide vaporous debris at impact velocities of the order of 8 km/sec.

This conclusion is substantiated by the results of pressure probe measurements of debris clouds reported in references 2 and 3.

In figure 1.1(a) we have indicated a pressure probe located on the centre line of the impact event. Figures 1.1(b) through (d) represent various stagnation pressure versus time distributions obtained in the debris cloud under varying impact conditions.

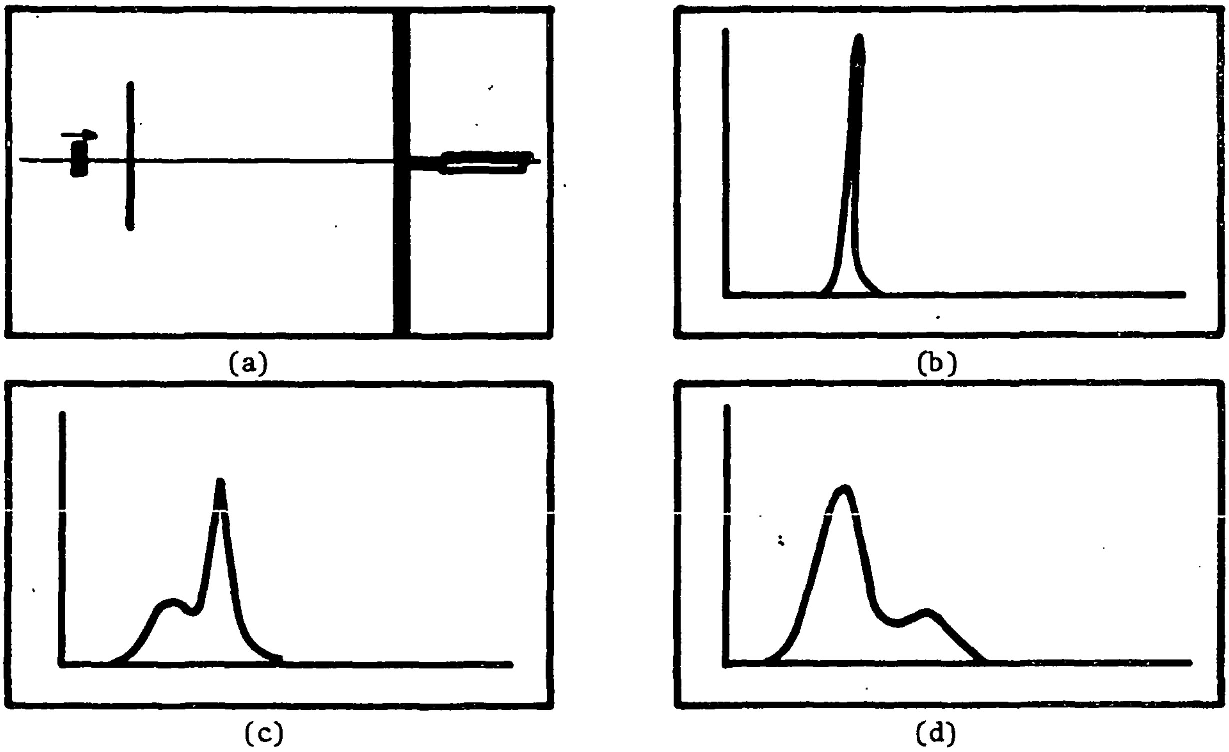

Figure 1.1 Schematic of Centre Line Pressure Pulses in Debris Cloud

When the velocity of the projectile is such that the kinetic energy is less than the tabulated energy of vaporization, the pressure pulse is as in figure 1.1(b). The amplitude is high and the width is perhaps 2 - 3 μsec. Upon increasing the kinetic energy to a level somewhat higher than the vaporization energy, the pulse appears as in figure 1.1(c). Two distinct peaks are visible. The earlier pulse is interpreted as being due to vapor while the later pulse is interpreted as being due to the more slowly moving solid/liquid debris. Further increases in velocity cause the vapor pulse to increase in magnitude at the expense of the solid/liquid pulse until the latter disappears. This condition is reached for a Lexan on lead impact at about 8.5 km/sec (28,000 ft/sec). The ratio of kinetic to tabulated vaporization energy is roughly 7. The relatively low energy ratio requirement is due to the fact that the mismatch between the light projectile and heavy target produces a high internal energy in the projectile at the expense of the shield. This mismatch in internal energy per unit mass is, however, compensated by a similar mismatch in the vaporization energies of Lexan and lead (5.0×10^6 and 0.83×10^6 joules/kg, respectively). We note that the progression of pulses 1.1(b) - 1.1(d) can also be effected by using a high impact velocity and varying the bumper thickness (reference 3). As discussed in reference 14, the thinner target causes more substantial decay of the shock wave in the projectile, lowering the final shocked internal energies below the values required for vaporization.

1.2 Qualitative Response of the Main Wall to Debris Cloud

In considering the response of the main wall to the impact generated debris cloud, one must distinguish between the gaseous and the solid/liquid phases of the cloud. The response of the main wall and the dependence of that response on spacing from the shield can be quite different for the two distinct phases. (We are not distinguishing between the solid fragments and the liquid droplets. They present a similar hazard to the main wall due to a local concentration of momentum within the cloud). Particles may always be expected in the debris due to decay of the radially propagating shock wave in the shield. In addition, particles may be born in the projectile due to underdesign of the shield or because of a low impact velocity.

In figure 1.2 we have indicated a schematic dependence on spacing of the ballistic limit thickness of the main wall. The ballistic limit represents a configuration corresponding to incipient failure of the structure. It is customary to speak of a ballistic limit velocity or a ballistic limit thickness where it is understood that all the other system parameters are held constant while the velocity or the target thickness is varied to bring the structure to incipient failure.

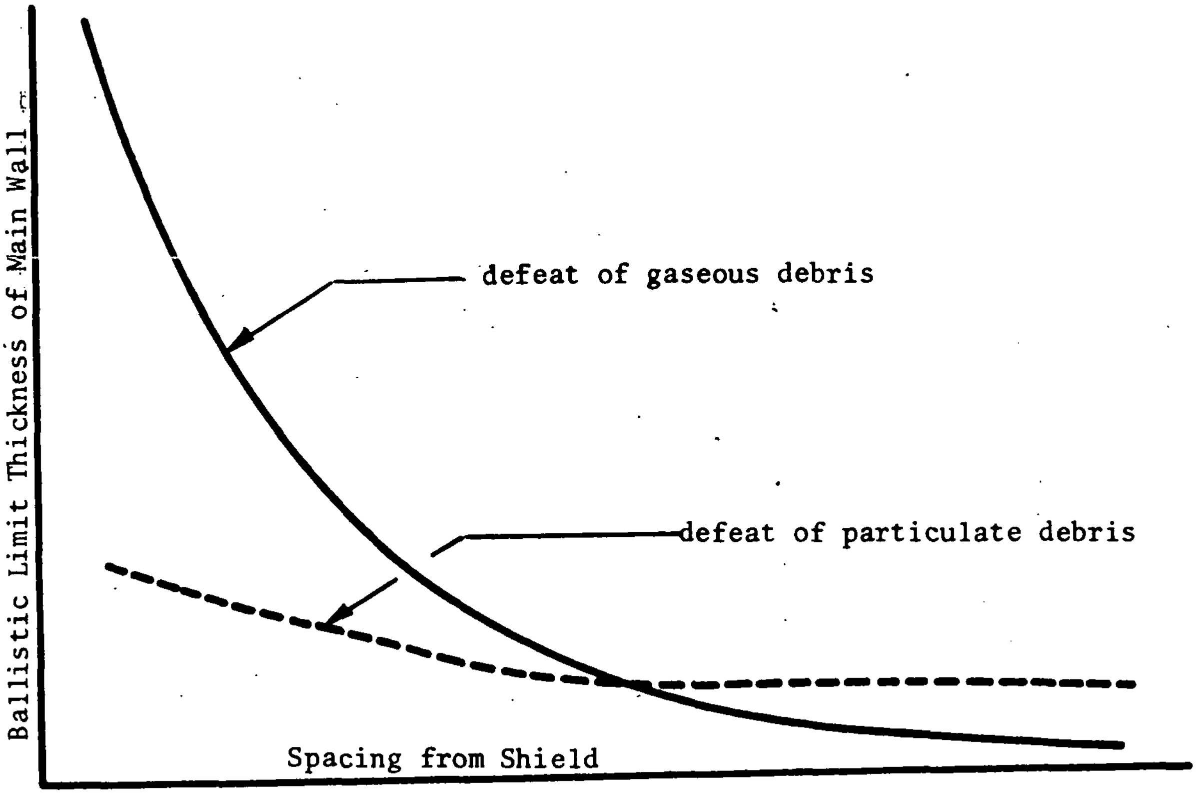

Figure 1.2 Schematic Dependence of Ballistic Limit Thickness of Main Wall on Spacing

The solid line represents defeat of the gaseous debris and the broken line represents defeat of small particles. We expect the hazard presented by the gaseous phase to decrease rapidly with spacing and to approach zero as the spacing becomes large. The main wall is observed to fail in any one of several ways. At very small spacings, the gas has not expanded appreciably, the dynamic pressures are orders of magnitude greater than the strength of the main wall and the loading on the wall is similar to that of a direct impact. Depending on the thickness of the main wall, one may find total perforation (material punch-out), cratering of the surface and/or spallation of the rear surface. Moving further back, the cloud has had time to expand and the dynamic pressures are of the order of the material strength. The wall is accelerated by the rapid deposition of momentum on its surface. Again depending on the wall thickness, bending or membrane stresses dominate and the wall may suffer a large deformation failure.

A different situation exists for the hazard presented by the solid/liquid phase of the cloud. The lethality of the small particles may decrease somewhat over small spacings from the shield. At very small spacings, overlap of individual craters in the sheet will add to the hazard. As the spacing is increased, we expect interaction of the damage patterns to become small so that the particles may be considered separately. The hazard to the main wall will then level off with spacing as the lethality of an individual particle will remain constant. At large spacings, a main wall sufficiently thick to support the loading produced by the gaseous phase may nonetheless fail due to penetration by individual particles. Thus the graph of ballistic limit thickness versus spacing will correspond to the gas curve in figure 1.2 up to the cross over point when the particle curve begins to apply.

The above discussion of main wall response was based on the supposition of a well vaporized debris cloud. If, in fact, the cloud consists entirely of particles in the solid/liquid phases, the ballistic limit thickness will have much the same dependence as that indicated in figure 1.2. The spacing at which the debris becomes constant and the final limiting thickness of the main wall will clearly depend on the size and energy of the constituent particles.

2.0 THE DETERMINATION OF SHOCK COMPRESSION DATA FOR LEXAN

When impact occurs at hypervelocity, shock waves are created which strongly compress even solid materials in the neighborhood of the area of contact. At impact velocities of the order of 10 km/sec, the compression will be roughly two-fold for most solid materials and the stresses associated with the compression will be of the order of 10^7 kg/cm^2 (1.4 x 10^8 psi). An investigation of hypervelocity impact must logically begin with a study of the relations governing the processing of material to these extreme conditions. The maximum difference between the principal stresses that a solid can support is of the order of the yield stress. For most materials the yield stress is of the order of 10^3-10^4 kg/cm^2 (1.4x10^4 - 1.4x10^5 psi). Thus the difference between the principal stresses in the highly compressed state typical of hypervelocity impact is small compared to the magnitude of the stresses themselves. It is customary to ignore the difference and to assume that the principal stresses are equal. This is sometimes referred to as the hydrodynamic analogy in that the highly compressed solid is treated as though it were a fluid.

The basic equations to be studied are the Rankine-Hugoniot conservation relations across a shock wave. The shock wave is regarded, from the macroscopic point of view, as a mathematical surface across which the mechanical and thermodynamic state of the fluid may change in a discontinuous manner. In reality, the shock wave has a finite thickness which is determined by the relaxation mechanisms in the fluid. In the frame of reference of the shock wave, fluid is seen to approach the wave front with high mechanical and low internal energy.

At the shock front the material exchanges the mechanical for internal energy and is seen to recede from the shock wave with low mechanical and high internal energy. Thus material crossing the shock front is retarded and the thickness of the surface is determined by the rate of processes which largely randomize the orderly motion of the influx to produce thermal energy at the expense of the kinetic energy. In a gas the parameter of length associated with the fundamental intermolecular forces is the mean free path and the thickness of the shock front is found to be, both theoretically and experimentally, of the order of a few mean free paths (references 15, 16). Under normal conditions, therefore, the shock wave in a gas may be very well approximated by a mathematical surface. In a solid, the picture is somewhat different as the atoms are bound into a lattice and the internal energy is determined by proximity of the lattice sites and the degree of excitation of the nuclei in those sites. There is in addition an electronic contribution to the internal energy. The quantum particle associated with lattice excitation is the phonon and hence, energy can be exchanged from one vibrational mode to another by phonon-phonon scattering. The mean free path for the phonon is considered to be the fundamental length appropriate to the thickness of a shock wave in a solid. The thickness of the shock front estimated in this manner is of the order of 10^{-6} cm (0.4×10^{-6} in) (reference 17).

It is therefore reasonable to regard the shock wave front as a mathematical surface moving with velocity D into a medium initially having velocity, density, pressure and internal energy u_o, ρ_o, p_o and e_o.

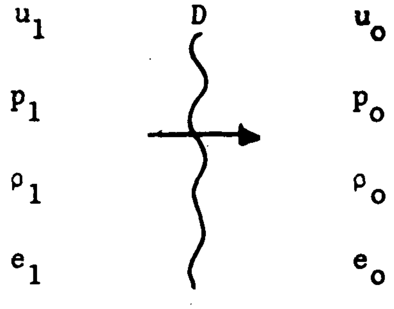

Because there is no accumulation of mass or energy within the front, we may write

$$\rho_1(D - u_1) = \rho_o(D - u_o) \tag{2.1}$$

$$p_1 - p_o = \rho_o(D - u_o)(u_1 - u_o) \tag{2.2}$$

$$e_1 - e_o = (p_1 + p_o)(\frac{1}{\rho_o} - \frac{1}{\rho_1}) \tag{2.3}$$

These equations reflect the conservation of mass, momentum and energy, respectively. They relate the state of the material behind the shock wave to that of the material ahead without any reference to the microscopic process responsible for effecting the change in state. Often, one may eliminate the internal energy by means of the equation of state

$$e = e(p,\rho) \tag{2.4}$$

When this is done one may determine the Hugoniot relation for the material

$$H(p_1, \rho_1; p_o, \rho_o) = e(p_1, \rho_1) - e(p_o, \rho_o) - (p_1 + p_o)(\frac{1}{\rho_o} - \frac{1}{\rho_1}) \tag{2.5}$$

The requirement that

$$H(p_1, \rho_1 : p_o, \rho_o) = 0 \tag{2.6}$$

generates a curve in the (p,ρ) plane known as the Hugoniot. The Hugoniot is a process equation for shock wave compression, just as the requirement of constant entropy yields a process equation for adiabatic behaviour.

Let us now regard the unshocked material as being at rest so that $u_o = 0$ and equations (2.1), (2.2), and (2.3) become

$$\rho_1/\rho_o = D/(D - u_1) \tag{2.7}$$

$$p_1 - p_o = \rho_o D u_1 \tag{2.8}$$

$$e_1 - e_o = (p_1 + p_o)(1/\rho_o - 1/\rho_1) \tag{2.9}$$

It is observed experimentally that for many materials, a linear relationship exists between the velocity of the shock wave relative to the undisturbed medium and the particle velocity of the shocked fluid.

$$|D| = c + s|u_1| \tag{2.10}$$

where c and s are constants for any given material over a wide range of shock wave velocities.

It is possible to use equation (2.10) to derive a Hugoniot relation from equations (2.7) and (2.8) without reference to the internal energy. This becomes essential when the function $e(p,\rho)$ is not known. After substitution of equation (2.10) into equations (2.7) and (2.8) and elimination of D and u, we have:

$$p_1 - p_o = \frac{\rho_1 c^2 (\rho_1/\rho_o - 1)}{[(s - 1)\rho_1/\rho_o - s]^2} \tag{2.11}$$

A useful approach to the analysis of shock waves involves the (p,u) plane. From equations (2.8) and (2.10) we have for a right running shock wave ($D - u_o > 0$, $u_1 - u_o > 0$)

$$p_1 - p_o = \rho_o[cu_1 + su_1^2] \tag{2.12}$$

Equation (2.12) connects the shocked particle pressure and velocity for material originally at rest. In the case of impact phenomena at meteoroid velocities $p_1 >> p_o$ so that it is customary to neglect p_o.

Consider figure 2.1 in which equation (2.12) is denoted schematically by the curve H_R. Material originally at rest in the laboratory frame of reference and having pressure p_o will be processed by a right running shock wave to pressures and particle velocities which are related by H_R.

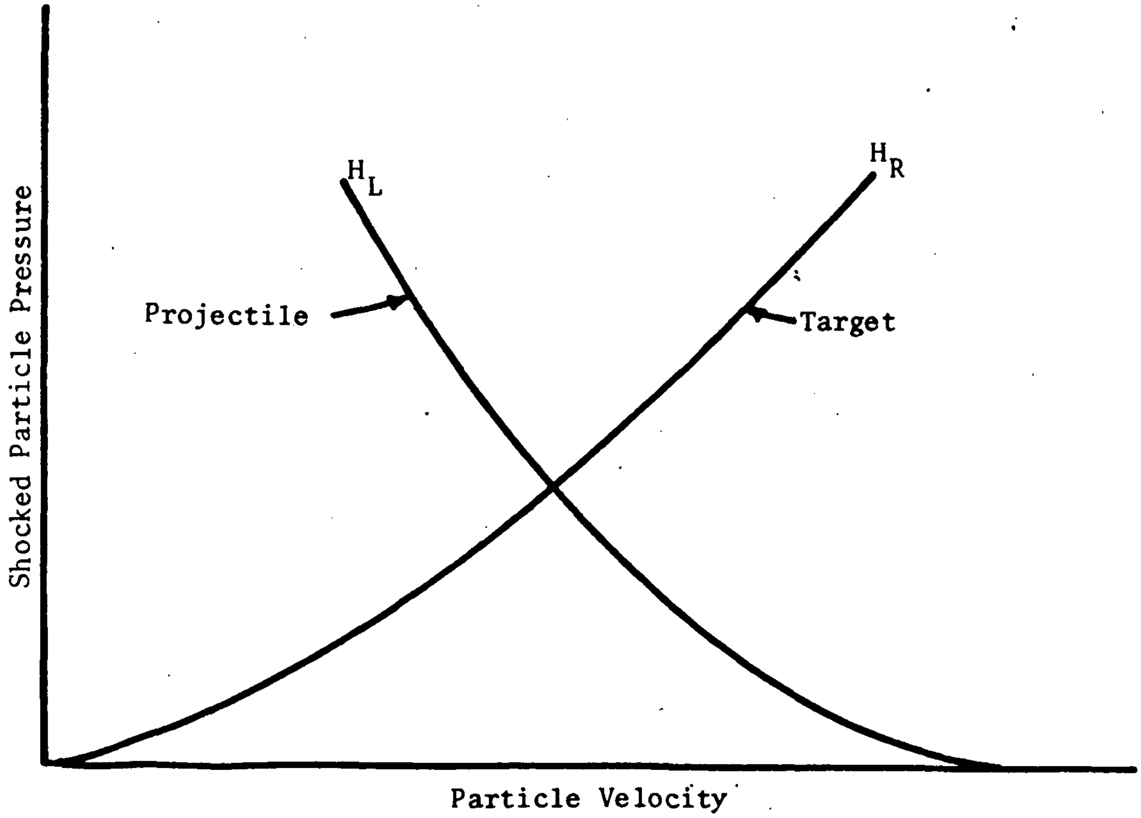

Figure 2.1 Schematic of Hugoniots in (p,u) Plane Corresponding to Right and Left-Running Waves

From equation (2.8) it is easy to see that the same material originally at pressure p_o and having particle velocity V will be processed by a left running wave to states lying on H_L which is a mirror image of H_R.

Now consider a like material impact (figure 2.2)

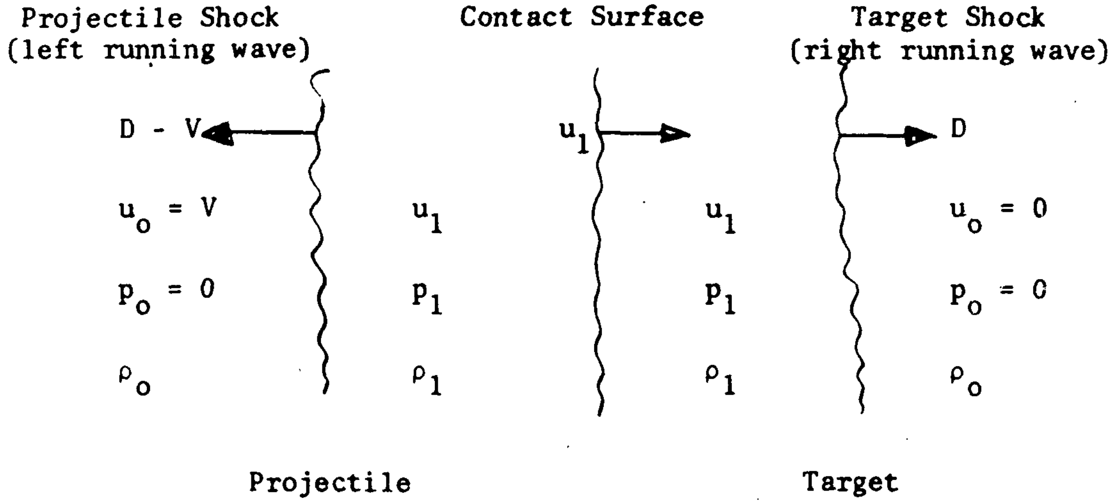

Figure 2.2 Schematic of Wave System Created by Impact

Both the target and the projectile are regarded as having initial pressure $p_o = 0$. The target is initially at rest and is accelerated by a right running shock wave. Consequently, the shocked target material is described by a wave in the (p,u) plane of the form H_R.

Similarly, the projectile material, originally having velocity V, is decelerated by a left running wave and the process is described by H_L. At the contact surface separating the shocked target and projectile material we have the requirements that the particle velocity and pressure be continuous. Thus the shocked state corresponds to the point of intersection of H_L and H_R. For like materials, the symmetry of H_R and H_L demands that the shocked particle velocity be one half the impact velocity.

The properties of the shocked material are determined in general, by measuring either the shock wave velocity or the particle velocity, (references 4,5,6,7,8,9). A review of recent practice is contained in reference 10

We suppose that we have a like material impact:

$$\begin{aligned} \rho_1/\rho_o &= D/(D - u_1) \\ \rho_1 &= \rho_o u_1 D \qquad (2.13) \\ u_1 &= V/2 \end{aligned}$$

Equations (2.13) describe the target which is initially at rest. If we measure V and D (ρ_o is presumed known), we can solve for p_1 and ρ_1. Thus we will have determined one point in the Hugoniot curve. By varying V from test to test, we may generate the Hugoniot curve for the material.

The impact velocity was determined in the usual manner (reference 2) from flash x-ray measurement. To determine the shock wave velocity in the target, we instrumented a Lexan rod (1.27 cm (0.5 in) diameter by 3.8 cm (1.5 in) long) with five detectors. Figure 2.3 shows the orientation of the detectors in the target.

Each trigger consisted of two 0.075 mm (0.003 in) diameter enamelled copper wires mounted side by side. The target was split in half and the five sets of trigger wires were mounted on the exposed diameter. The two halves of the target were bonded together with Eastman 910 cement and the rear of the target with the output connections was potted in epoxy. Figure 2.4 is a photograph of an instrumented target.

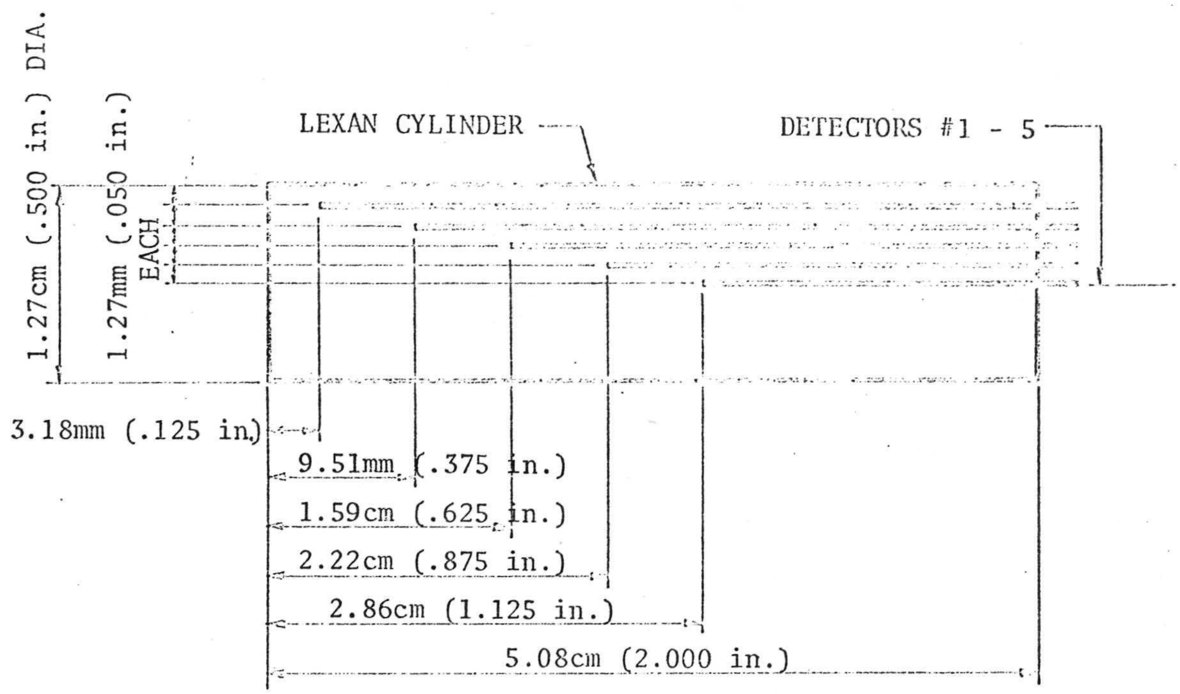

Figure 2.3 Locations of Triggers in Instrumented Target

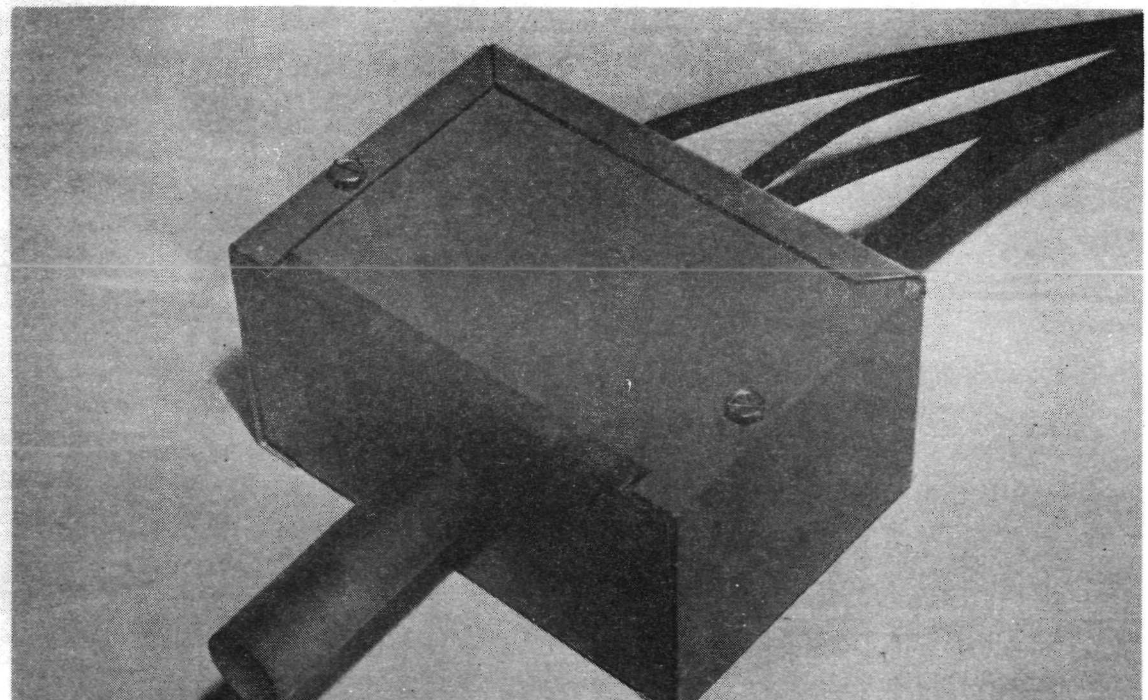

Figure 2.4 Photograph of Instrumented Target

Page Intentionally Left Blank

Because of the high conductivity of the shocked material as compared with the very low conductivity of Lexan under ordinary conditions, the shock wave behaved like a switch, closing the circuit between each pair of wires as it passed by. The closing event triggered a pulse amplifier which delivered a 0.03 μsec pulse to an oscilloscope. The first such pulse served to trigger the scope while the remaining four appeared as a very sharp spike on the scope record. The sensor units had an inherent delay of .03 μsec and a pulse width of 0.05 μsec. The delay was of little consequence as it was equal for all the triggers and the short pulse width made for a clear display on an oscilloscope sweeping at a fast rate (0.5 μsec/cm). The sensor unit circuitry and a schematic of the trigger monitoring hook-up are shown in figure 2.5. A schematic of the overall instrumentation set-up is shown in figure 2.6. A typical scope record is shown as figure 2.7. The record is from shot N67-362 which involved a Lexan on Lexan impact at 7.28 km/sec (23,900 ft/sec). Both the upper and the lower trace were triggered by the first sensor. Sensors 2 and 3 were monitored on the upper and 4 and 5 on the lower trace. Both traces were swept at 0.5 μsec/cm and because of the rapid decay of the wave in the target, the fifth sensor pulse is apparently off scale to the right and is not seen. Figure 2.8 consists of two frames of the Beckman and Whitley coverage of the event and illustrates the normality of the impact. In figure 2.9 we have reduced the data of figure 2.7 into graphical form. Little decay is observed in the first centimeter (0.4 in) of travel of the shock wave. However, strong decay is observed between the third and fourth sensors. Very similar results are seen in figure 2.10 which corresponds to a round at somewhat lower impact velocity.

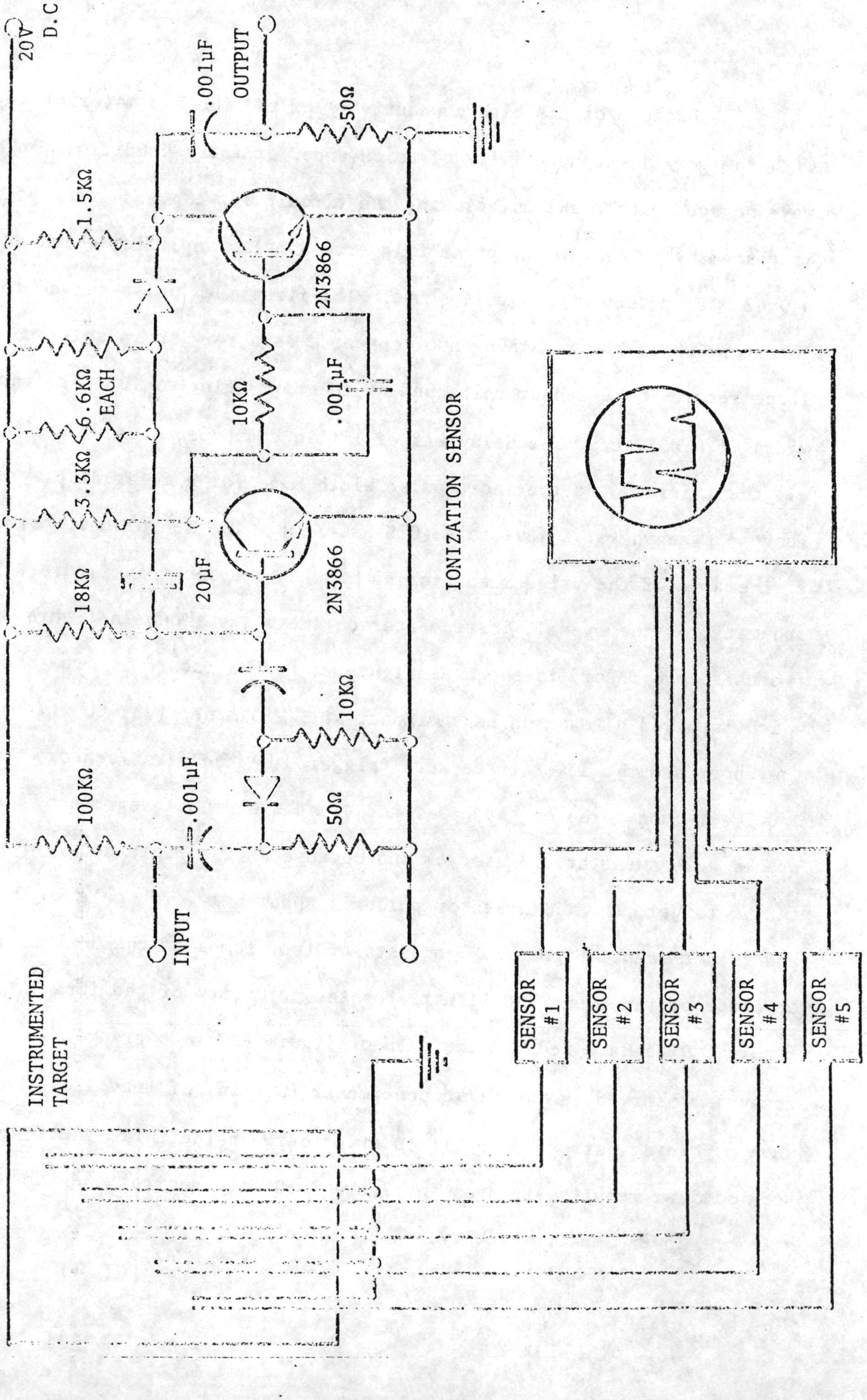

Figure 2.5 Layout of Five Channel Shock Trajectory Instrumentation

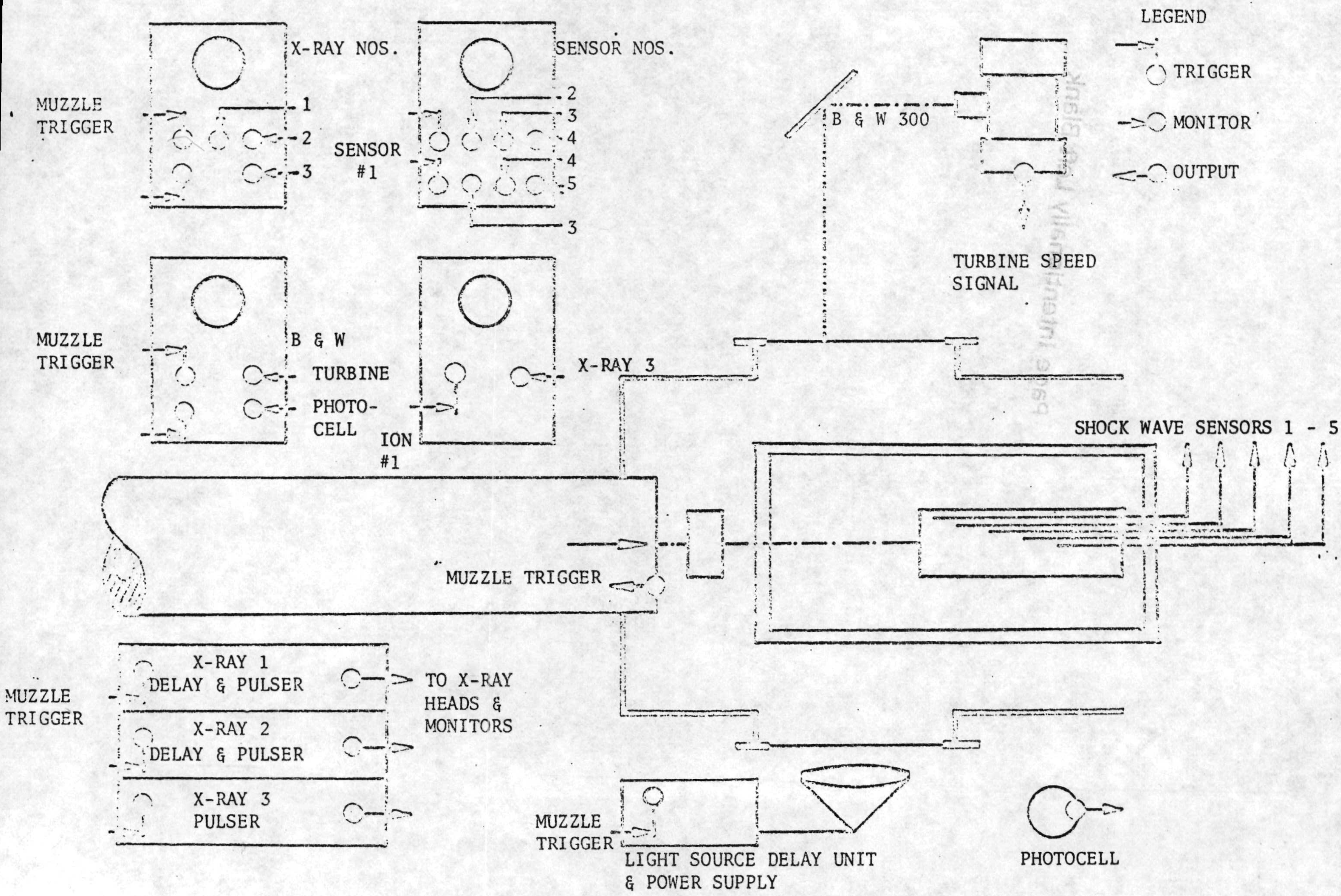

Figure 3.6 Schematic of Instrumentation

Page Intentionally Left Blank

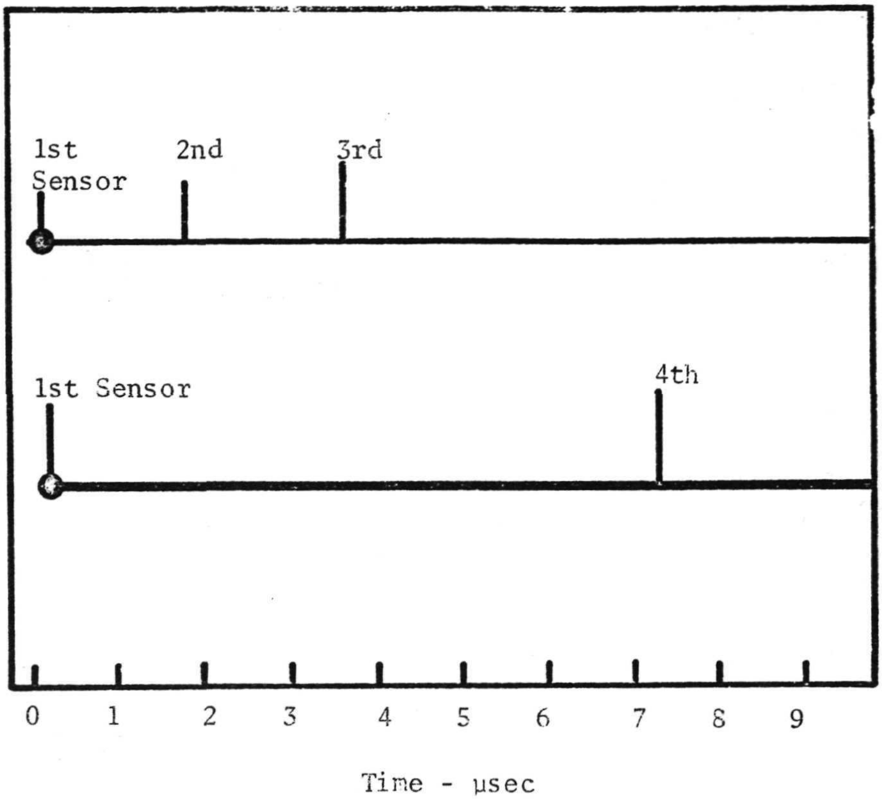

Figure 2.7 Oscilloscope Trace of Shock Wave Sensors from Shot N67-362. Lexan on Lexan at 7.28 km/sec (23,650 ft/sec)

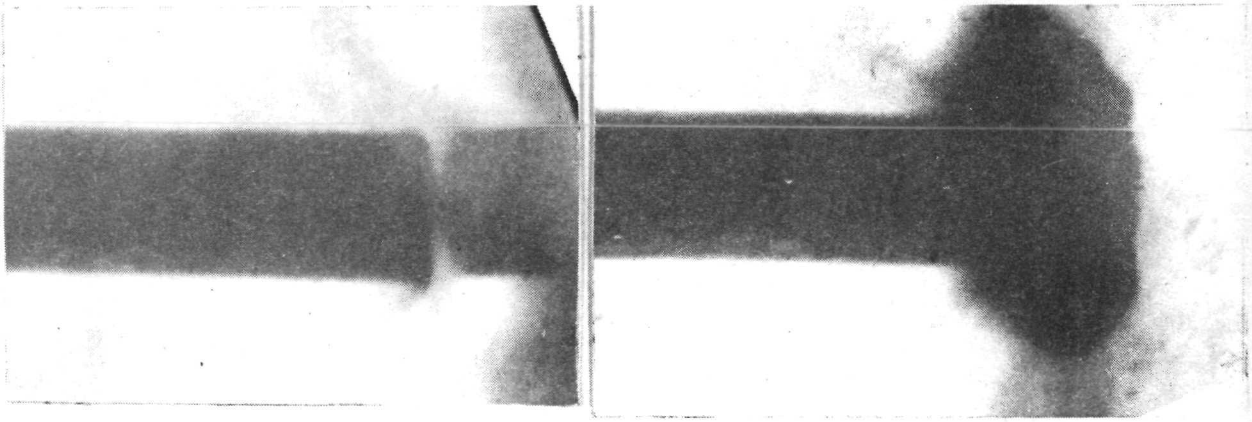
(a)

(b)

Figure 2.8 Frames from B & W 300 Photo Coverage of N67-362. (a) Just before and (b) just after impact.

The decay in shock wave velocity is due to interaction with the free surfaces of the target and projectile. As may be seen from figure 2.8(b), the interference causes ejection of the shocked material into the ambient vacuum. The reflection of the shock wave at the boundaries generates rarefaction waves which eventually overtake the shock wave (references 14, 18). In order to obtain an accurate measurement of shock wave velocity, it is customary to use very thin targets together with only two sensors. We have relied, however, on the accumulation of several points on the trajectory in order to reconstitute accurately the initial velocity. Apparently, referring to figures 2.9 and 2.10, the change in shock velocity is small over a distance equal to approximately 1.3 cm (0.5 in) (which is equal to the diameter of the target).

Figure 2.11 shows the Hugoniot data for Lexan in terms of shock wave velocity versus particle velocity. The values of c and s determined from figure 2.11 compare reasonably with values for other plastics (reference 19). In figure 2.12 we have shown the Hugoniot curve in the (p,ρ) plane.

The bulk of the rounds fired in the experimental programs has involved Lexan projectiles striking lead targets. For reference we have used the above values of c and s for Lexan together with values appropriate to lead (reference 20) to determine the shocked pressure and particle velocity as a function of impact velocity (figure 2.13).

An attempt was made to determine Hugoniot data in a different manner. The flash x-ray units were deployed directly over the impact point so as to obtain radiograms very shortly ($\sim$1 μsec) after the impact. The shocked material would then be distinguishable as a relatively darkened area on the

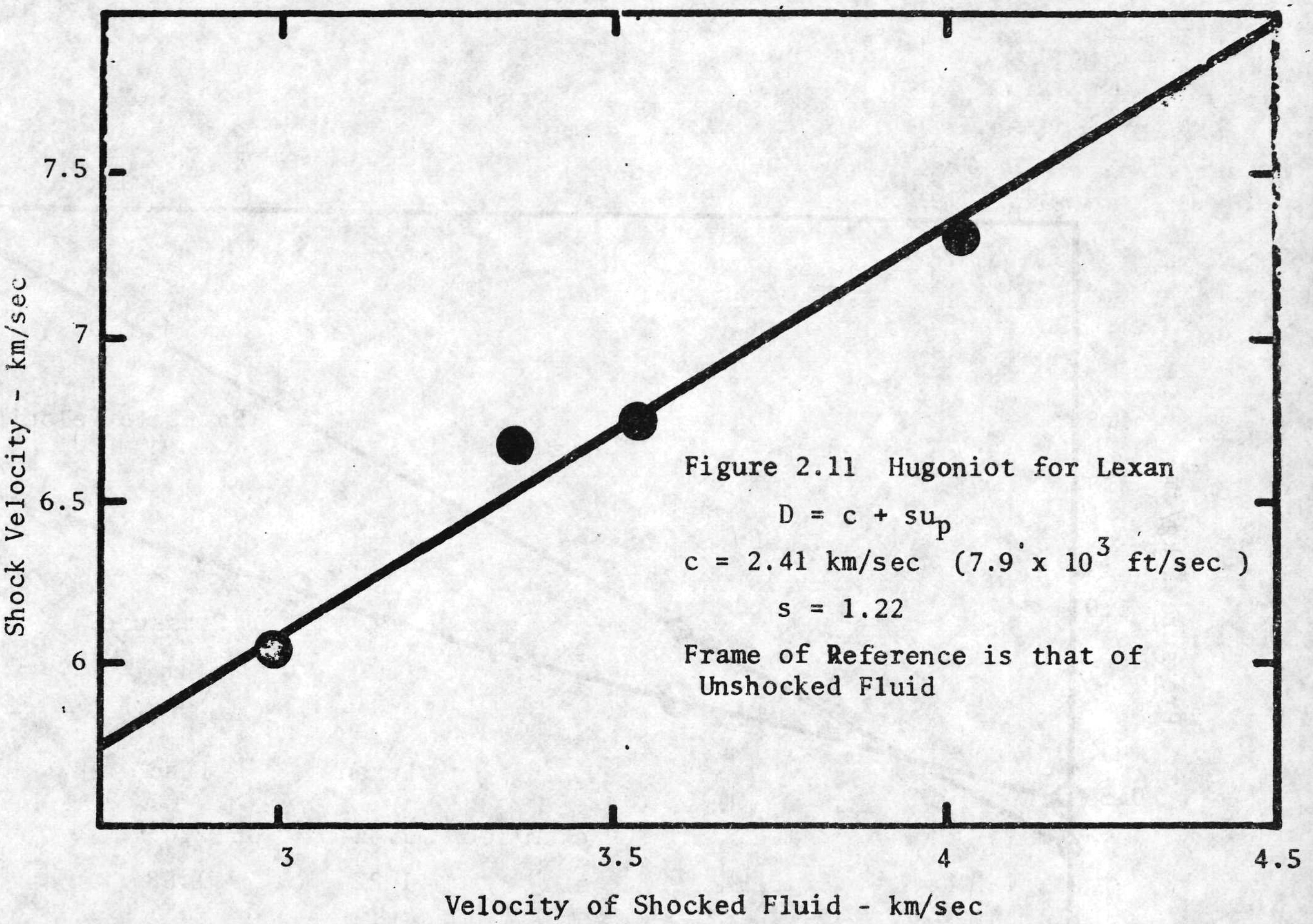

Figure 2.11 Hugoniot for Lexan

$D = c + su_p$

$c = 2.41$ km/sec (7.9×10^3 ft/sec)

$s = 1.22$

Frame of Reference is that of Unshocked Fluid

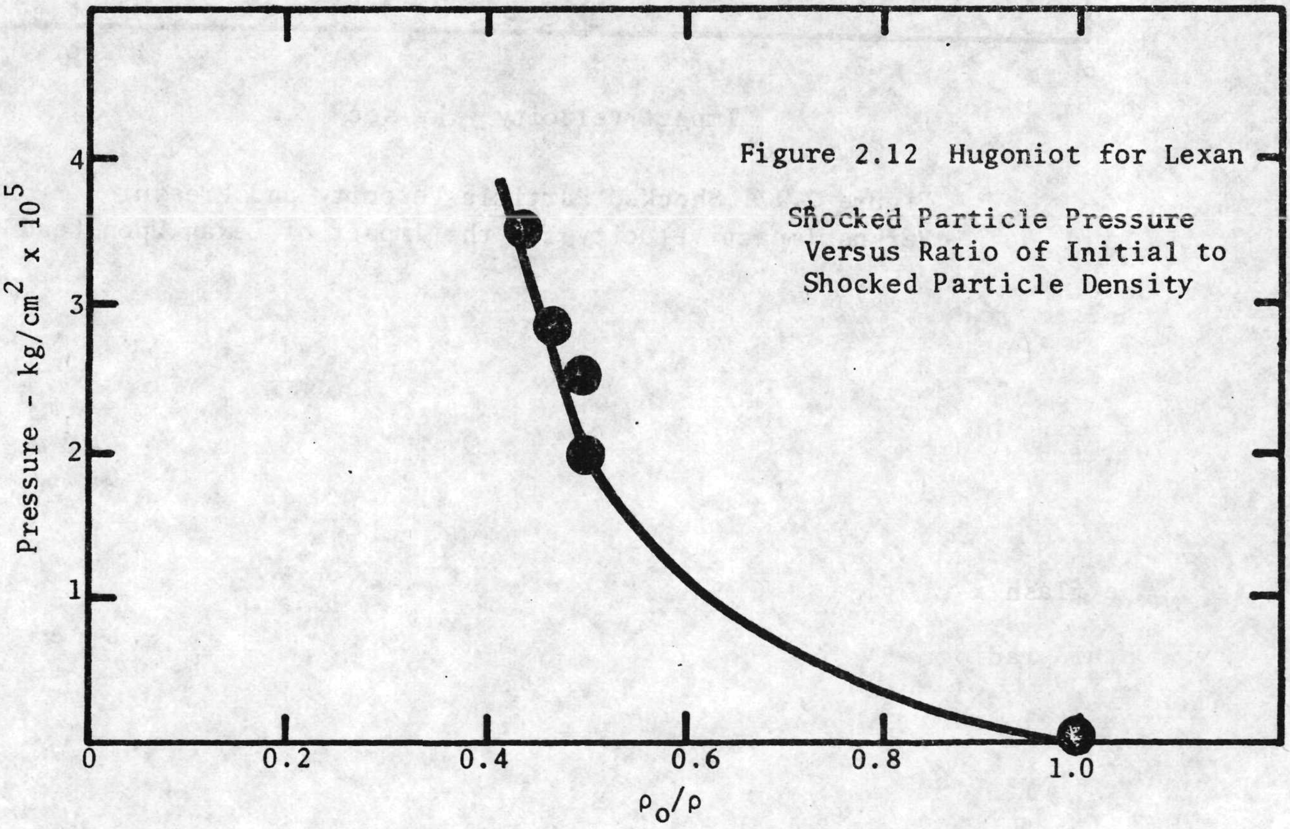

Figure 2.12 Hugoniot for Lexan

Shocked Particle Pressure Versus Ratio of Initial to Shocked Particle Density

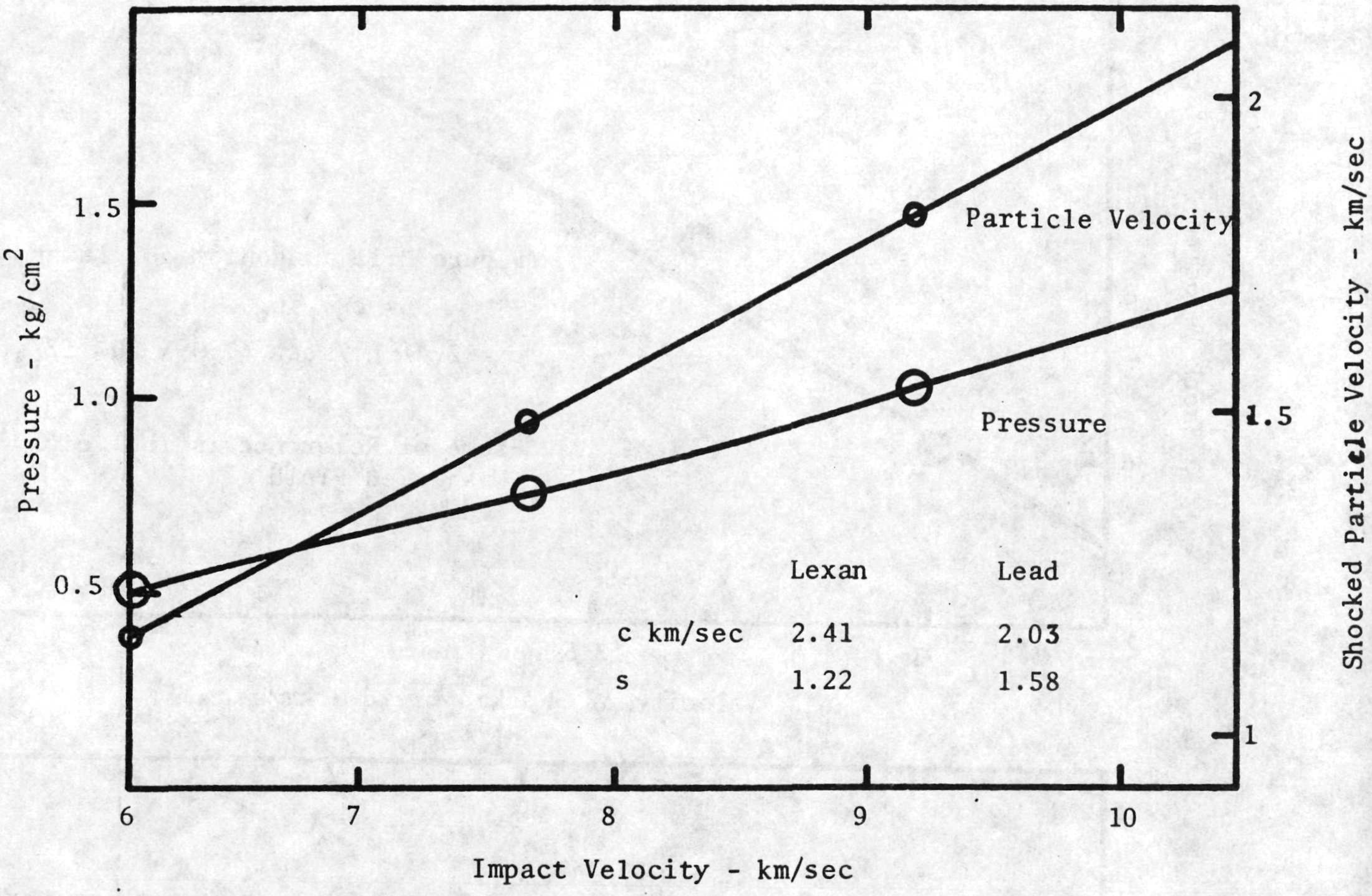

Figure 2.13 Shocked Particle Velocity and Pressure Versus Impact Velocity for the Impact of Lexan Upon Lead

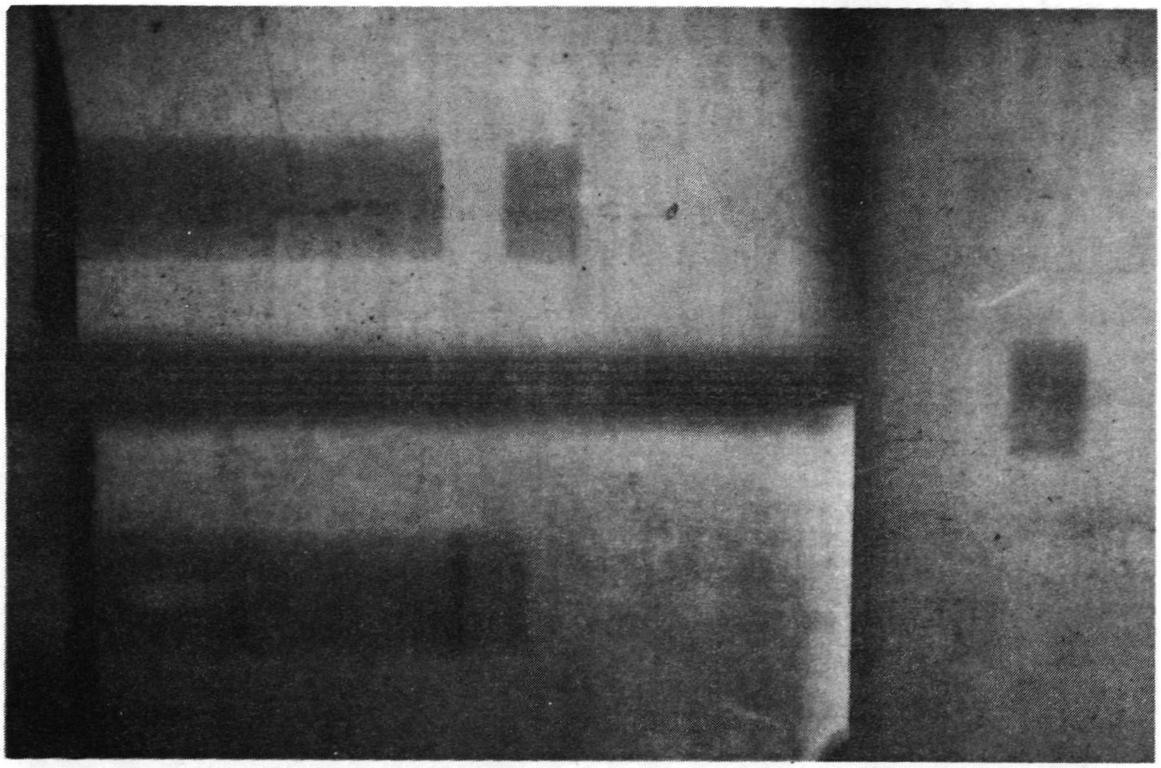

Figure 2.14 X-rays of Impact of Lexan Cylinders at Approximately 8.25 km/sec (27,000 ft/sec), Showing Shocked Region

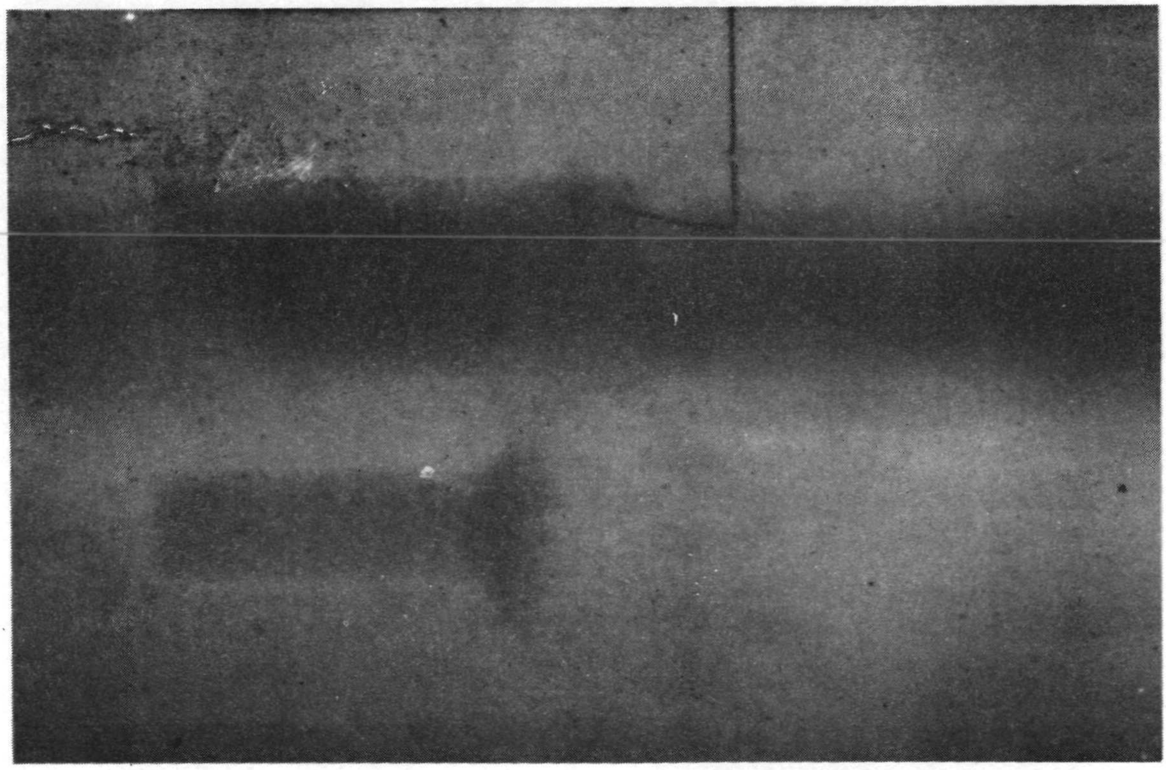

Figure 2.15 X-rays of Impact of Lexan Cylinders at Approximately 8.25 km/sec (27,000 ft/sec), Showing Shocked Region

film and a determination of the compression could be made. As discussed in reference 21, the main technical obstacle lay in triggering the x-rays with the required precision. No quantitative data was gathered by this technique. However, the radiograms of successful rounds are of qualitative interest. Figure 2.14, for example, is taken essentially at the instant of impact and reveals quite clearly the one-dimensional character of the shock waves in the target and the projectile. Figure 2.15 consists of two radiograms of the shock wave system taken 0.3 μsec and 1.8 μsec after impact. The second x-ray was taken too late to permit reduction of data as the initial one-dimensionality of the impact evident in the first x-ray has been lost through the mechanisms of free surface effects. It is interesting to compare this observation with the information of figures 2.9 and 2.10 which indicate the presence of strong decay in the shock wave velocity after approximately 2 μsec.

The first x-ray of figure 2.15 can be analysed by reference to figure 2.16.

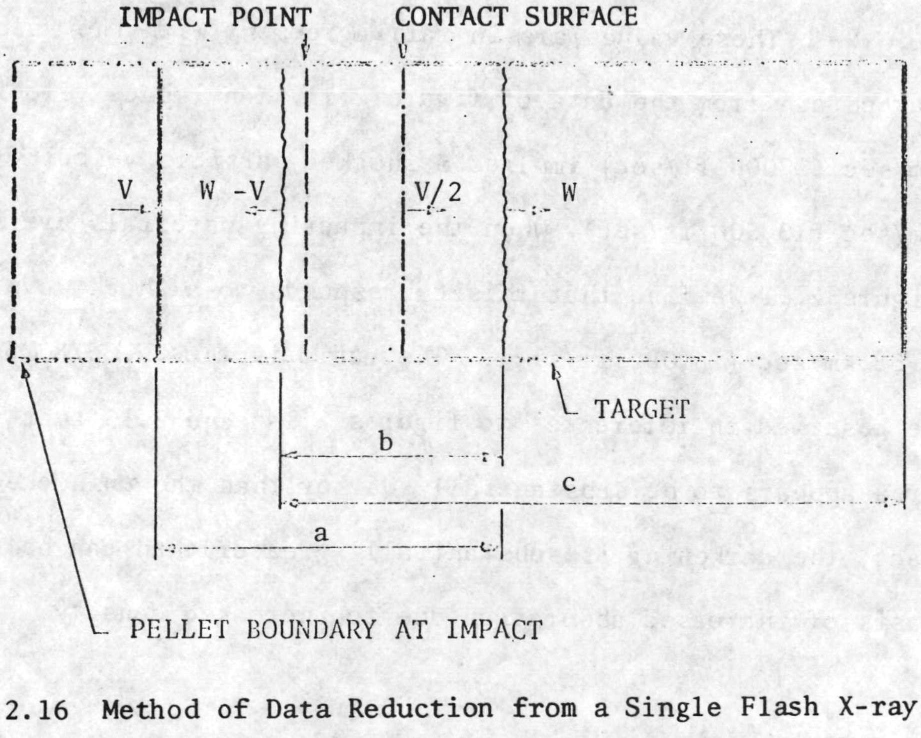

Figure 2.16 Method of Data Reduction from a Single Flash X-ray

The impact was due to a 1.27 cm (0.5 in) diameter by 0.76 cm (0.3 in) long Lexan pellet striking a 1.27 cm diameter (0.5 in) Lexan target at approximately 8.23 km/sec (27000 ft/sec). The velocity was not measured in the usual manner as the x-ray units were required to monitor the impact. The velocity is inferred from the gun parameters by reference to other firings. From figure 2.15 we find, in the terminology of figure 2.16:

$$a = 0.3 + (W - V)\tau$$

$$b = W\tau + (W - V)\tau$$

$$c = 2.0 + (W - V)\tau$$

so that

$$\frac{W}{V} = \frac{(b - (a - 0.3))}{(b - 2(a - 0.3))}$$

and

$$\frac{W}{V} = \frac{(b - (c - 2.0))}{(b - 2(c - 2.0))}$$

Values of W/V of 1.09 and 1.00 were obtained from the values of a and c respectively.

These values are in fair agreement with the value of 0.9 which we may obtain from the data of figure 2.11. An impact velocity equal to 8.23 km/sec (27000 ft/sec) implies a shocked particle velocity equal to 4.12 km/sec (13,500 ft/sec), when the impacting materials are identical. From figure 2.11 we find that this corresponds to a shock wave velocity equal to 7.38 km/sec (24,000 ft/sec). The ratio is thus 7.38/8.23 = 0.9. It will be observed in reference to figures 2.14 and 2.15 that the compressed area appears to be substantially darker than the unshocked material. In fact, the darkening is substantially greater than can be explained on the basis of increased absorption due to increased density. By comparison with a reference cone, it is found that the apparent density is approximately four times greater than the original. The explanation lies in the presence of two mechanisms for scattering of x-rays in solids, namely by the photo-electric effect (ejection of a bound electron) and by scattering by free electrons. The cross section for photo-electric absorption by carbon atoms is quite small in comparison to that for scattering by free electrons for x-ray energies equal to 30 Kev. (reference 22, pg. 160). In the uncompressed state, Lexan is a dielectric material and absorption occurs principally by the photo-electric effect. After processing by shock waves, the material is heated sufficiently to free outer shell electrons. Then absorption is also effected by scattering due to free electrons. This remark is appropriate to x-rays having energies greater than 25 Kev. However, for somewhat lower energies, the cross section due to the photo-electric effect is substantially greater than the free electron scattering cross section and we may anticipate a correspondingly smaller relative contribution of free electrons to the total absorption. Thus for x-ray energies, somewhat less than 25 Kev, we may expect the absorption per unit length to be approximately proportional to the density.

3.0 INTERACTION OF THE MAIN WALL AND THE IMPACT DEBRIS

The loading on a main wall (simulating the spacecraft hull) has been examined in reference 3. We present here some additional experimental results together with some data concerning the response of the wall. The main walls used in the experiments were sufficiently large (46 cm by 46 cm)(18 in. x 18 in.) that the boundaries played no part during the loading and fracturing time. Consequently, the results are appropriate to analyses which assume that the main wall has no finite boundaries. The wall is also unsupported and free of additional protection beyond the shield. This distinction is important as we will be concerned, in subsequent sections, with the effect on impact penetration of having a cryogenic insulation panel in front of the main structural wall and/or having the wall supported from behind by a body of water.

In addition to the photographic records of time sequenced displacements of the main wall, we present some ballistic limit data. The acquisition of ballistic limit data has not been a primary concern of the program, but has been required in order to evaluate better the interaction of cryogenic panels with impact debris and to provide a standard against which the Grid-Bumper could be evaluated.

3.1 Measurements of Stagnation Pressure in the Debris Cloud

Measurements of the stagnation pressure in the cloud were made using the piezo-bar pressure probe described in references 2 and 3. In all cases, the gauges were flush-mounted in a rigid witness sheet. The pressures recorded can therefore be correlated with the response of a main wall. As we show presently, the main wall may displace somewhat during the loading cycle; however the velocity of the wall is small compared with the incident particle velocity in the cloud so that the effect of the motion on the stagnation pressure is thought to be negligible. Consequently, it will be supposed that the loading on a main wall is independent of the thickness of the wall for all cases of practical interest.

The gauge described in reference 3 was modified slightly in order to permit the sensors to be placed closer together. A single multi-gauge housing was fabricated to permit close spacings of the gauges. The module, illustrated in figures 3.1(a) and 3.1(b), is also more convenient to set up than a cluster of individual gauges. Records from a five gauge assembly are shown in figure 3.2. The debris is due to the impact of a Lexan cylinder onto a lead shield at 8.2 km/sec (26,800 ft/sec) and the witness sheet is spaced 15.2 cm (6 in) downstream from the shield. The configuration is illustrated in figure 3.1(c). It will be observed that the impact has not centered on gauge E as would be desired. Instead, the impact has apparently centered near gauge A.

We can locate approximately the center of impact by reference to figure 3.3. Since D and E give the same peak reading, we assume that they are equidistant from the center which must therefore lie on the right bisector of the line joining D and E. Also we can locate by linear interpolation on the line segment EC, an approximate location in which the peak pressure is equal to that at gauge B. Then by construction of a second right bisector, we can locate the apparent center of impact. In figure 3.4 we have treated data from the following round (N67-366) in precisely the same manner. The conditions which produced the pressure readings in figure 3.4 are almost identical to those of figure 3.3: the only difference being in the angle of orientation of the projectile onto the shield. The projectile was tilted 13 degrees from

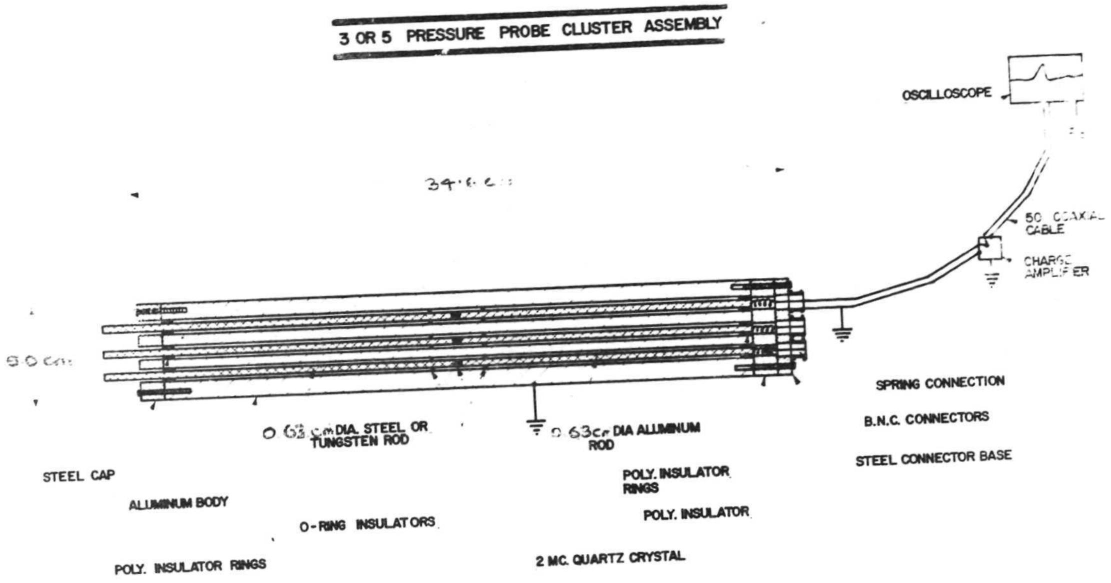

Figure 3.1a Cross-Section of Multiple Piezo-Bar Gauge Module

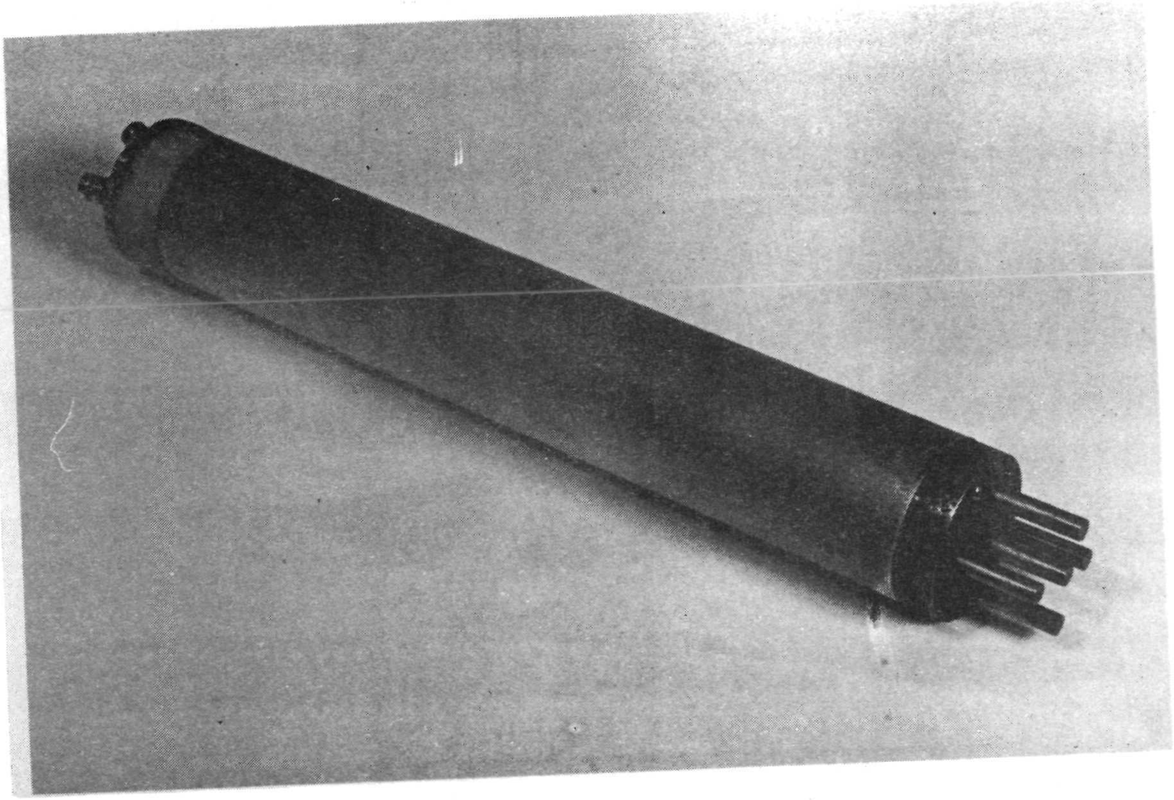

Figure 3.1b Photograph of Assembled Piezo-Bar Gauge Module

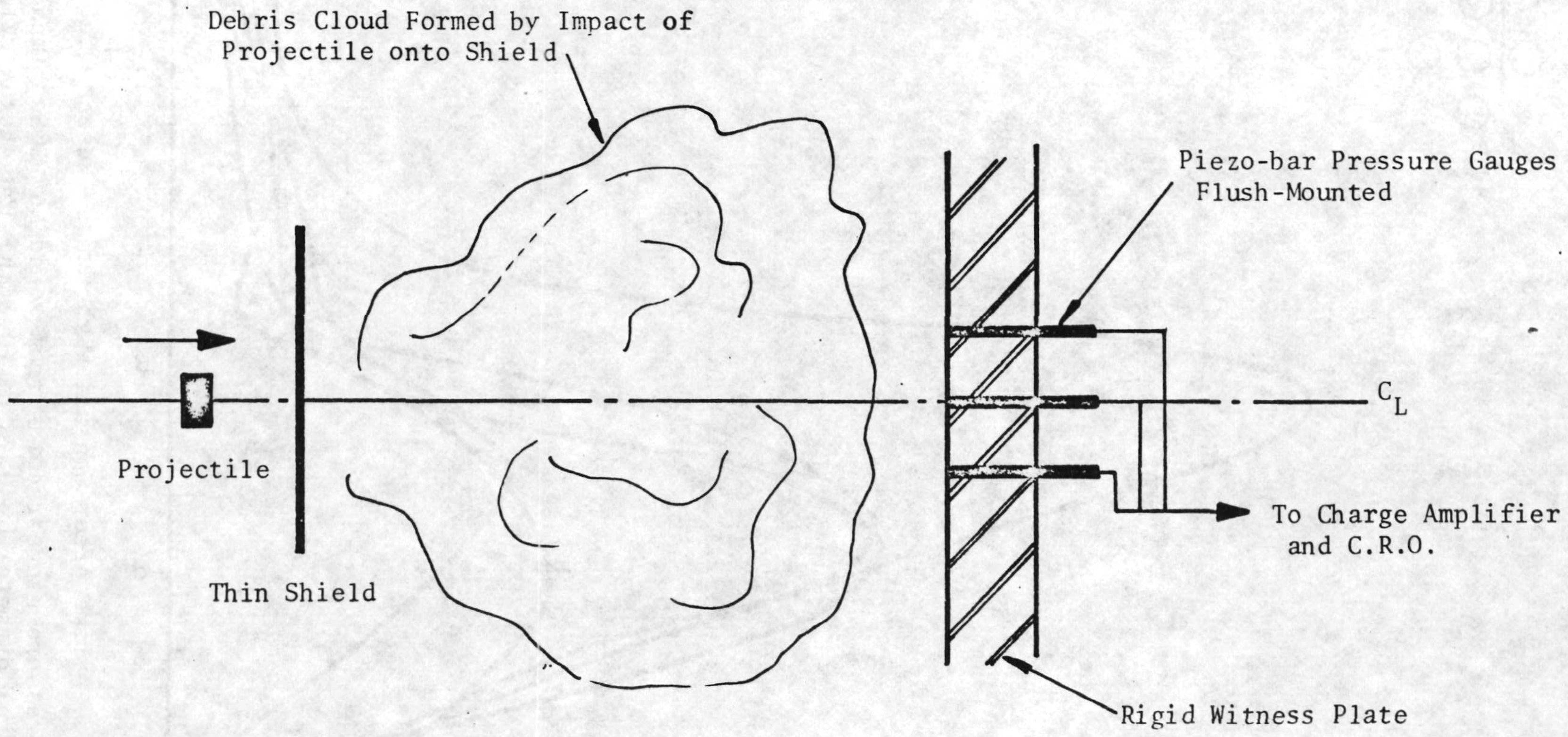

Figure 3.1c Schematic of Experimental Configuration to Determine Debris Cloud Loads on Main Wall

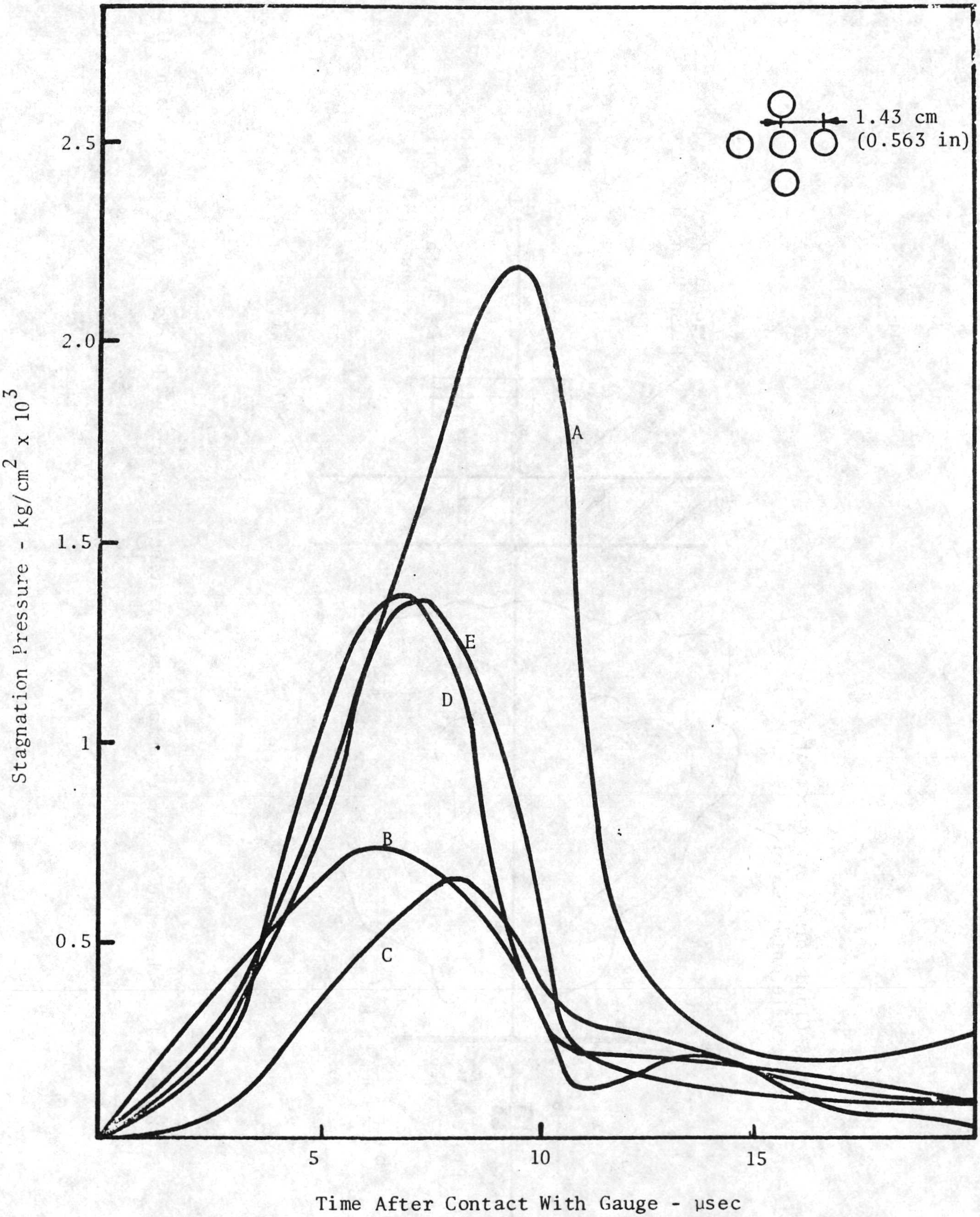

Figure 3.2 Pressure gauge records from round N67-365. Impact of a 1.27 cm (0.5 in) diameter by 0.75 cm (0.3 in) long Lexan cylinder onto a 0.25 mm (0.010 in) thick lead shield at 8.2 km/sec (26,800 ft/sec). Gauges flush-mounted with rigid witness sheet spaced 15.2 cms (6 in) downstream from shield.

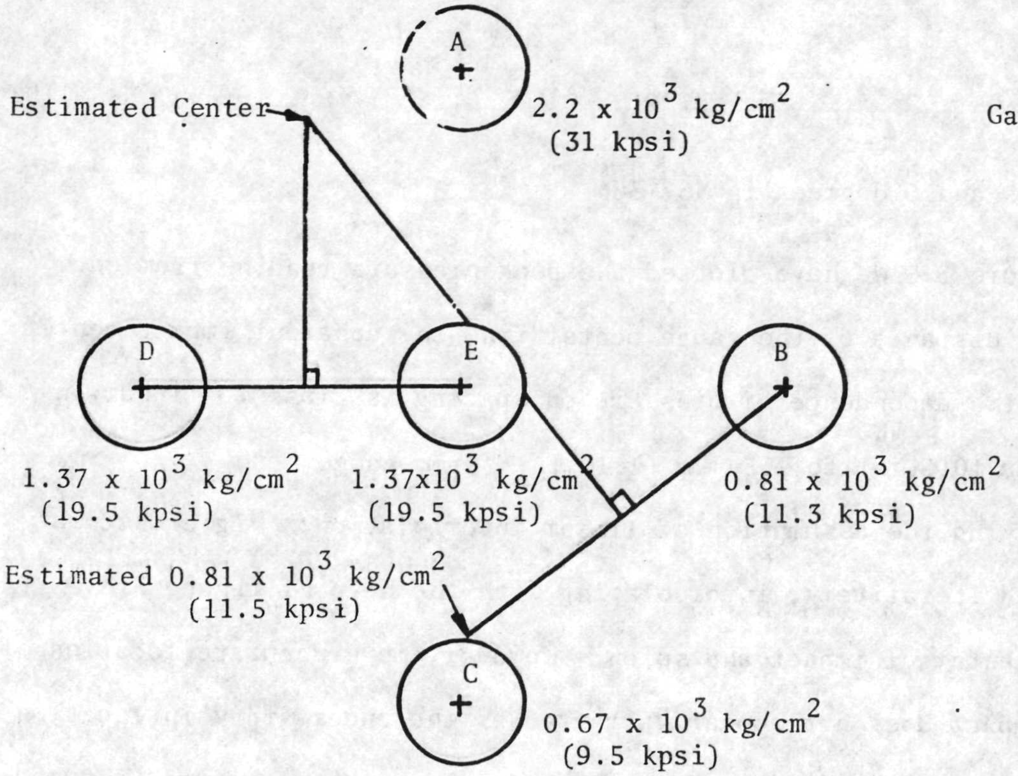

Gauge	Distance from Estimated Center	
	cm	in
A	0.76	0.3
B	2.51	0.99
C	2.79	1.10
D	1.42	0.56
E	1.42	0.56

Figure 3.3 Diagram of gauges showing peak recorded pressures and construction to locate apparent impact center of round N67-365.

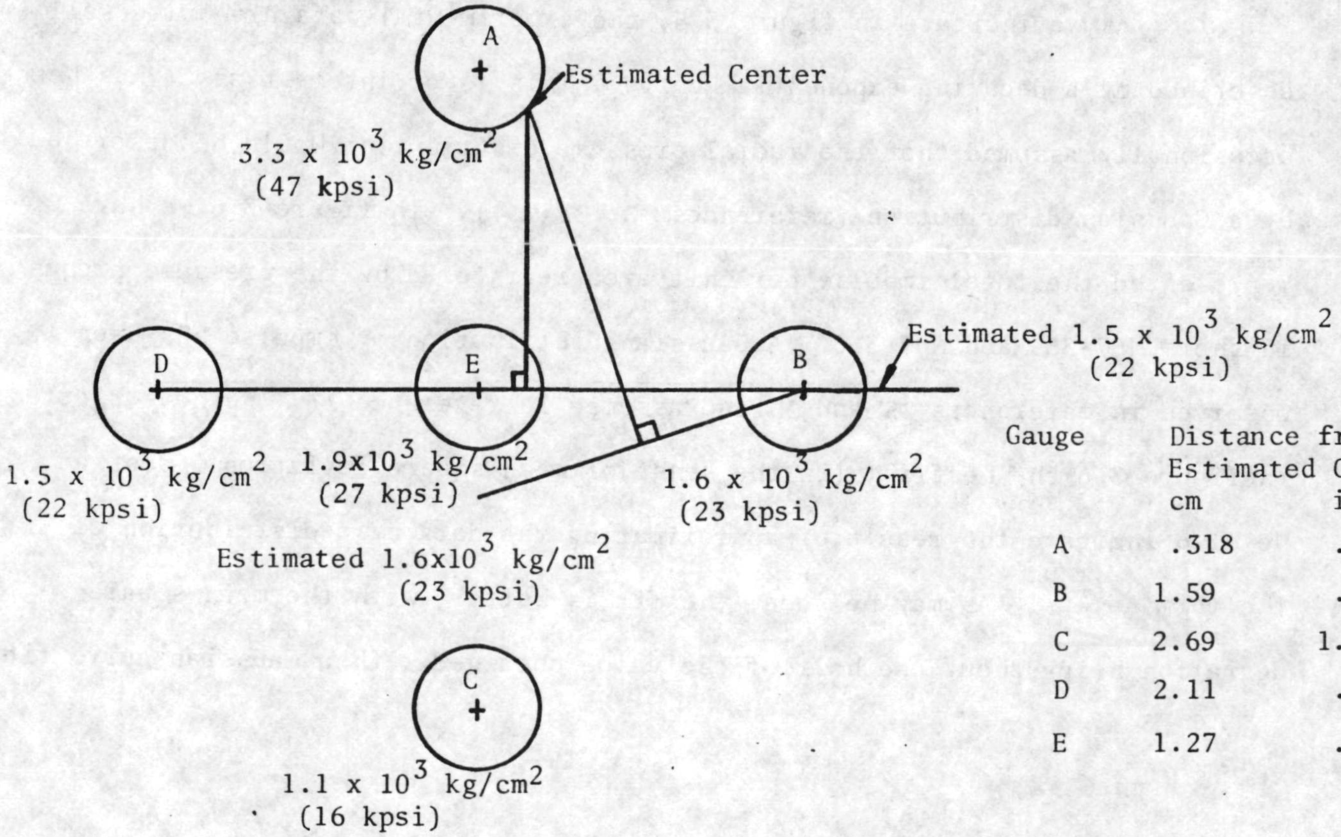

Gauge	Distance from Estimated Center	
	cm	in
A	.318	.125
B	1.59	.625
C	2.69	1.06
D	2.11	.83
E	1.27	.50

Figure 3.4 Diagram of gauges showing peak recorded pressures and construction to locate apparent impact center of round N67-366.

normal in N67-365 and 6 degrees in N67-366.

In figure 3.5 we have plotted the peak pressure reading from each gauge versus the distance of the gauge center from the apparent impact center. We observe that the dependence of pressure on spacing is close to linear in the range 1.27 cm (0.5 in) to 2.54 cm (1.10 in) (from gauge E to gauge C), justifying the assumption of linear interpolation. Higher accuracy could be obtained iteratively, interpolating with the help of figure 3.5, locating a new center of impact and so on. However, more accurate location of the center of impact does not appear warranted as the uncertainty in location is small compared to the diameter of the gauges. We have, of course, assumed in the above that the debris cloud possesses rotational symmetry. It should be noted that this is not strictly true due to the tilting of the projectile on impact.

As we indicate in figure 3.5, the experimental data are quite well described by a decaying exponential curve. This is of interest as it has been occasionally assumed that the radial pressure distribution would be described by a Gaussian distribution (references 3, 23, 24). In figure 3.6 we have represented the total impulse per unit area registered by the pressure probes in shots N67-365 and N67-366. A Gaussian distribution of impulse has been observed in references 25 and 26 and assumed in reference 27. We have plotted in figure 3.6 the best fit (in the sense of mean square deviation) Gaussian. We also indicate the result of approximating the data by a distribution of the form $Ae^{(\frac{r}{\Delta})^n}$. As may be seen, the fit is better, with the mean square deviation being about one half of the value obtained with a Gaussian curve fit.

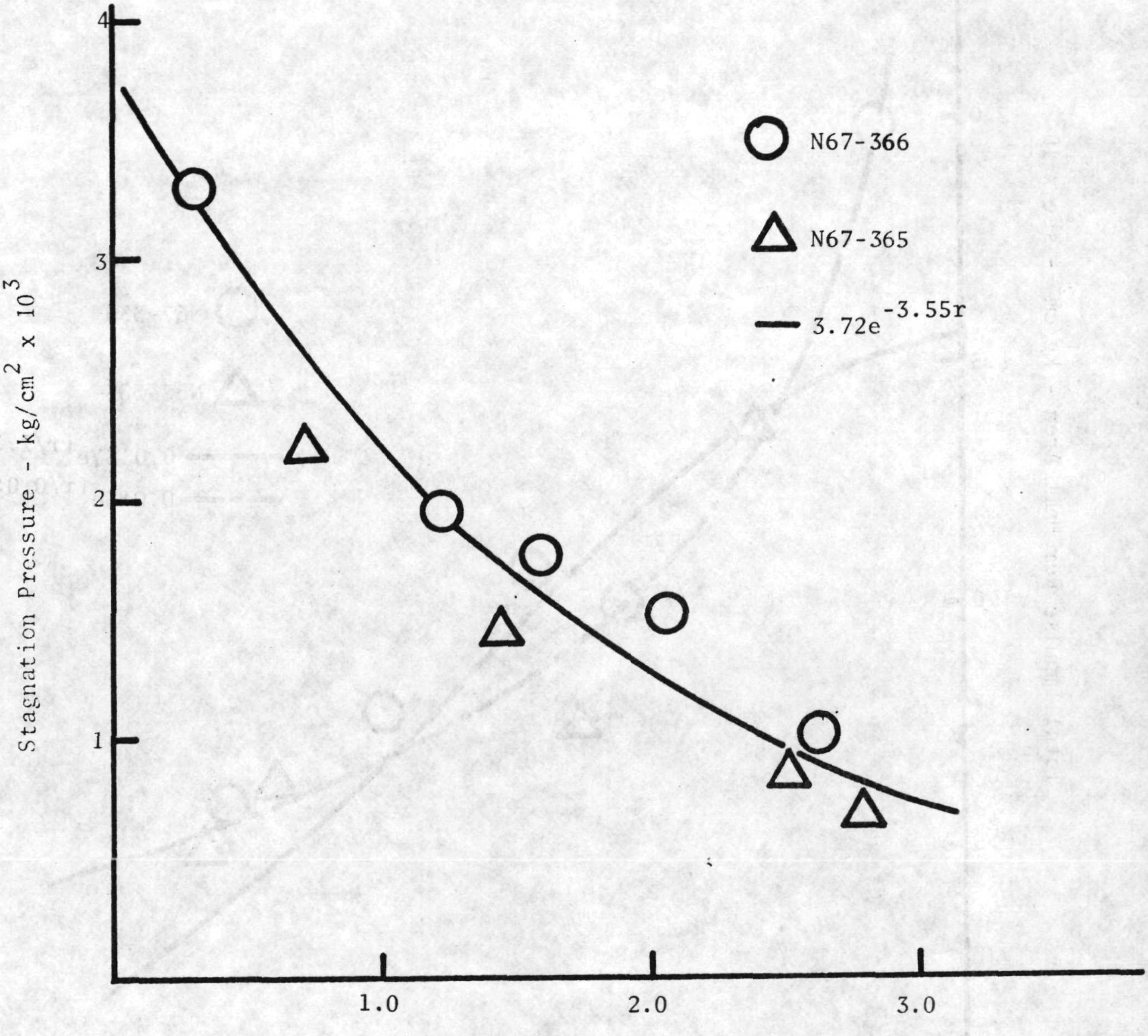

Figure 3.5 Peak stagnation pressure versus spacing from impact center. Debris cloud due to impact of 1.27 cm (0.5 in) diameter by 0.75 cm (0.3 in) long Lexan cylinder onto a 0.25 mm (0.010 in) thick lead shield at 8.2 km/sec (26,800 ft/sec). Gauges flush-mounted with rigid witness sheet spaced 15.2 cm (6 in) downstream from shield.

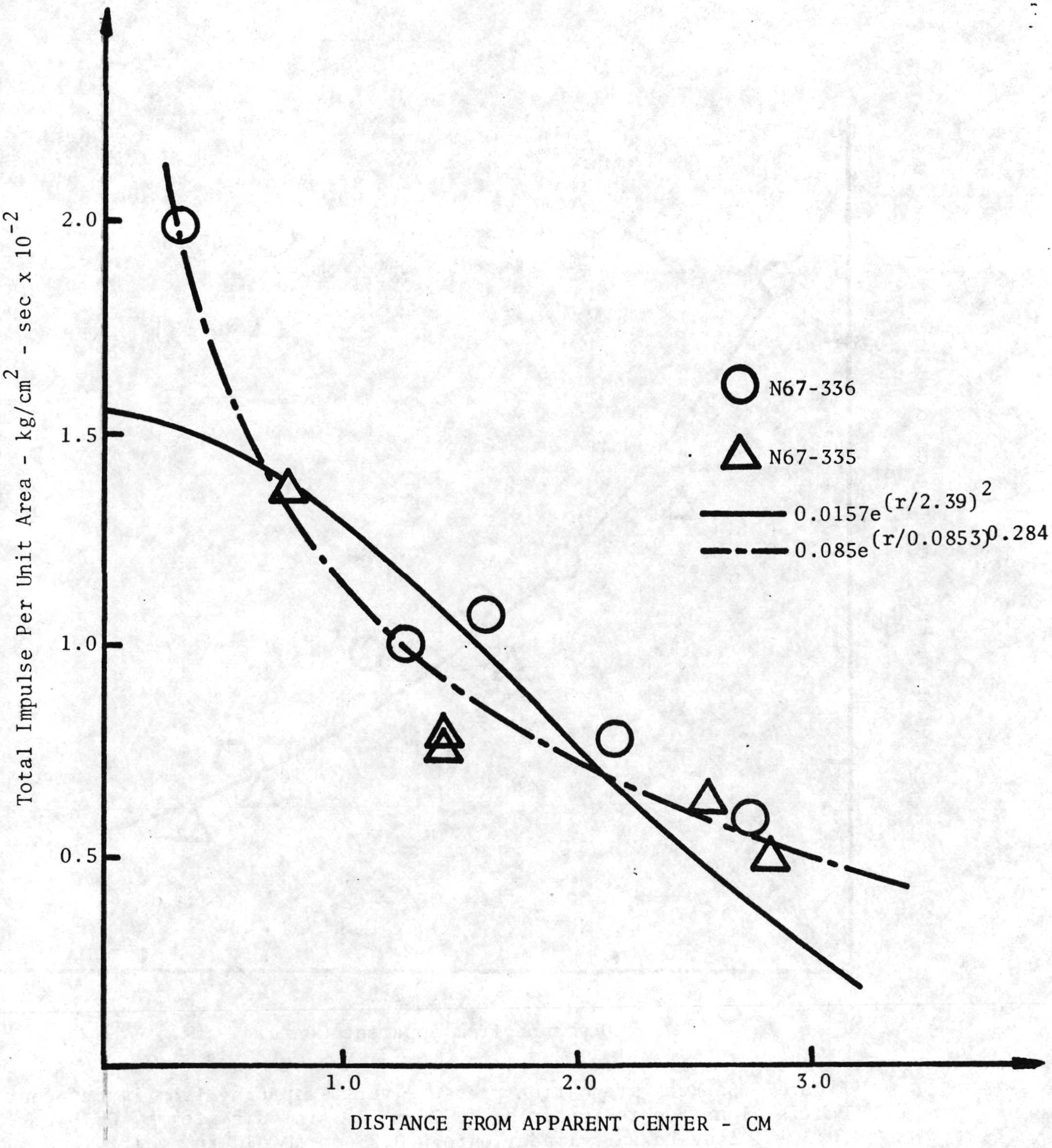

Figure 3.6 Total Impulse per Unit Area Versus Spacing From Impact Center. Debris Cloud as in Figure 3.5.

3.2 Quantitative Response of the Main Wall to Debris Cloud

As discussed in the introduction, the main wall may respond to the debris cloud loading in a variety of manners, depending on the thickness and material properties of the wall, the distance from the shield and projectile material, dimensions and velocity. In figure 3.7 we indicate the quantitative dependence on thickness of the center line deflection of 2024T3 Aluminum main walls. The pressure pulse responsible for the deflection is indicated on the same figure. All the curves have been referenced to the same initial time. However, an uncertainty exists in the zero time for the main wall response as the very early time response was not clearly visible in these particular tests. Three distinct types of response are reflected in the data of figure 3.7. The 0.159 cm (0.0625 in.) main wall suffered a gross deformation and ultimate rupture, several petals being formed. The 0.318 cm (0.125 in.) wall suffered a large permanent deformation but did not rupture. Finally, the 0.635 cm (0.25 in.) wall suffered a deformation under the load but enjoyed considerable recovery upon release. The final deformation of the 0.635 cm wall was small.

In order to gain further insight into the response of the main wall to the debris cloud loading, several rounds were fired in which a Beckman and Whitley 192 camera was used at a high framing rate. Figures 3.8 and 3.9 are two representative series of photographs. From the photographs one may construct the center line history of the main wall. This is done in figures 3.10 and 3.11. In figure 3.12 we have indicated the center line pressure pulse which is associated with the plate displacements of figures 3.10 and 3.11. The information in figures 3.10 through 3.12 should find application in the evaluation of theoretical models of the response of the main wall.

In order to correlate the main wall response with the debris load,

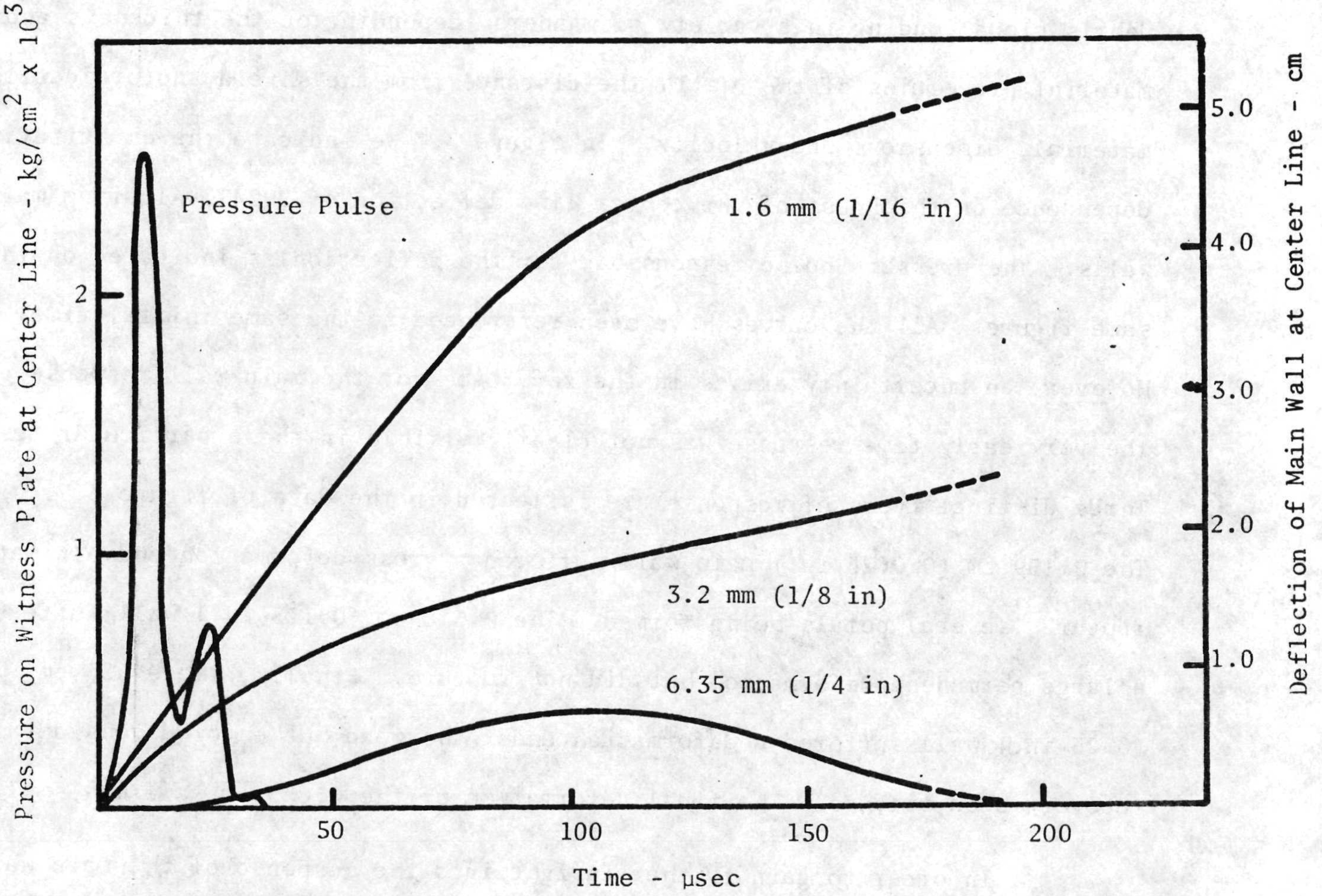

Figure 3.7 Center line response of 2024-T3 aluminum main walls to loading by debris from the impact of a 1.27 cm (0.5 in) diameter by 0.95 cm (0.375 in) long Lexan cylinder onto a 0.25 mm (0.010 in) thick lead shield at 7.6 km/sec (25,000 ft/sec). The main wall was spaced 15.2 cm (6 in) from shield in each test.

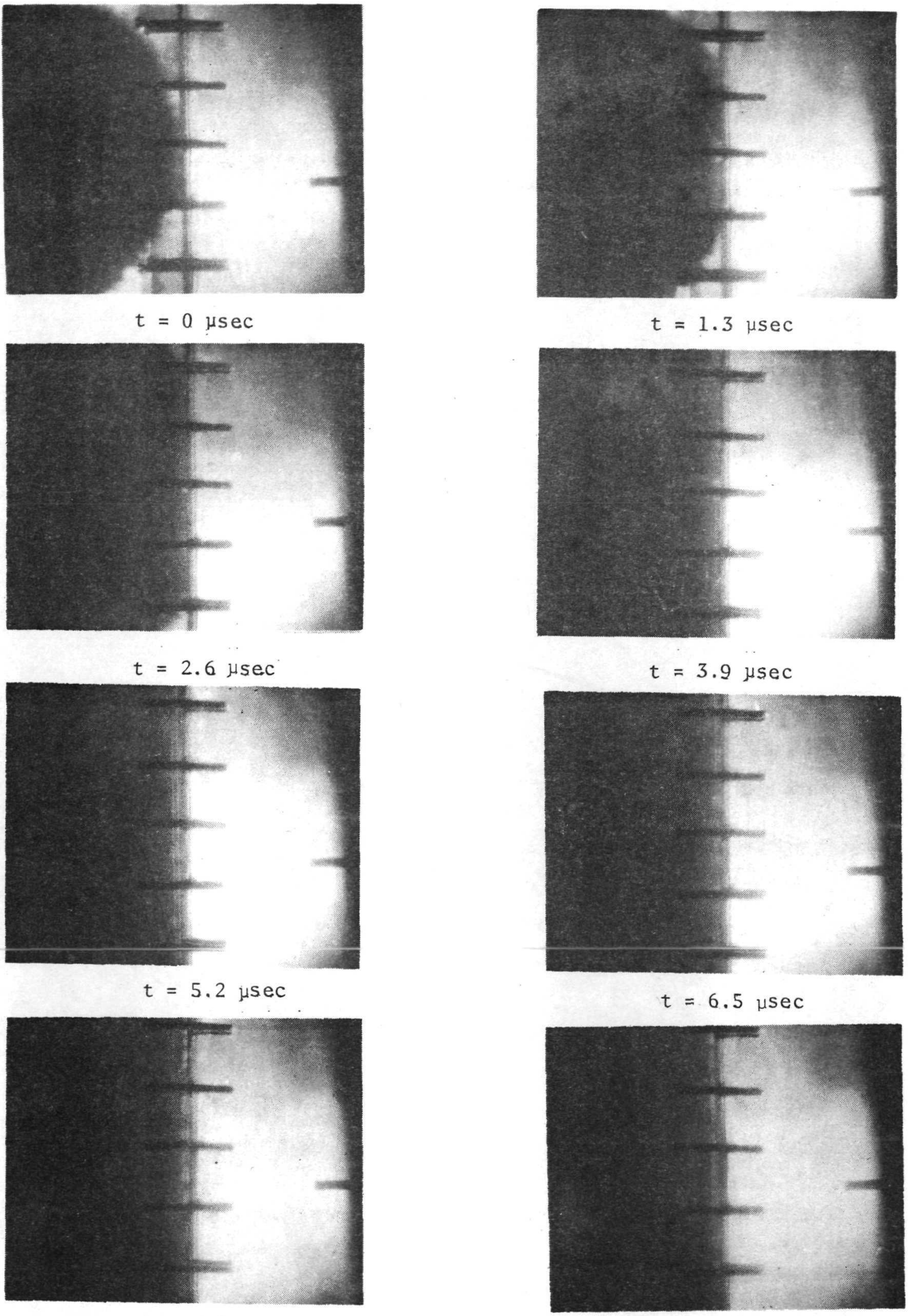

t = 0 μsec

t = 1.3 μsec

t = 2.6 μsec

t = 3.9 μsec

t = 5.2 μsec

t = 6.5 μsec

t = 7.8 μsec

t = 9.0 μsec

Figure 3.8 Response of 1.6 mm (0.063 in) 2024-T3 aluminum main wall to debris of impact of 1.27 cm (0.5 in) diameter by 0.76 cm (0.3 in) long Lexan pellet onto a .25 mm (0.010 in) lead shield at 7.8 km/sec (25,500 ft/sec). Spacing between wall and shield was 15.2 cm (6 in). The debris cloud makes

Figure 3.8 (Cont'd)

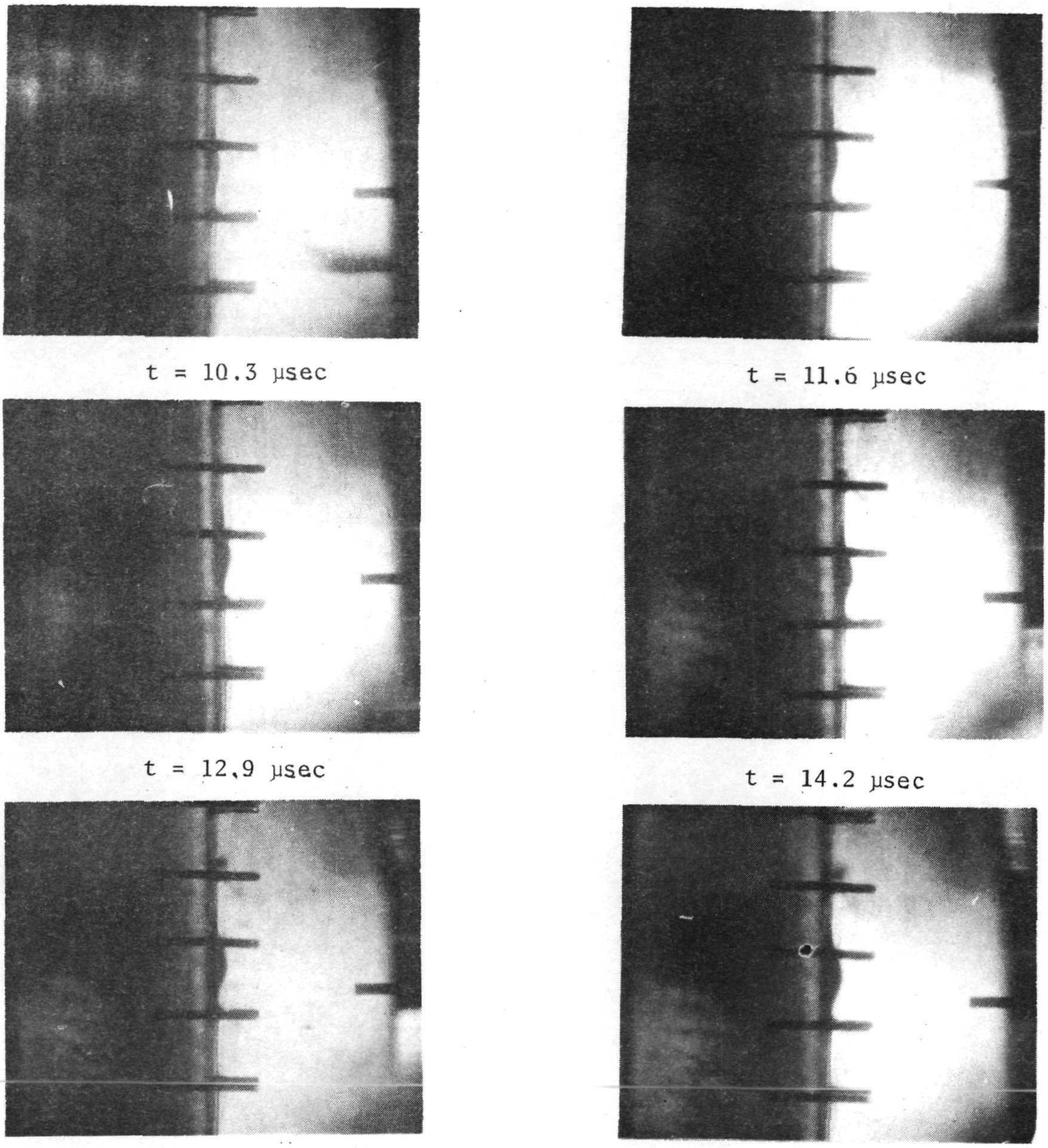

t = 10.3 µsec

t = 11.6 µsec

t = 12.9 µsec

t = 14.2 µsec

t = 15.5 µsec

t = 16.8 µsec

Figure 3.8 (Cont'd)

contact at t = 0. Motion of the wall is not visible until approximately 10 µsec later. Note that the displaced portion of the wall is small compared to the area loaded by the debris cloud.

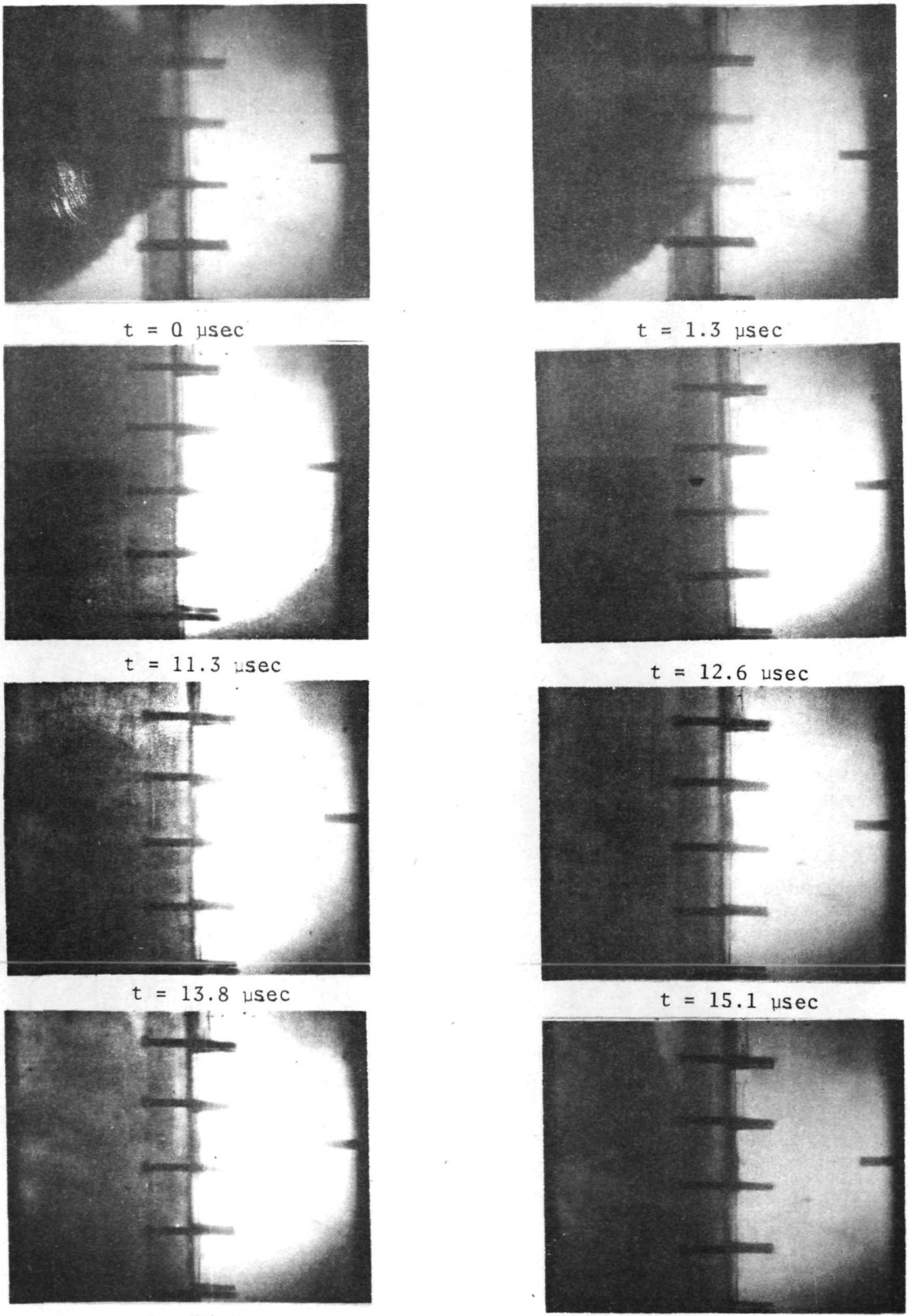

t = 0 μsec

t = 1.3 μsec

t = 11.3 μsec

t = 12.6 μsec

t = 13.8 μsec

t = 15.1 μsec

t = 16.3 μsec

t = 17.6 μsec

Figure 3.9 Response of 3.2 mm (.125 in) 2024-T3 aluminum plate to debris of impact of 1.27 cm (0.5 in) diameter by 0.76 cm (0.3 in) long Lexan pellet onto 0.25 mm (0.010 in) lead shield at 7.9 km/sec (26,000 ft/sec). Spacing between shield and plate was 15.2 cm (6 in)

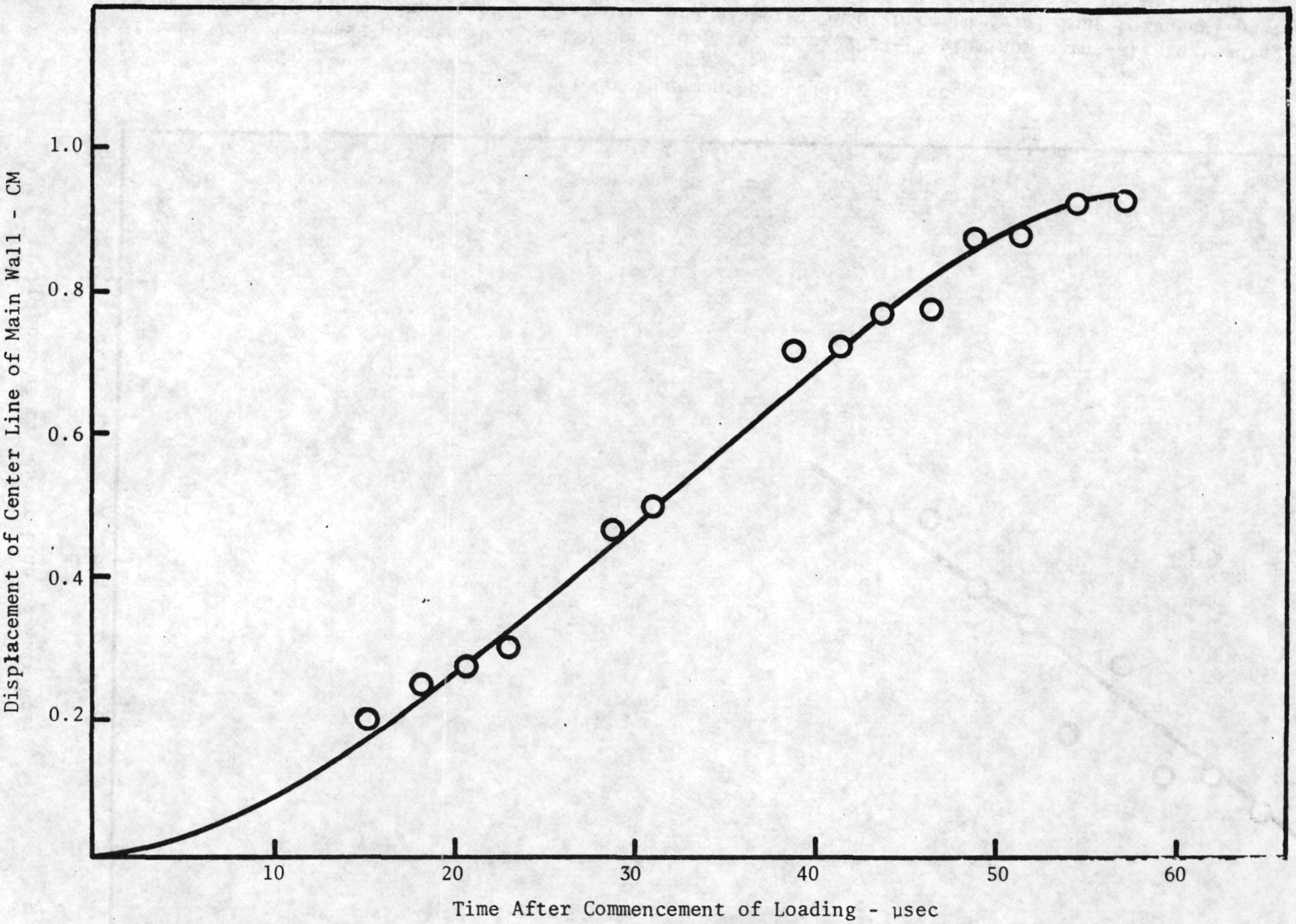

Figure 3.10 Response of center of 0.318 cm (0.125 in) thick 2024-T3 aluminum main wall to loading by debris cloud due to impact of 1.27 cm (0.5 in) diameter by 0.76 cm (0.3 in) long Lexan cylinder onto 0.25 mm (0.010 in) thick lead shield at 7.9 km/sec (26,000 ft/sec). The wall was spaced 15.2 cm (6 in) from shield.

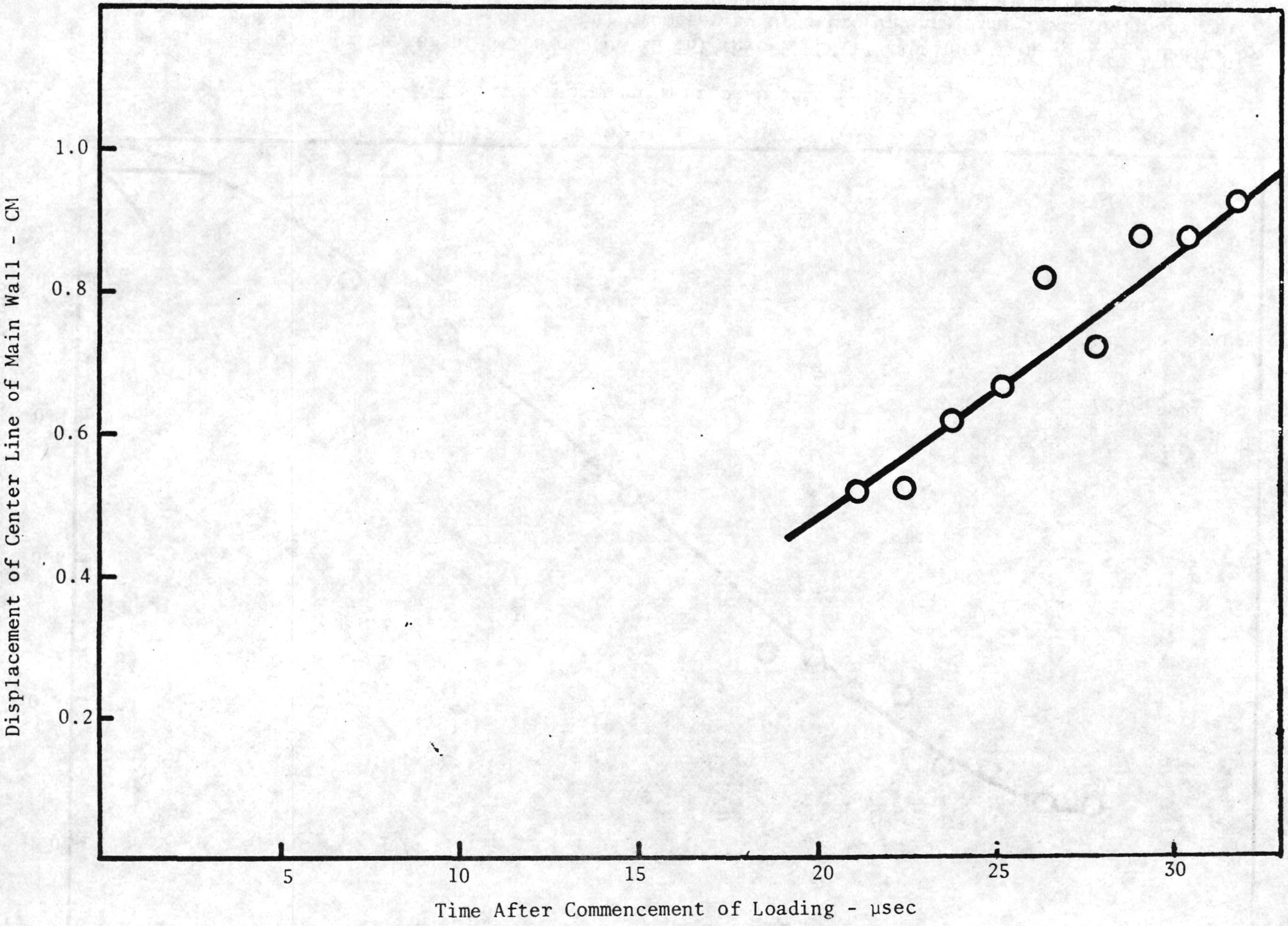

Figure 3.11 Response of center of 0.159 cm (0.063 in) thick 2024-T3 aluminum main wall to loading by debris cloud due to impact of 1.27 cm (0.5 in) diameter by 0.76 cm (0.3 in) long Lexan cylinder onto 0.25 mm (0.010 in) thick lead shield at 7.76 km/sec (25,500 ft/sec). The wall was spaced 15.2 cm (6 in) from shield.

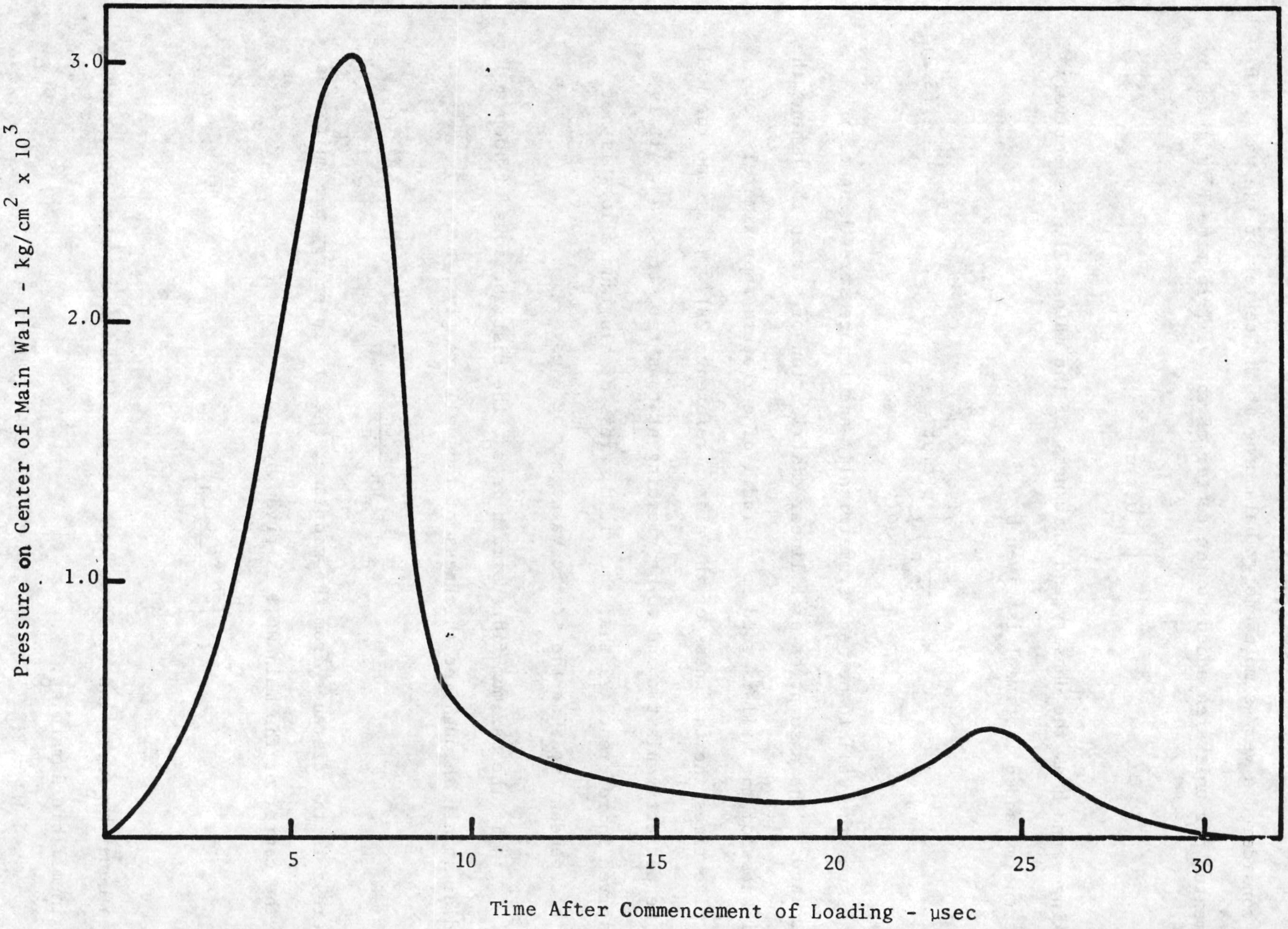

Figure 3.12 Pressure load at center of main wall under loading by debris cloud due to impact of 1.27 cm (0.5 in) diameter by 0.76 cm (0.3 in) long Lexan cylinder onto 0.25 mm (0.010 in) thick lead shield at 7.6 km/sec (25,000 ft/sec). The wall was spaced 15.2 cm (6 in) from shield.

we considered a very simple energy balancing at the center of the wall. The momentum per unit area added to the center of the wall in time T is given by

$$\int_{o}^{T} p(o,t)\,dt \tag{3.1}$$

Taking ρ and h as the density and thickness of the main wall, respectively, the energy added in time T is given by

$$\frac{g_o}{2\rho_w h}\left\{\int_{o}^{T} p(t)\,dt\right\}^2 \tag{3.2}$$

We assume the wall to be bent symmetrically and ignore stretching of the midplane. The assumption of a linear distribution of strain throughout the thickness of the wall is good up to radii of curvature approximately four or five times the thickness of the plate (reference 28). We assume the wall to be perfectly plastic and to be yielding at constant stress σ_o. It is observed in reference 29 that the yield stress of aluminum alloys is not rate dependent so that the static value may be used.

If the maximum fibre strain is ε_o, the distributions of hoop and radial strain through the thickness of the wall are given by

$$\varepsilon_\theta = \varepsilon_r = \frac{2\varepsilon_o z}{h}$$

Where z is the distance from the midplane, the strain energy per unit area at the center of the main wall is given by

$$\int_{-\frac{h}{2}}^{\frac{h}{2}} 2\frac{\varepsilon_o\sigma_o}{h}\,z\,dz = \varepsilon_o\sigma_o h \tag{3.3}$$

Then equating (3.3) and (3.2) we have for a wall which comes to rest with maximum fibre strain ε_o,

$$\frac{g_o}{2\rho_w h}\left\{\int_{o}^{T} p(t)\,dt\right\}^2 = \varepsilon_o\sigma_o h \tag{3.4}$$

If we now suppose that ε_o is the fracture strain, we may convert (3.4) into a ballistic limit equation:

$$h = \sqrt{\frac{g_o}{2\rho_w \varepsilon_o \sigma_o}} \int_o^T p(t)\,dt \tag{3.5}$$

In practice ε_o will not be known as it is the fracture strain in biaxial tension at some elevated rate of strain. Consequently, we may as well consider the entire term under the radical to be unknown and simply regard equation 3.5 as indicating a proportionality between the ballistic limit thickness of the main wall and the impulse loaded at the center. In evaluating the pressure integral we restricted the integration to the first peak, i.e. the gaseous debris. The secondary debris, which consists largely of particles, has a flat distribution at the center and only contributes to the bending of the main wall through interaction with fixed boundaries. In all the ballistic limit studies, the main walls were sufficiently large that failure occurred in a time substantially less than the time required for an acoustic wave to reach the center from the edge. Thus, it is assumed that the particulate debris does not contribute to the observed failure of the main wall at the center.

An effort was made to accumulate a body of ballistic limit data for configurations such as those in figures 3.10 and 3.11. Herein, the ballistic limit is defined to be the thickness of the main wall that just resists penetration by a given debris cloud. This definition is substantially in agreement with that in reference 30, but differs from that used in references 31 and 32. We attempted to hold constant:

(1) Projectile geometry - 1.27 cm (0.5 in.) **diameter** by 0.76 cm (0.3 in) long Lexan cylinder

(2) Shield - 0.25 mm (0.010 in.) lead

(3) Impact Velocity - 7.6 km/sec. (25,000 ft/sec.)

(4) Main wall material - 2024-T3 aluminum

The parameters subject to variation were:

1) Downstream spacing of main wall - 7.61, 15.2, 22.9 or 30.5 cm (3, 6, 9 or 12 in).

2) Main wall thickness at each spacing.

The experimental results are summarized in Table 3.1.

Table 3.1

Impacts onto Unbacked 2024T3 Aluminum Plates Protected by Lead Shields. Nominal Impact Conditions: 1.27 cm (0.5 in.) dia. by 0.76 cm (0.3 in.) Long Lexan Cylinder Impacting onto a .25 mm (0.010 in.) Thick Lead Shield at 7.6 km/sec (25,000 ft/sec)

Shot No.	Spacing		Thickness		Impact Velocity		Final Plate Condition	Momentum Scaled Plate Thickness	
	cm	(in)	mm	(ins)	km/sec	(ft/sec)		mm	(ins)
N67-110	7.6	3	3.22	0.127	8.6	28,200	Failed	2.87	0.113
114	7.6	3	6.55	0.258	8.23	27,000	Failed	6.07	0.239
100	15.2	6	1.55	0.061	7.76	25,500	Failed	1.52	0.060
197	15.2	6	1.73	0.068	7.13	23,400	Failed	1.85	0.073
163	15.2	6	2.08	0.082	7.13	23,400	No Failure	2.24	0.088
119	15.2	6	2.38	0.090	7.78	25,500	No Failure	2.24	0.088
102	15.2	6	3.25	0.128	7.92	26,000	No Failure	3.13	0.123
106	22.9	9	0.89	0.035	7.76	25,500	Failed	0.94	0.037
196	22.9	9	1.04	0.041	7.75	25,400	Failed	1.02	0.040
164	22.9	9	1.27	0.050	7.80	25,600	No Failure	1.24	0.049
104	22.9	9	1.55	0.061	6.70	22,000	No Failure	1.75	0.069
249	30.5	12	0.41	0.016	8.45	27,700	Failed	0.36	0.014
109	30.5	12	0.89	0.035	7.20	23,600	No Failure	0.94	0.037

The first five columns of the table are self-explanatory. In column six we have listed a "momentum scaled plate thickness". This was necessitated by the scatter in impact velocity around the nominal 7.6 km/sec (25,000 ft/sec.) value. Equation 3.5 above indicates the ballistic limit thickness is proportional to the center line impulse in the gas cloud. For small changes in projectile velocity, it is reasonable to expect the impulse to scale directly with momentum. This leads to the parametric dependence of references 33 and 34. If the projectile mass is held constant, this becomes equivalent to velocity scaling. Consequently, the momentum scaled thickness h_M is related to the actual thickness h by the simple relation

$$h_M = \frac{7.6h}{V} \tag{3.6}$$

where V is the impact velocity in km/sec. Equation 3.6 simply states that to the first order, one may regard a slightly slow impact on a given main wall as producing the same terminal condition (failure or no failure) as an impact at nominal velocity on a slightly thicker wall.

In figure 3.13 we have plotted the experimental quantity $I = \int_0^T p(o,t)dt$ against spacing, S, in log - log form. It then appears that

$$I \propto S^{-1.67} \tag{3.7}$$

This, in combination with equation (3.5) indicates that

$$h_{B.L.} \propto S^{-1.67} \tag{3.8}$$

This result is more conservative than theoretically determined ballistic limit results which usually possess an inverse square dependence on spacing. It may well be, however, that the exponent depends on the impact velocity or the target characteristics. Upon determining the structural constant in equation (3.5) by reference to the experimental result at 15.2 cm (6 in),

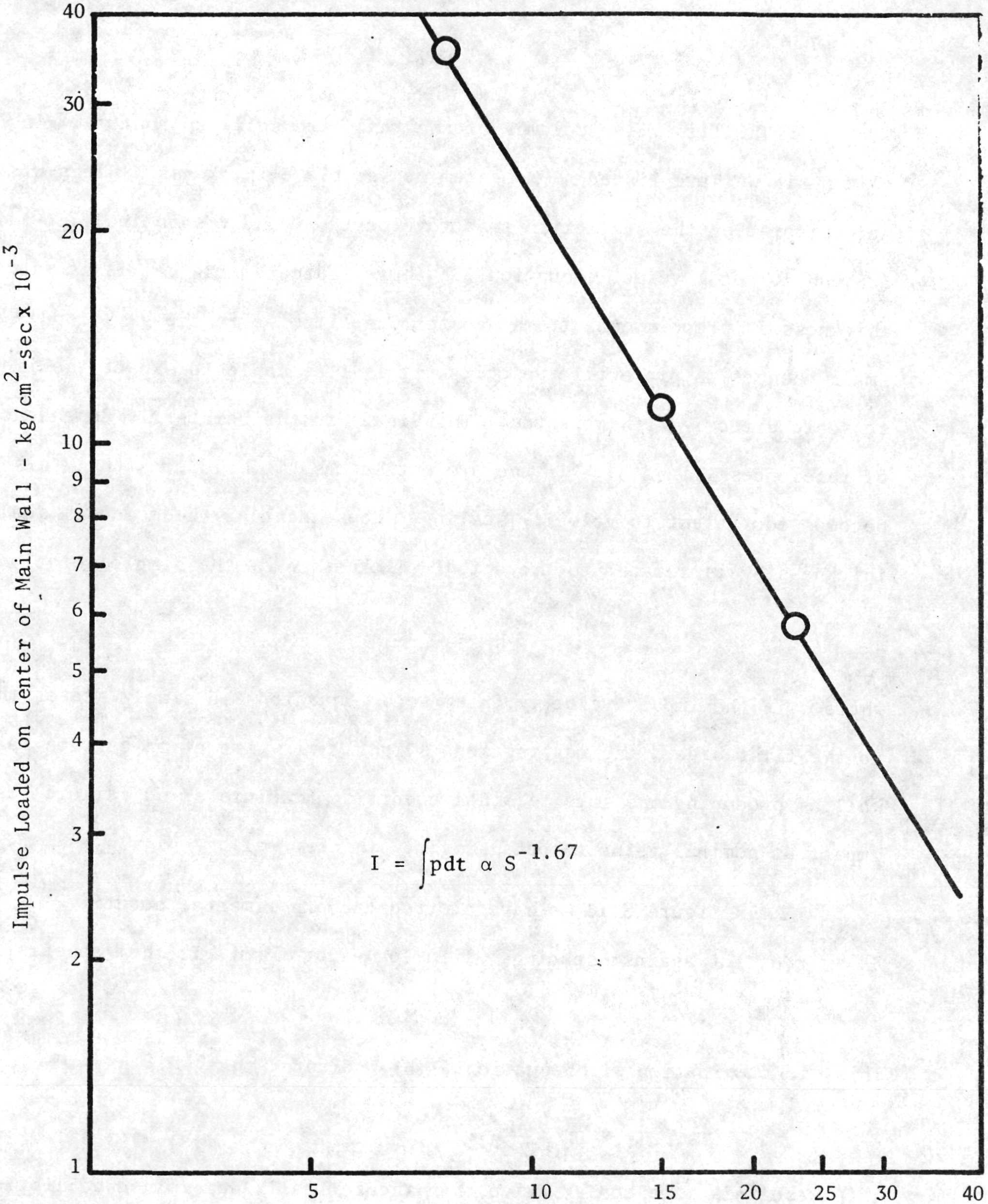

Figure 3.13 Center line impulse in gaseous debris versus spacing from shield. Debris due to impact of 1.27 cm (0.5 in) diameter by 0.76 cm (0.3 in) long Lexan cylinder onto 0.25 mm (0.010 in) lead foil at 7.6 km/sec (25,000 ft/sec).

a spacing dependent equation results for nominal impact conditions and for a particular main wall material (in this case 2024-T3 aluminum)

$$h_{B.L.} = 0.224\left(\frac{15.3}{S}\right)^{1.67} \tag{3.9}$$

where $h_{B.L.}$ and S are in cm. It must be emphasized that the coefficients in equation 3.9 pertain only to the cited impact configuration as only the effects of spacing have been investigated.

In figure 3.14, equation 3.9 is plotted out as a solid line. The data of Table 3.1 are included for comparison. It should be noted that momentum scaled values of the main wall thickness have been used. The agreement is seen to be good, well within the experimental accuracy and supports the idea that the ballistic limit thickness is proportional to the center line impulse. A similar result is found in reference 34. As no experimental measurement was available for the distribution of impulse, reference 34 assumed a distribution and the response of a beam was analysed and related to the problem of the loaded main wall.

In figures 3.15, 3.16 and 3.17 we have illustrated some main walls used in the ballistic limit series. Figure 3.15 is a good example of a catastrophically ruptured main wall. Note the symmetry of the petals. It was found in general that only a very small change in thickness was required to change the ballistic event from no-rupture to catastrophic rupture. The Beckman and Whitley photographic records revealed that when failure occurred, it occurred in a time comparable with the loading time. The failure was detectable on the Beckman and Whitley records by the appearance of a plume of debris transmitted through the rupture in the in the wall. Figure 3.16 shows a main wall that did not fail and

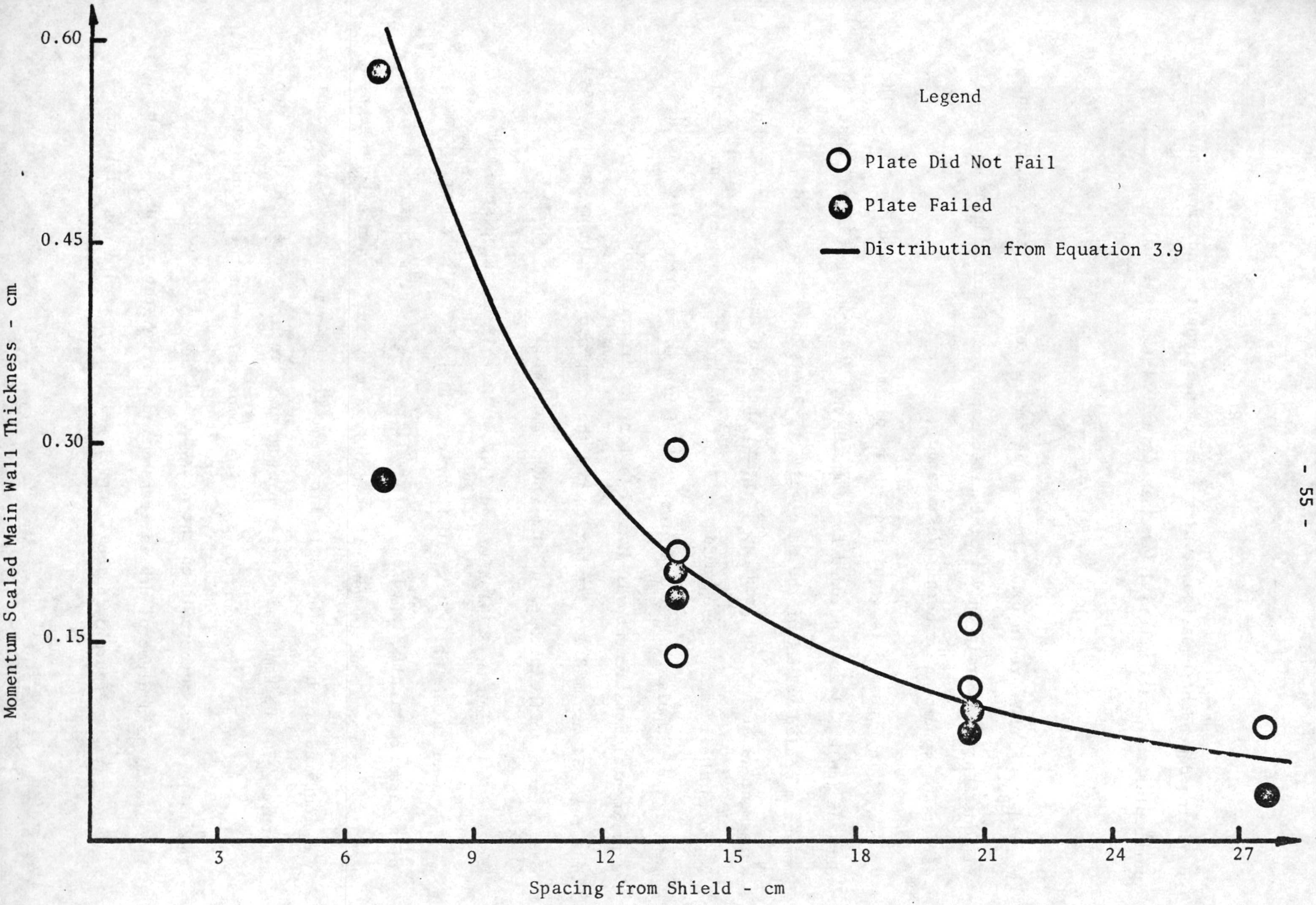

Figure 3.14 Ballistic limit tests with 2024-T3 aluminum main walls. Debris due to impact of 1.27 cm (0.5 in) diameter by 0.76 cm (0.3 in) long Lexan cylinder onto a 0.25 mm (0.010 in) thick lead shield at a nominal velocity of 7.6 km/sec (25,000 ft/sec).

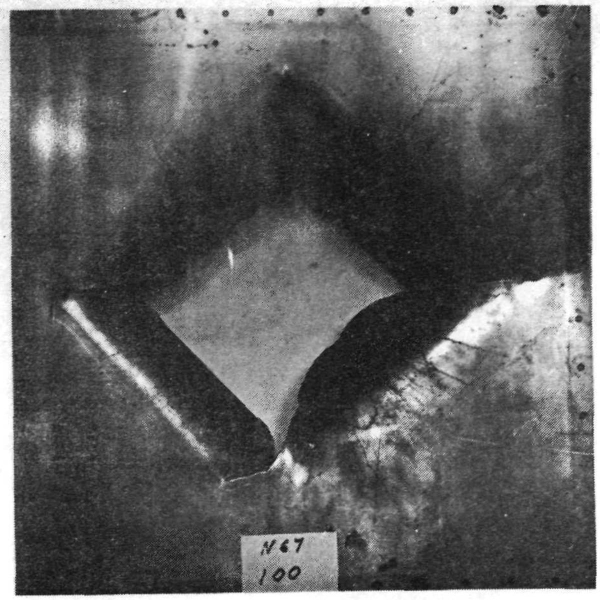

Figure 3.15 Photograph of 1.55 mm (0.001 in) thick 2024-T3 aluminum plate, loaded by debris from impact of 1.27 cm (0.5 in) dia. by 0.76 cm (0.3 in) long Lexan pellet onto 0.25 mm (0.010 in) thick lead shield at 7.76 km/sec (25,500 ft/sec). Spacing from shield was 15.2 cm (6 in)

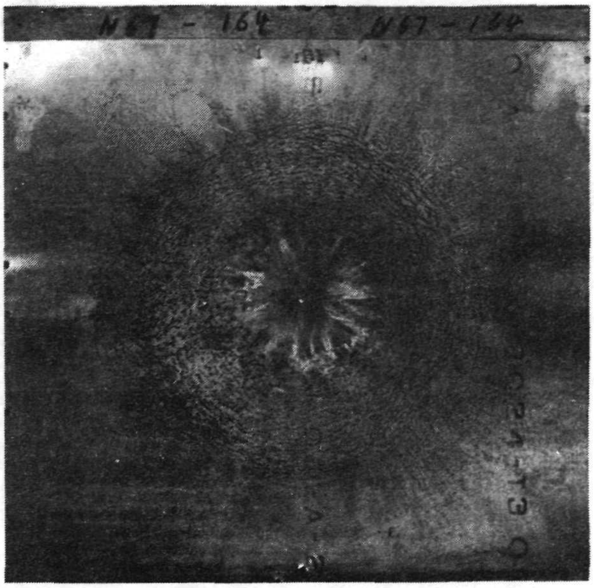

Figure 3.16 Photograph of 1.27 mm (0.050 in) thick 2024-T3 aluminum plate, loaded by debris from impact of 1.27 cm (0.5 in) dia. by 0.76 cm (0.3 in) long Lexan pellet onto 0.25 mm (0.010 in) thick lead shield at 7.80 km/sec (25,600 ft/sec) Spacing from shield was 22.9 cm (9 in)

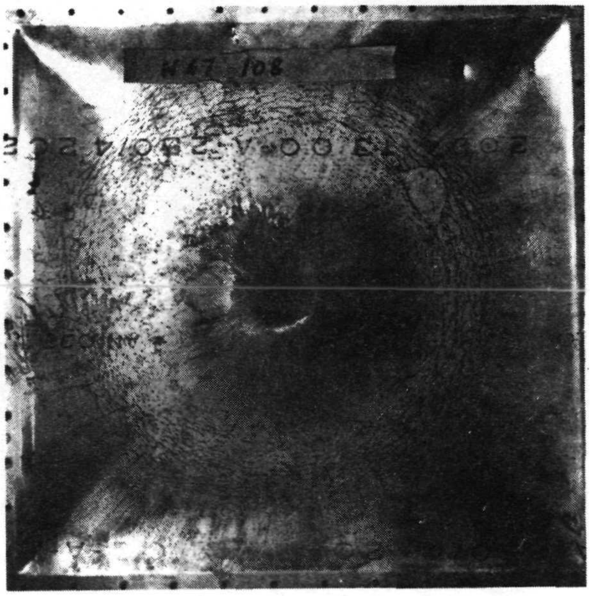

Figure 3.17 Photograph of 0.89 mm (0.035 in) thick 2024-T3 aluminum plate, loaded by debris from impact of 1.27 cm (0.5 in) dia. by 0.76 cm (0.3 in) long Lexan pellet onto 0.25 mm (0.010 in) thick lead shield at approximately 7.5 km/sec (25,000 ft/sec). Spacing from shield was 30.5 cm (12 in)

demonstrates the fineness of fragmentation of the debris.

Figure 3.17 also shows a witness plate that did not fail and is of particular interest because of the configuration into which it is deformed. The configuration can be described by imagining a volcano situated in a valley. This deformation is seen only at large spacings and proved to be quite repeatable. The deformation may be in qualitative agreement with the integrated momentum profiles of reference 35, which show a central minimum for unvaporized debris at large spacings (figure 3.18a). The vaporized debris, however, does not present this behaviour to the same extent and retains a central maximum at large spacings (figure 3.18b). Since the debris which loaded the witness plate of figure 3.17 is expected to have contained both vaporized and unvaporized material, it is possible that the plate was loaded by a combined profile as indicated in figure 3.18c.

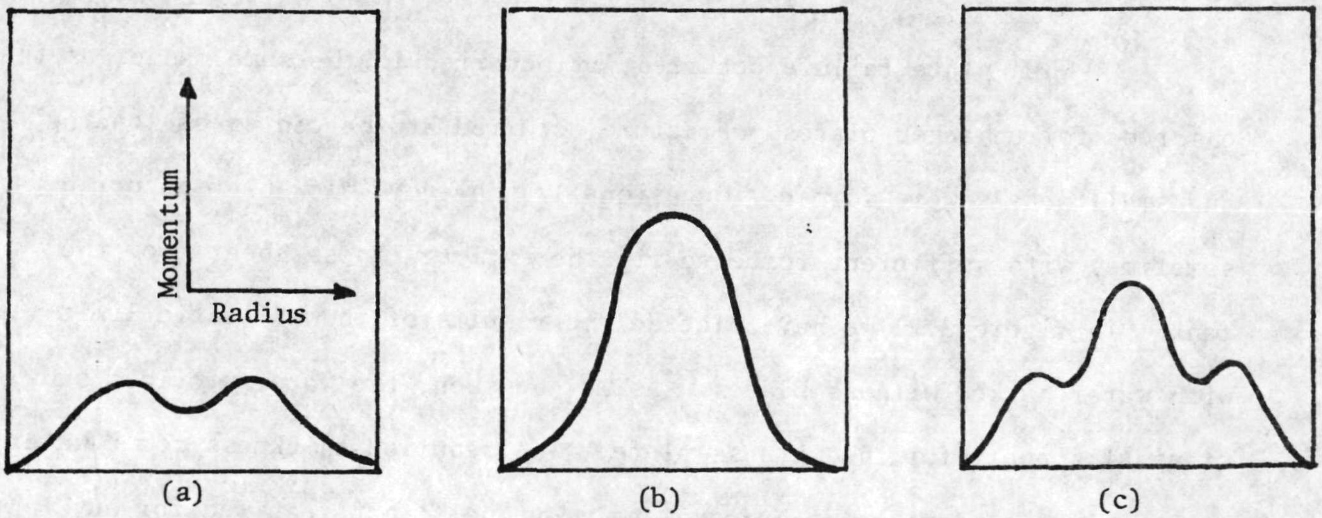

(a)
Low velocity impact
(particulate debris)
from reference 35

(b)
High velocity impact
(vaporous debris)
from reference 35

(c)
Combined profiles for
particulate and vaporous
debris

Figure 3.18 Schematics of Integrated Momentum Profiles Versus Radial Spacing

3.3 Response of Main Wall When Supported by Water

The study of the response of witness sheets to debris cloud loading was completed by a brief investigation of the effect on the response of having a body of water behind the witness plate. In order to observe the approach of the debris cloud as well as the response of the witness plate, a tank having plexiglass sides was fabricated. The tank is illustrated in figure 3.19. The Beckman and Whitley coverage of a typical event is shown in figure 3.20. We see the impact of the projectile onto the shield and the subsequent expansion of the debris cloud. When the debris makes contact with the witness plate, the familiar "impact flash" is observed. No motion of the plate is observed. This agrees with the conclusion of reference 23 that the deflection of a water backed plate will be an order of magnitude less than that of an unbacked plate. Towards the later stages of the coverage, we observe a wave front progressing into the water.

When plate failure occurred, it occurred in the same manner as that observed for unbacked plates. Fracture occurred at the center of loading and small petals were formed. Occasionally, however, blow-back occurred, sometimes with sufficient force to rip the entire witness sheet from the tank. In figure 3.21 we have plotted the results of the ballistic limit tests with water backed witness plates. As may be seen, the water provides substantial support for the witness plate. The required thickness for a water backed plate appears to be approximately one half that required for an unbacked plate. However, a more substantial investigation is required to establish this conjecture over a wide range of impact conditions.

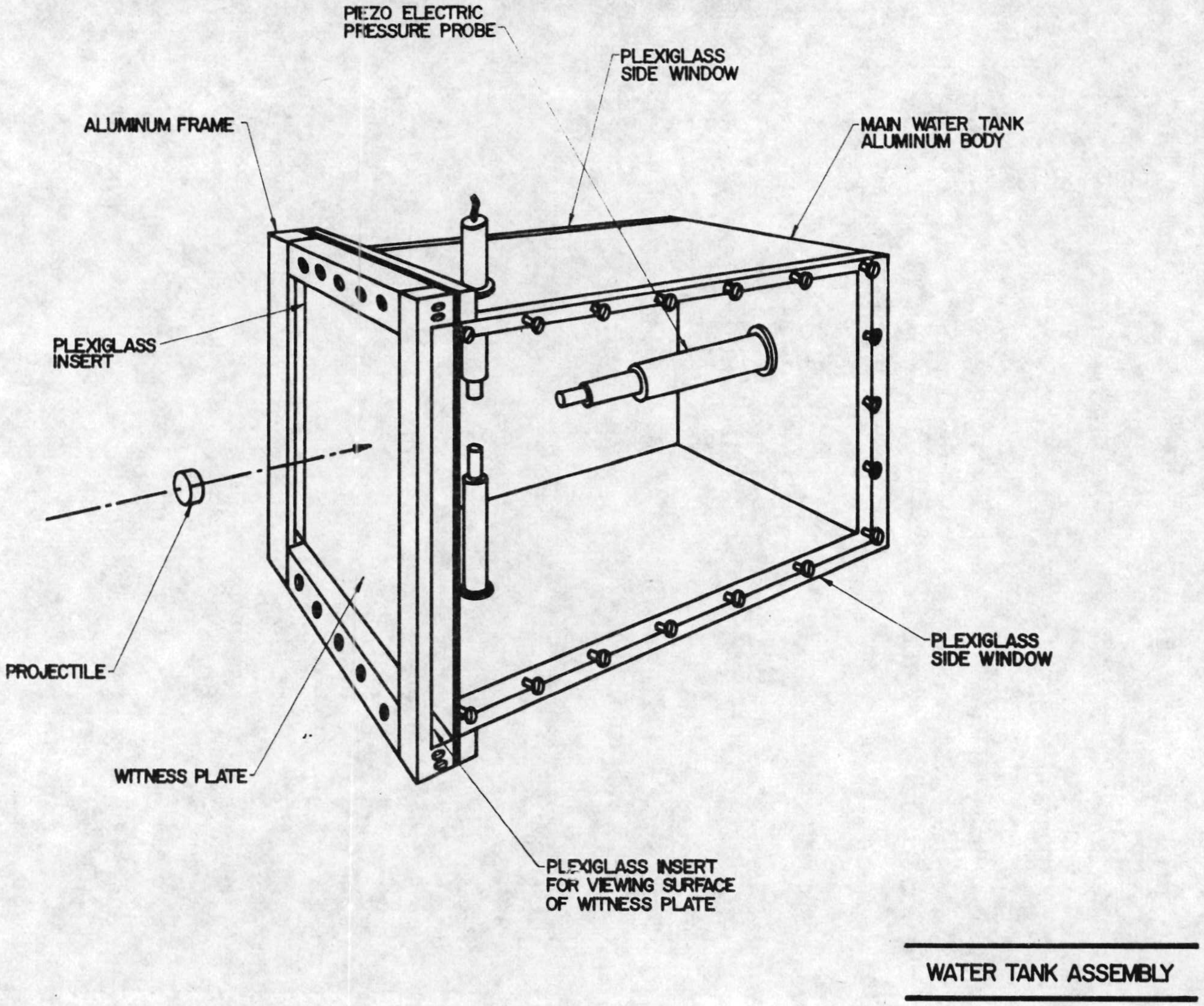

Figure 3.19 Illustration of Tank Utilized in Water Backed Impact Studies

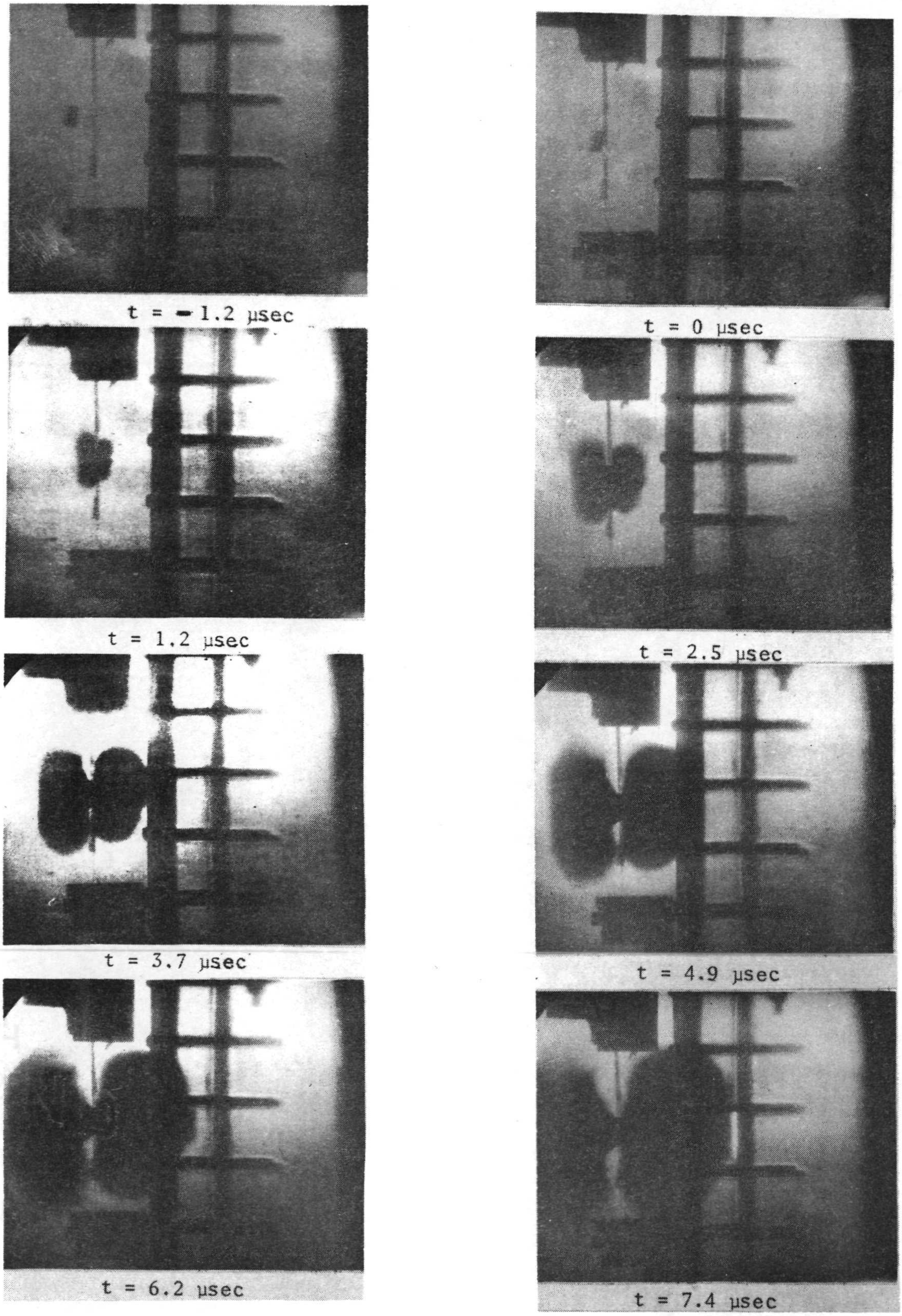

t = −1.2 μsec

t = 0 μsec

t = 1.2 μsec

t = 2.5 μsec

t = 3.7 μsec

t = 4.9 μsec

t = 6.2 μsec

t = 7.4 μsec

Figure 3.20 Beckman and Whitley coverage of response of a .238 cm (3/32 in) thick 2024-T3 aluminum wall, supported from behind by a body of water, to the loading of debris due to the impact of 1.27 cm (0.5 in) diameter by 0.76 cm (0.3 in) long Lexan cylinder onto a 0.25 mm (0.010 in) thick lead shield at 8.0 km/sec (26,200 ft/sec). The wall was spaced 7.6 cm (3 in) from the shield. The projectile impacts onto the shield at t = 0. The

Figure 3.20(Cont'd)

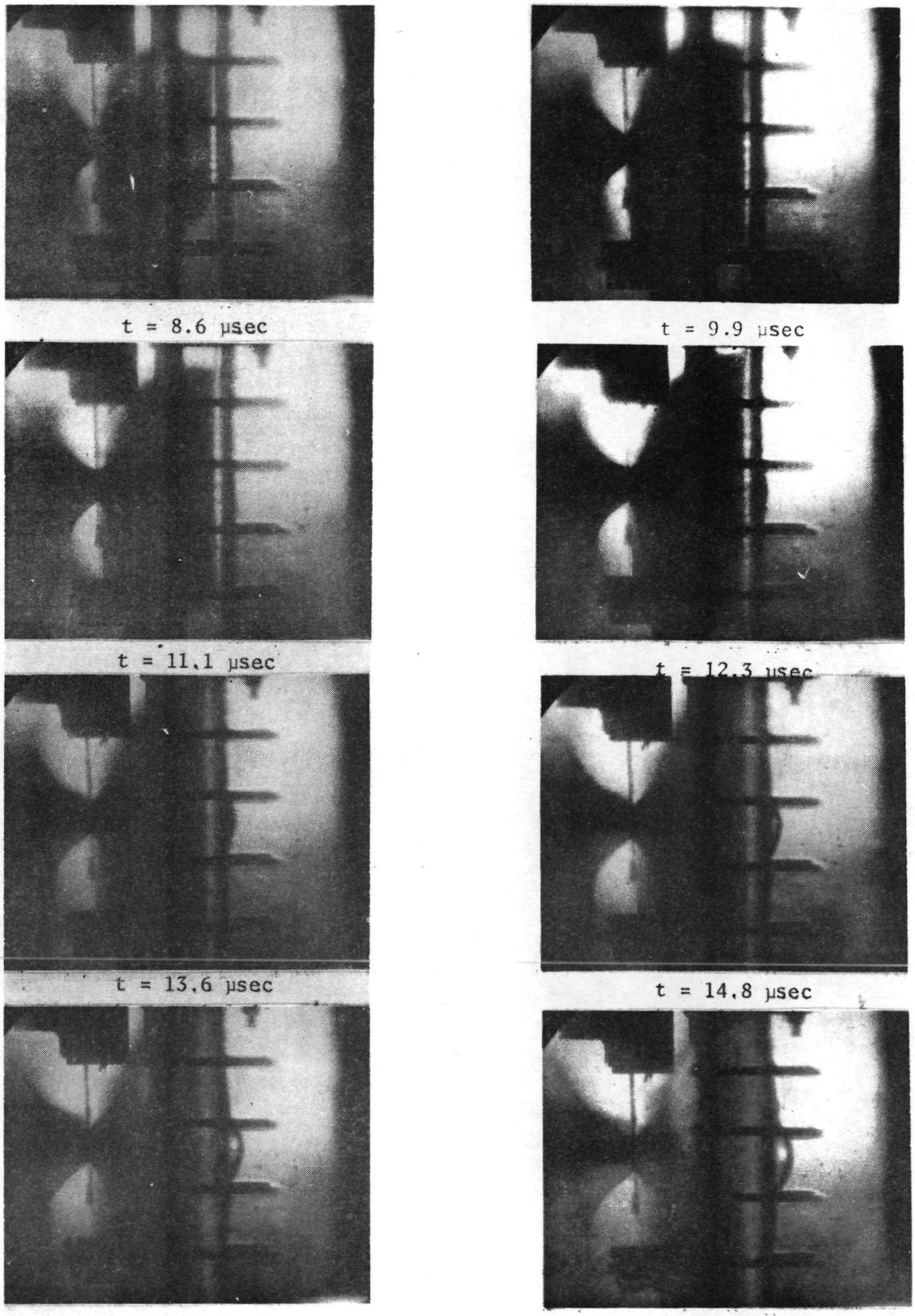

t = 8.6 μsec

t = 9.9 μsec

t = 11.1 μsec

t = 12.3 μsec

t = 13.6 μsec

t = 14.8 μsec

t = 16.0 μsec

t = 17.2 μsec

Figure 3.20 (Cont'd)

resulting debris contacts the main wall approximately 4.0 μsec later. Note the impact flash at t = 7.4 μsec and the development of the shock wave in the water after t = 12.3 μsec

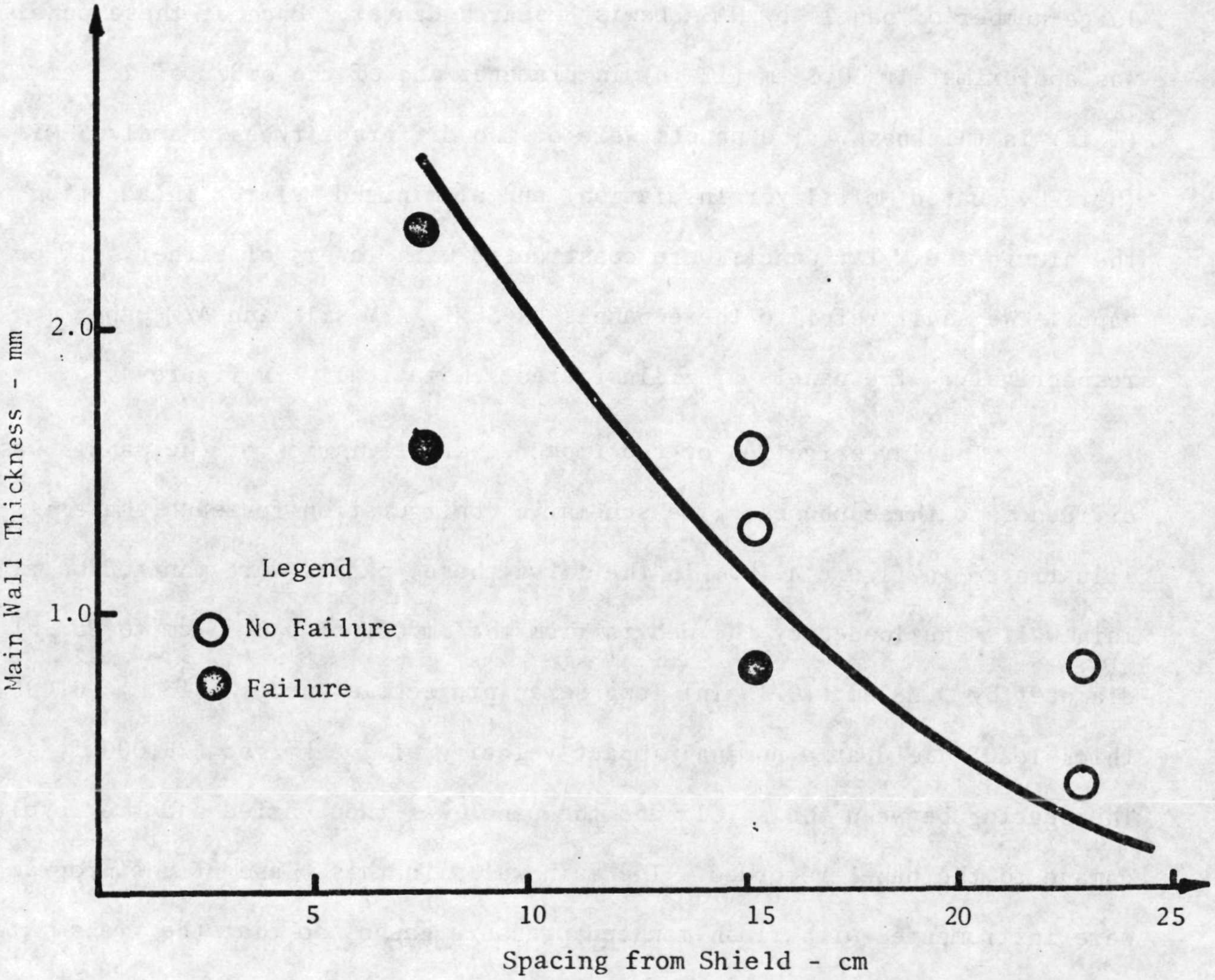

Figure 3.21 Ballistic limit data for water backed 2024-T3 aluminum main wall. The loading in each case was due to the impact of a 1.27 cm (0.5 in) diameter by 0.76 cm (0.3 in) long Lexan cylinder onto a 0.25 mm (0.010 in) thick lead shield at 7.6 km/sec (25,000 ft/sec).

4.0 THE IMPACT CHARACTERISTICS OF CRYOGENIC INSULATION PANELS

The cryogenic tanks used to contain fuel in space missions are shrouded by insulation structures. In order to evaluate the response of typical insulation structures to meteoroid impact, we were furnished with a large number of panels by NASA Lewis Research Center. Each of these panels was approximately 30.5 cm (12 in) in diameter and of the order of 2.5 cm (1 in) in thickness. The panels were of two different types, namely SEMI (Self-Evacuated Multilayer Insulation) and aluminized Mylar. In addition, the aluminized Mylar panels were constructed with layers of either silk or paper. We shall refer to these panels as SEMI, A/M silk and A/M paper respectively. The panels are illustrated schematically in figure 4.1a.

The investigation of the impact characteristics of the panels was divided into three phases. The schematic configuration for each phase is illustrated in figure 4.1b. In the first phase, panels were mounted on rigid main walls and loaded by the debris from the impact of a 0.63 cm (0.25 in) diameter by 0.38 cm (0.15 in) long Lexan projectile onto a 0.13 mm (0.005 in) thick lead shield at a nominal impact velocity of 7.6 km/sec (25,000 ft/sec). The spacing between the shield and the panel was then varied and the resulting damage to the panel recorded. The main walls in this phase of the program were instrumented with flush-mounted pressure gauges so that the transmitted pulse could be compared with that observed without the insulation panel.

In the second phase, the rigid main wall was replaced by a flexible wall (a sheet of 2024-T3 aluminum 0.159 cm (0.063 in) in thickness). Only A/M paper panels were used, the debris load was as in phase one and the object of the tests was to vary the spacing from the shield and determine the response of the main wall. The response of the main wall when protected

SEMI

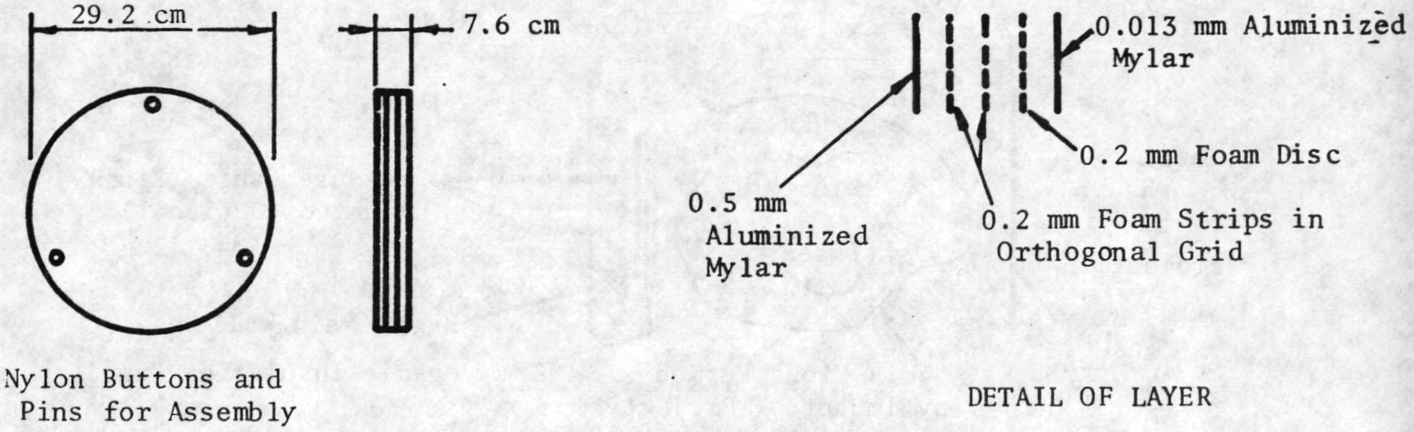

ALUMINIZED MYLAR - SILK

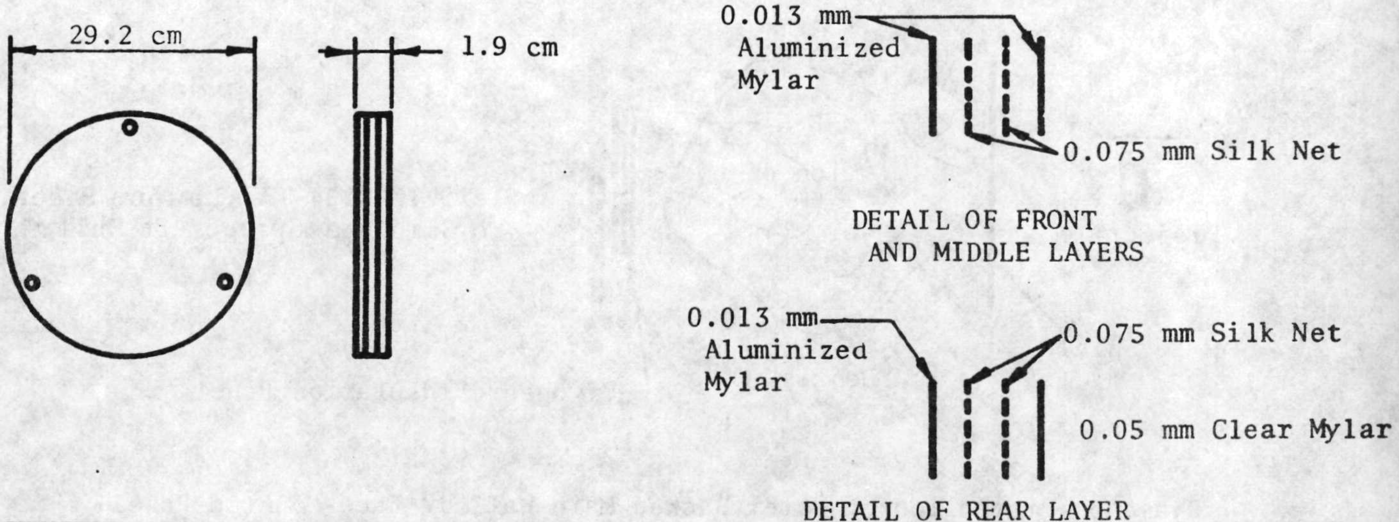

ALUMINIZED MYLAR - PAPER

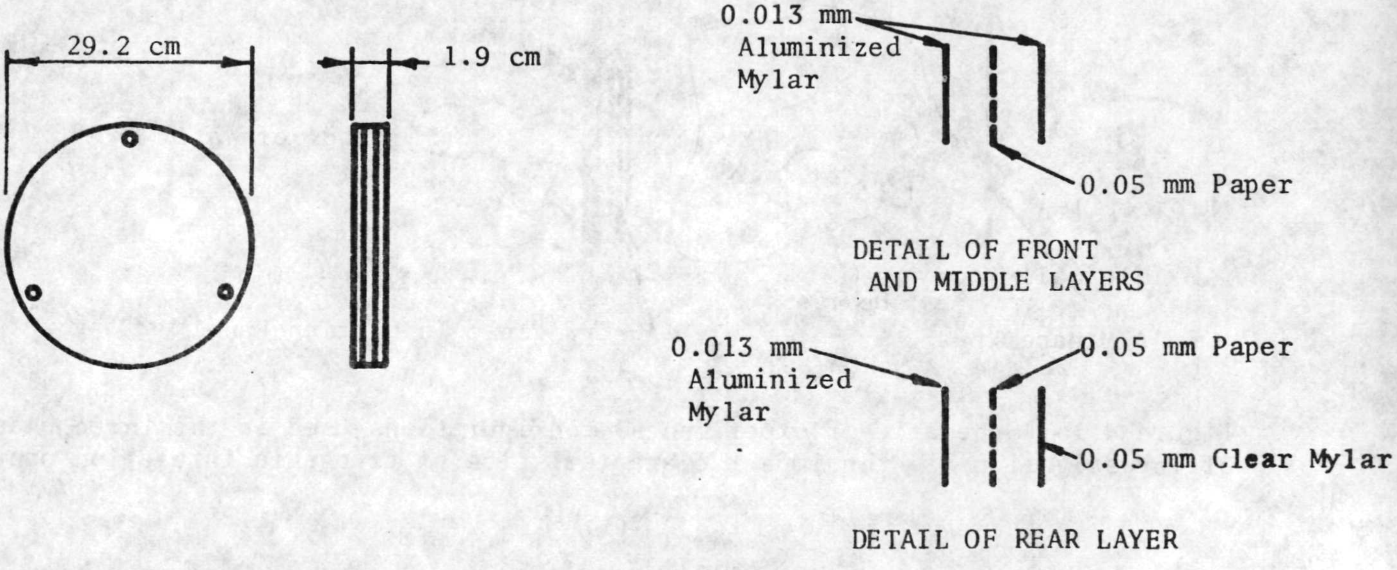

Figure 4.1a Schematics of SEMI and Aluminized Mylar Silk/Paper Cryogenic Insulation Panels as used in Impact Evaluation Testing.

Phase 1 Definition of Damage to Panel

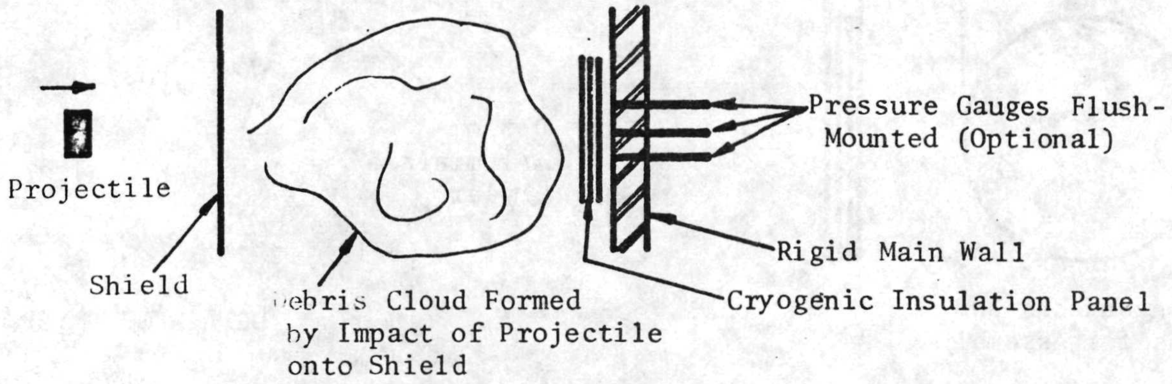

Phase 2 Protection of Main Wall by Face-Mounted Panel

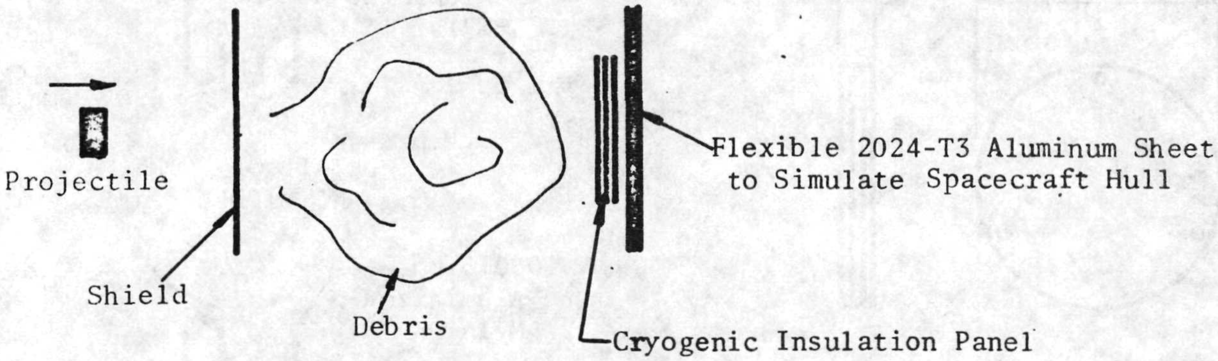

Phase 3 Protection of Water Backed Main Wall by Face-Mounted Panel

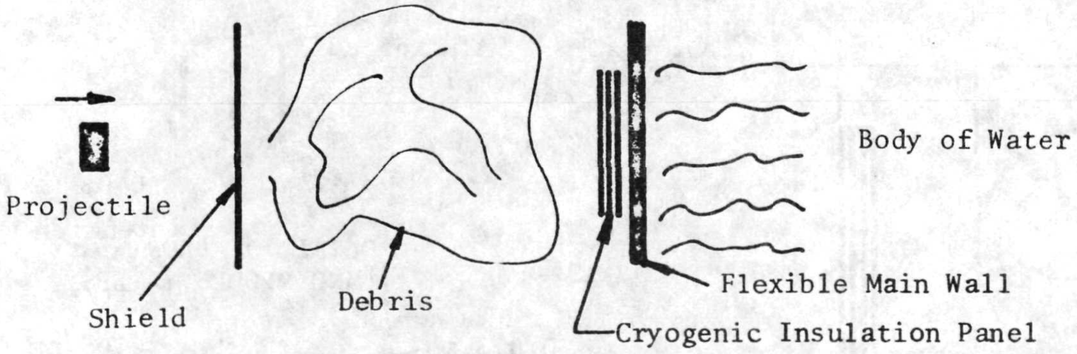

Figure 4.1b Schematic of experimental configurations used in the three phases of investigation of the impact characteristics of cryogenic insulation panels.

by the A/M paper panel was then compared with the response without the panel. The third phase was similar in intent to the second phase, the only difference being that the main wall was further supported by a body of water. The water tank described in Section 3.3 and illustrated in figure 3.19 was utilized for this phase of the program.

Originally, the investigation had called for debris clouds generated by 1.27 cm (0.5 in) diameter Lexan projectiles. However, it was quickly discovered that the panels were far too fragile to support the debris except at very large spacings ($\sim$90 cm). At such large spacings, the debris cloud is substantially larger in cross-section than the insulation panel and the panel no longer models a large surface. Consequently, it became necessary to study the response of the insulation panels to the debris produced by 0.63 cm (0.25 in) diameter Lexan projectiles. This was unfortunate as a large body of experimental data existed to characterize the debris associated with 1.27 cm (0.5 in) diameter projectiles (viz. Section 3 and references 2 and 3) and the response of flexible main wall to the debris load. No such body of information was available for the 0.63 cm (0.25 in) projectile and thus it was necessary to divert some of the effort in the investigation into the characterization of the debris clouds produced by these smaller projectiles.

Experimental difficulties in launching the 0.63 cm (0.25 in) diameter projectile at a consistent velocity and in obtaining reliable instrumentation triggering marred the investigation. As indicated above, the intention was to hold the projectile velocity at a nominal value of 7.6 km/sec (25,000 ft/sec). Observed values ranged from 6.5 km/sec (21,300 ft/sec) to 8.7 km/sec (28,600 ft/sec). The low velocity impacts frequently struck the shield obliquely with the result that a "dirty" debris cloud was formed containing a higher percentage of particulate debri than would be obtained at nominal conditions (see figure 3.16 as an example of a main wall loaded by clean or substantially vaporous debris). The absence of a muzzle trigger on the other hand precluded the successful measurement of impact velocity in several cases.

In figure 4.2 we present photographs of several of the impacted cryogenic insulation panels. We have included a sufficient number from each phase of the investigation to indicate the manner in which the response changes with spacing.

In analysing the results of the first phase of the task, careful interpretation of the damage to the panel was required. Particles are always present in the expansion cloud because of the shock diffraction within the target. Consequently, at close spacings, one may obtain simultaneous perforation of the panel by the vapor and by small particles. As the spacing downstream of the thin shield is increased, the gas cloud damage reduces rapidly until only the particulate penetration pattern is observed. This latter damage is generally confined to a narrow annulus centered about the original flight axis of the projectile. Asymmetries may result, however, from projectile tilt at impact. Nonetheless, particle penetration is always characterized by a narrow and relatively deep hole in the panel. The depth of penetration apparently remains independent of spacing once the spacing is sufficiently large.

The gas cloud damage is identified at close spacings by a hole which has a substantial diameter. As the spacing is increased, the depth of the hole decreases while the diameter increases somewhat. With further increases in spacing, we determined a limiting gas cloud damage which involved tearing of only the outermost one or two layers of the panel. In

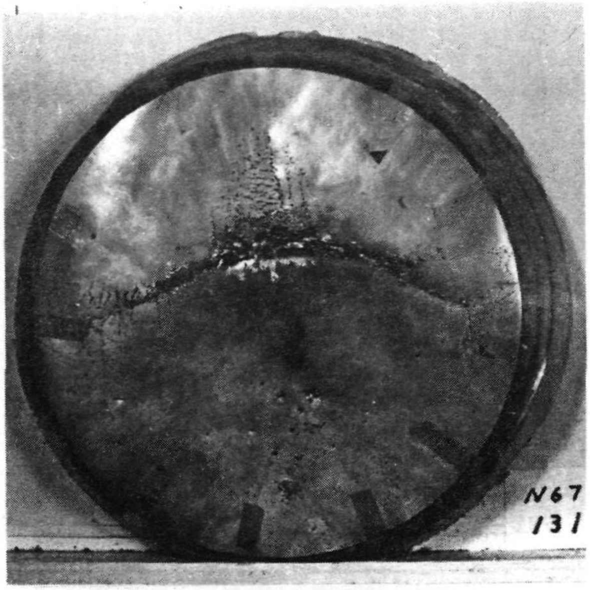

N67-131 SEMI RIGID BACKING
VELOCITY = 6.7 km/sec (22,000 fps)
SPACING = 30.5 cm (12 in)

N67-319 SEMI RIGID BACKING
VELOCITY = ?
SPACING = 30.5 cm (12 in)

N67-320 SEMI RIGID BACKING
VELOCITY = 7.35 km/sec (24,100 fps)
SPACING = 30.5 cm (12 in)

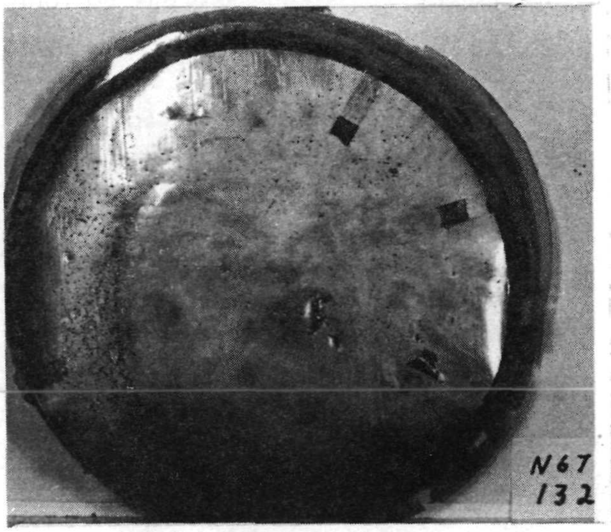

N67-132 SEMI RIGID BACKING
VELOCITY = 6.6 km/sec (21,600 fps)
SPACING = 45.6 cm (18 in)

Figure 4.2 Photographs of impacted cryogenic insulation panels. Debris from impact of a 0.63 cm (0.25 in) dia. by 0.38 cm (0.15 in) long Lexan projectile onto a 0.13mm (0.005 in) thick lead shield at a nominal impact velocity of 7.6 km/sec (25,000 ft/sec)

Figure 4.2 Cont'd

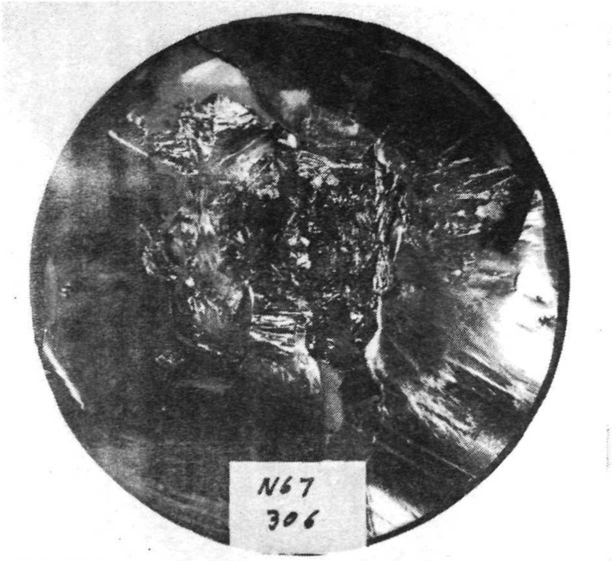

N67-306 SEMI RIGID BACKING
VELOCITY = ?
SPACING = 7.6 cm (3 in)

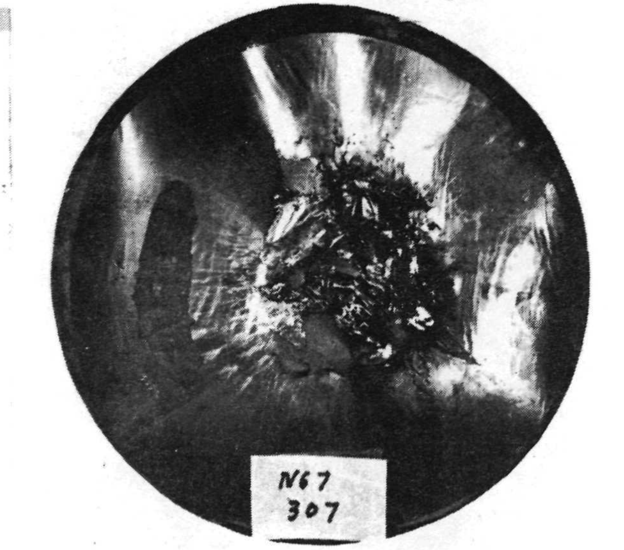

N67-307 SEMI RIGID BACKING
VELOCITY = 8.0 km/sec (26,200 fps)
SPACING = 15.2 cm (6 in)

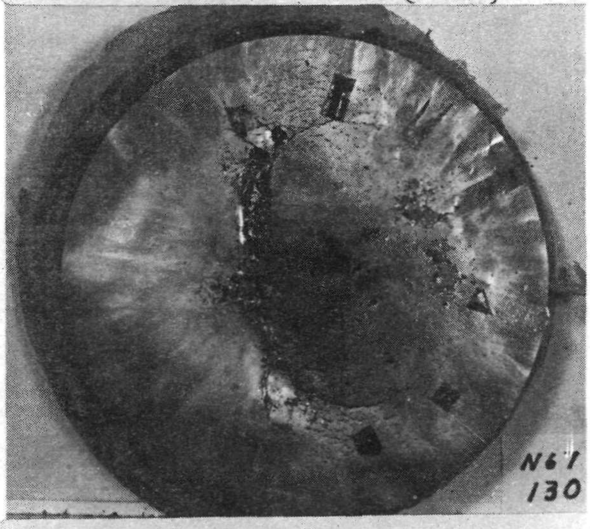

N67-130 SEMI RIGID BACKING
VELOCITY = 6.9 km/sec (22,700 fps)
SPACING = 22.9 cm (9 in)

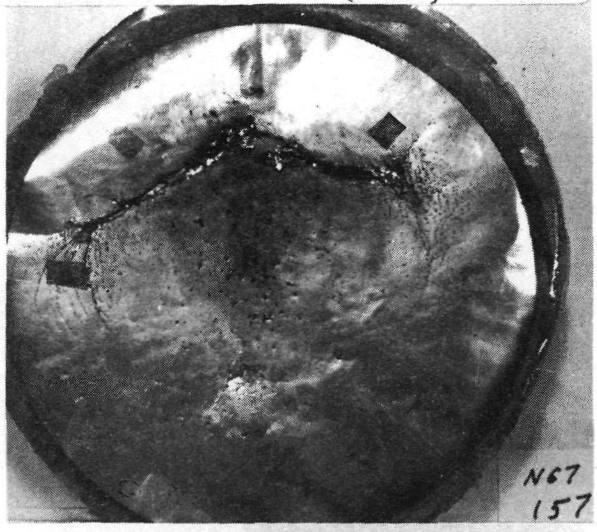

N67-157 SEMI RIGID BACKING
VELOCITY = 8.1 km/sec (26,600 fps)
SPACING = 22.9 cm (9 in)

N67-314 SEMI RIGID BACKING
VELOCITY = ?
SPACING = 22.9 cm (9 in)

N67-318 SEMI RIGID BACKING
VELOCITY = ?
SPACING = 22.9 cm (9 in)

Figure 4.2 Cont'

N67-103 A/M PAPER RIGID BACKING
VELOCITY = 7.15 km/sec (23,500 fps)
SPACING = 7.6 cm (3 in)

N67-101 A/M PAPER RIGID BACKING
VELOCITY = 7.85 km/sec (25,700 fps)
SPACING = 15.2 cm (6 in)

N67-90 A/M PAPER RIGID BACKING
VELOCITY = 7.9 km/sec (25,900 fps)
SPACING = 22.9 cm (9 in)

N67-128 A/M PAPER RIGID BACKING
VELOCITY = 7.5 km/sec (24,600 fps)
SPACING = 22.9 cm (9 in)

N67-92 A/M PAPER RIGID BACKING
VELOCITY = 8.1 km/sec (26,500 fps)
SPACING = 30.5 cm (12 in)

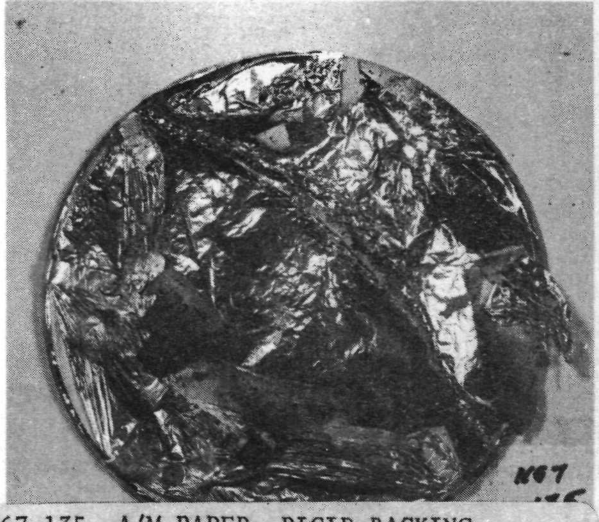

N67-135 A/M PAPER RIGID BACKING
VELOCITY = 7.0 km/sec (23,000 fps)
SPACING = 63.5 cm (24 in)

Figure 4.2 Cont'd

N67-116 A/M SILK RIGID BACKING
VELOCITY = 7.0 km/sec (23,000 fps)
SPACING = 7.6 cm (3 in.)

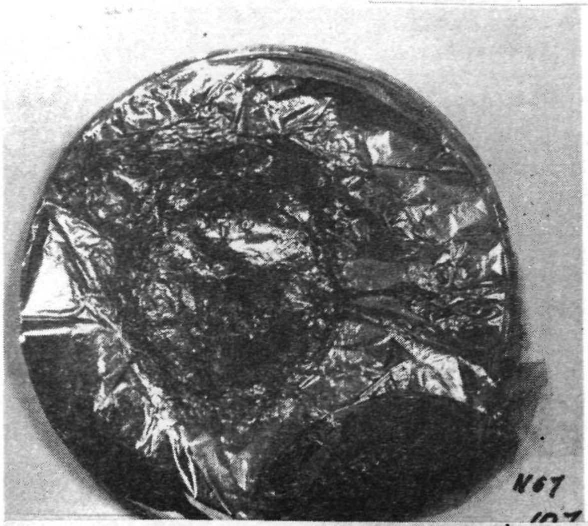

N67-107 A/M SILK RIGID BACKING
VELOCITY = 8.7 km/sec (28,600 fps)
SPACING = 15.2 cm (6 in.)

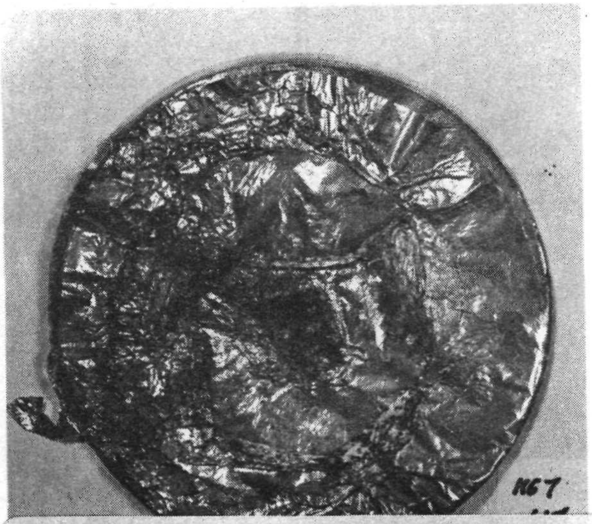

N67-117 A/M SILK RIGID BACKING
VELOCITY = 6.45 km/sec (21,100 fps)
SPACING = 22.9 cm (9 in.)

N67-126 A/M SILK RIGID BACKING
VELOCITY = 8.0 km/sec (26,100 fps)
SPACING = 30.5 cm (12 in.)

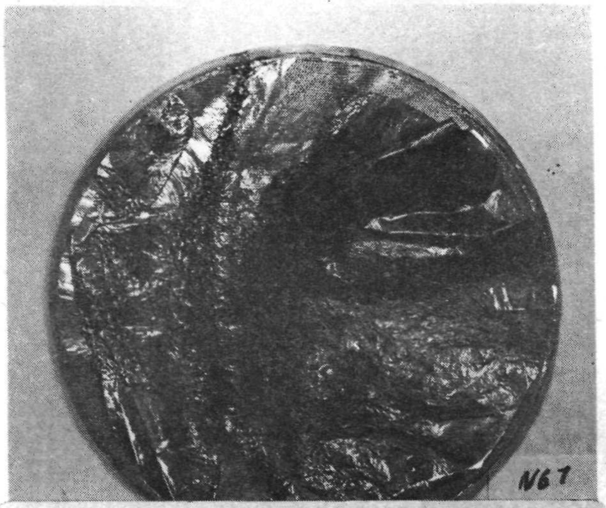

N67-133 A/M SILK RIGID BACKING
VELOCITY = 6.55 km/sec (21,500 fps)
SPACING = 45.6 cm (18 in.)

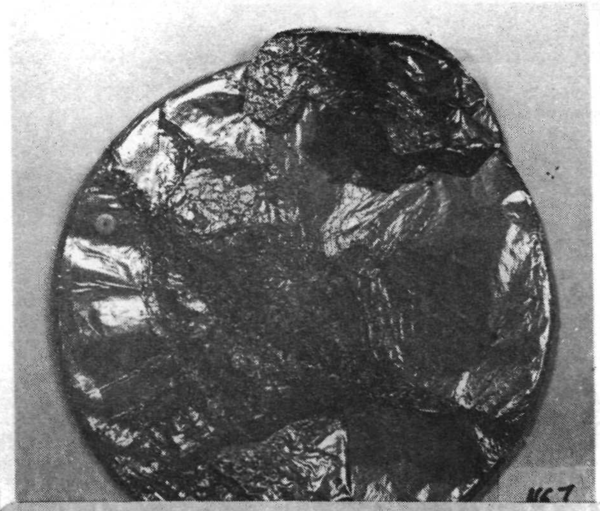

N67-134 A/M SILK RIGID BACKING
VELOCITY = 6.8 km/sec (22,400 fps)
SPACING = 63.5 cm (24 in.)

Figure 4.2 Cont'd

N67-216 A/M PAPER FLEXIBLE BACKING
VELOCITY = 7.2 km/sec (23,600 fps)
SPACING = 3.8 cm (1.5 in)

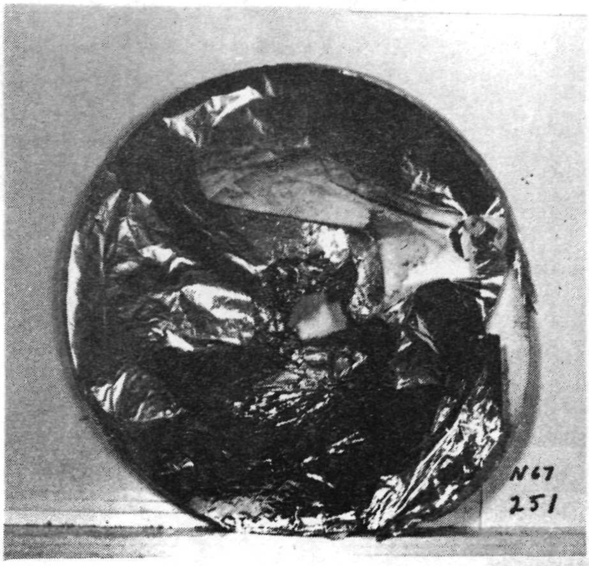

N67-251 A/M PAPER FLEXIBLE BACKING
VELOCITY = 7.0 km/sec (22,950 fps)
SPACING = 6.4 cm (2.5 in)

N67-206 A/M PAPER FLEXIBLE BACKING
VELOCITY = 8.0 km/sec (26,150 fps)
SPACING = 7.6 cm (3 in)

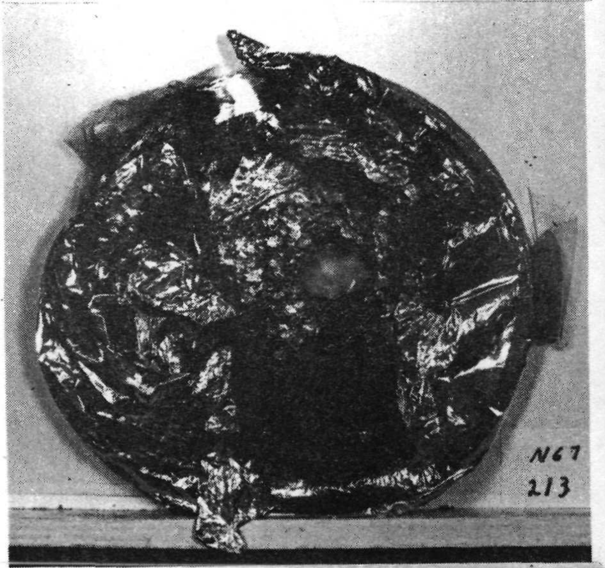

N67-213 A/M SILK FLEXIBLE BACKING
VELOCITY = ?
SPACING = 3.8 cm (1.5 in)

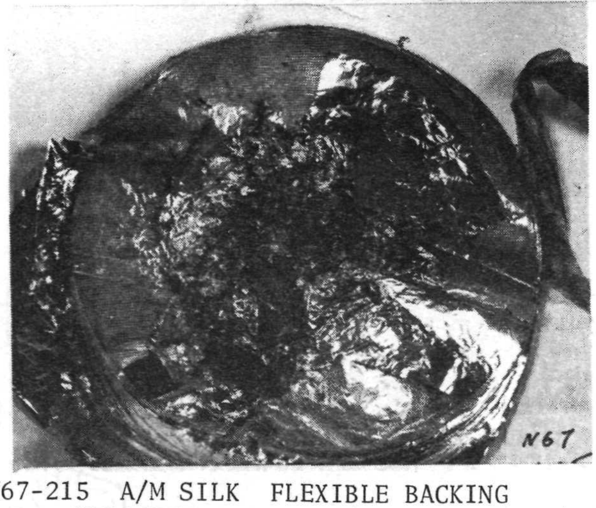

N67-215 A/M SILK FLEXIBLE BACKING
VELOCITY = 7.05 km/sec (23,100 fps)
SPACING = 3.8 cm (1.5 in)

N67-160 A/M SILK FLEXIBLE BACKING
VELOCITY = 8.7 km/sec (28,500 fps)
SPACING = 22.9 cm (9 in)

Figure 4.2 Cont'

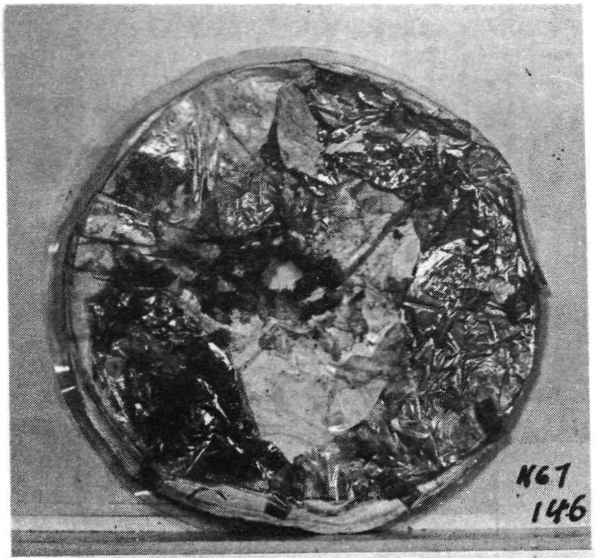

N67-146 A/M PAPER WATER BACKED
VELOCITY = 7.1 km/sec (23,300 fps)
SPACING = 3.8 cm (1.5 in)

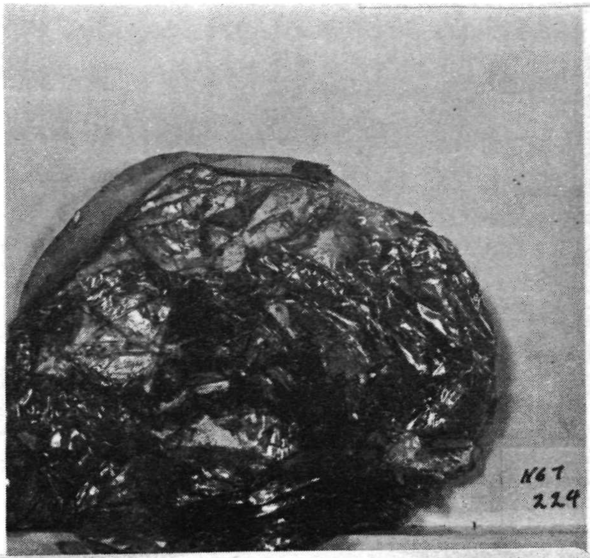

N67-224 A/M PAPER WATER BACKED
VELOCITY = 7.55 km/sec (24,700 fps)
SPACING = 3.8 cm (1.5 in)

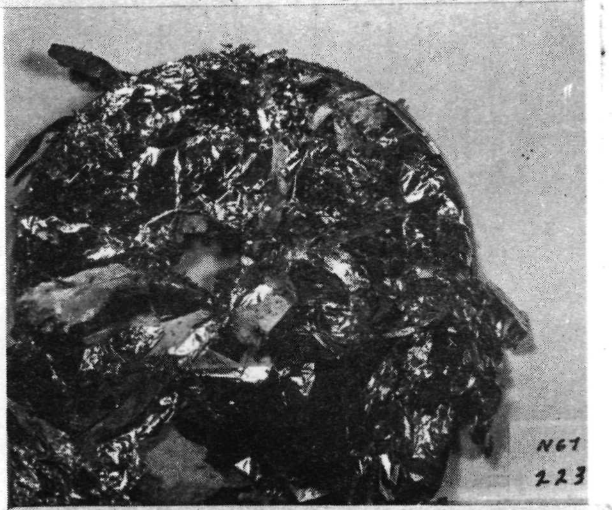

N67-223 A/M PAPER WATER BACKED
VELOCITY = 6.7 km/sec (22,050 fps)
SPACING = 6.7 cm (2.625 in)

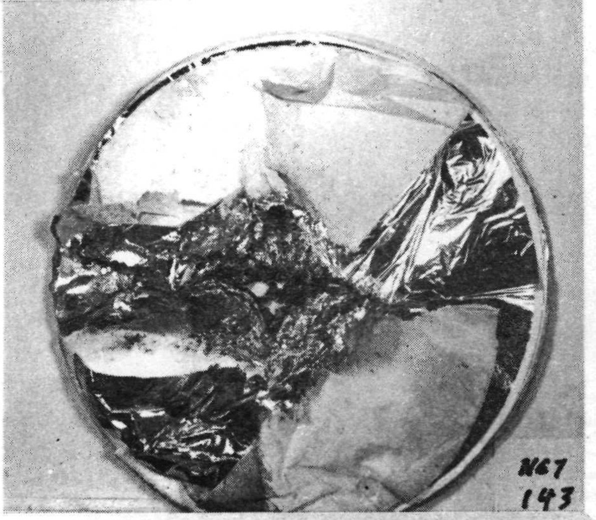

N67-143 A/M PAPER WATER BACKED
VELOCITY = 6.7 km/sec (22,000 fps)
SPACING = 7.6 cm (3 in)

N67-237 A/M PAPER WATER BACKED
VELOCITY = ?
SPACING = 15.3 cm (6 in)

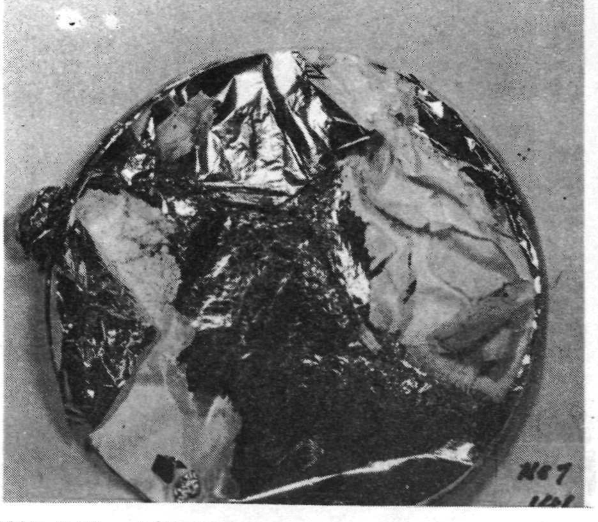

N67-141 A/M PAPER WATER BACKED
VELOCITY = 7.15 km/sec (23,400 fps)
SPACING = 22.9 cm (9 in)

Figure 4.2 Cont'd

N67-148 A/M SILK WATER BACKED
VELOCITY = 7.0 km/sec (23,000 fps)
SPACING = 3.8 cm (1.5 in)

N67-238 A/M SILK WATER BACKED
VELOCITY = ?
SPACING = 6.4 cm (2.5 in)

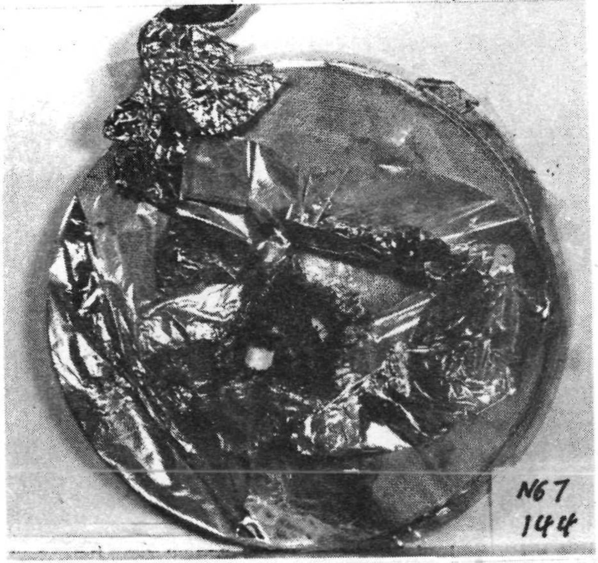

N67-144 A/M SILK WATER BACKED
VELOCITY = 7.6 km/sec (24,850 fps)
SPACING = 7.6 cm (3 in)

N67-142 A/M SILK WATER BACKED
VELOCITY = 7.65 km/sec (25,100 fps)
SPACING = 22.9 cm (9 in)

figure 4.3 we have plotted the number of layers penetrated by the gas cloud versus the downstream spacing. A fairly complete picture of the resistance of the panel to the gas cloud is provided in this manner.

From figure 4.3 it is clear why we chose a no-damage criterion involving damage only to the one or two outer layers. The damage drops very quickly to this level and then remains more or less constant with spacing.

In figure 4.4 we have plotted the peak axial pressure versus spacing in log-log form. A comparison has been made between the debris clouds due to the 1.27 cm (0.5 in) and the 0.63 cm (0.25 in) diameter projectiles. In addition, we observe the effect on the pressure experienced by the main wall of having a cryogenic panel mounted on the plate. It is apparent that the panels have no appreciable effect on the peak pressure. The scatter in pressure reflects the scatter in the impact velocity mentioned previously.

We would expect from this result that the insulation panel would provide negligible protection when mounted on a main wall. This expectation was confirmed by the second phase of the investigation.

We investigated the ballistic limit spacing for a 1.59 mm (0.063 in) thick 2024-T3 aluminum main wall when subjected to the debris from the impact of a 0.63 cm (0.25 in) diameter by 0.38 cm (0.15 in) long Lexan cylinder onto a 0.013 mm (0.005 in) thick lead shield at a nominal velocity of 7.6 km/sec (25,000 ft/sec.). The ballistic limit spacing was found to be between 3.8 cm (1.5 ins) and 6.35 cm (2.5 ins) both with a face mounted A/M panel and without one.

Similar testing with water backed main walls also showed no detectable protection by the cryogenic panel. The data were not sufficiently

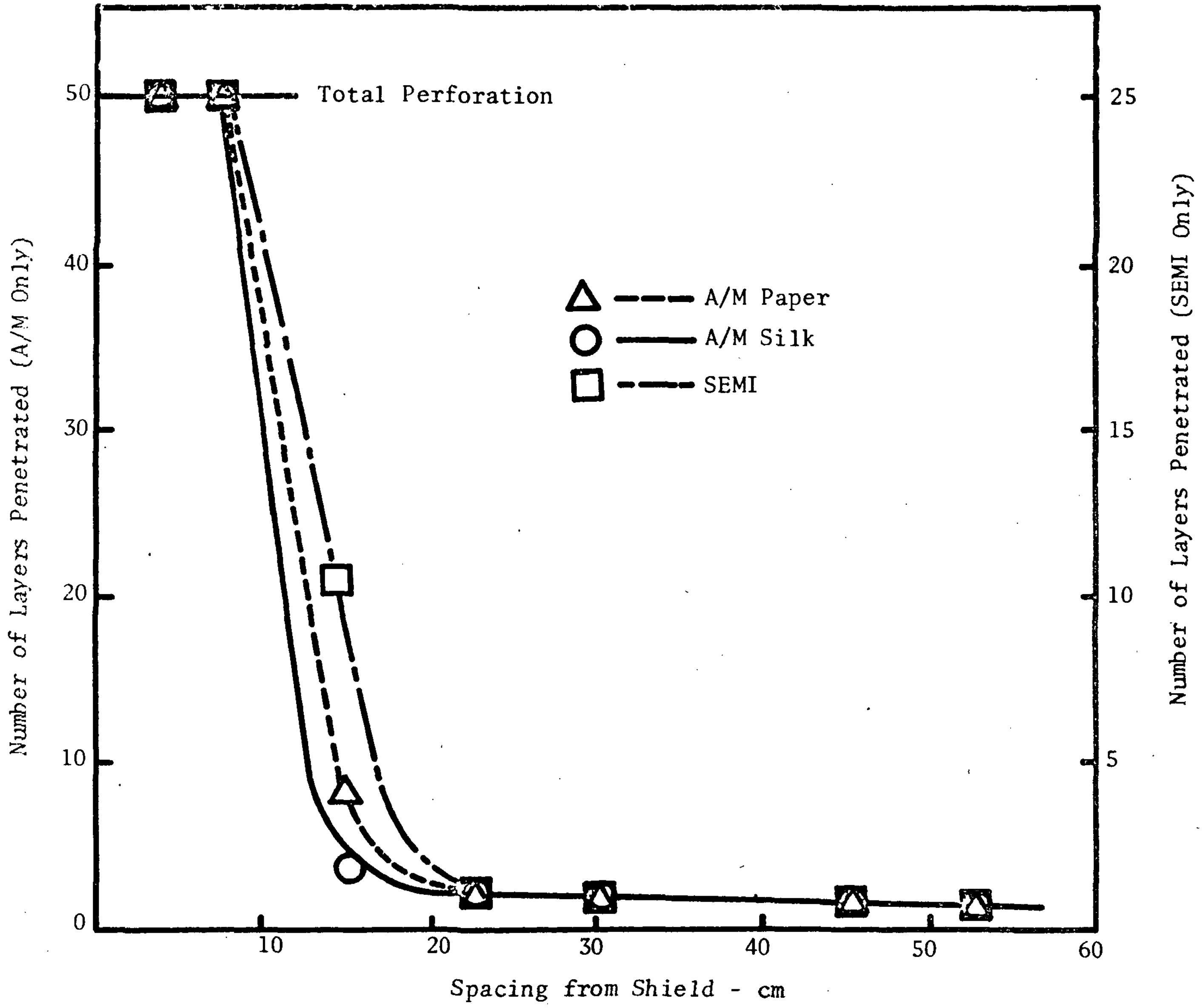

Figure 4.3 Damage to cryogenic insulation panels vs spacing. Damage caused by debris from the impact of a 0.63 cm (0.25 in) diameter by 0.38 cm (0.5 in) long Lexan cylinder onto a 0.12 mm (0.005 in) thick lead shield at a nominal velocity of 7.6 km/sec (25,000 ft/sec).

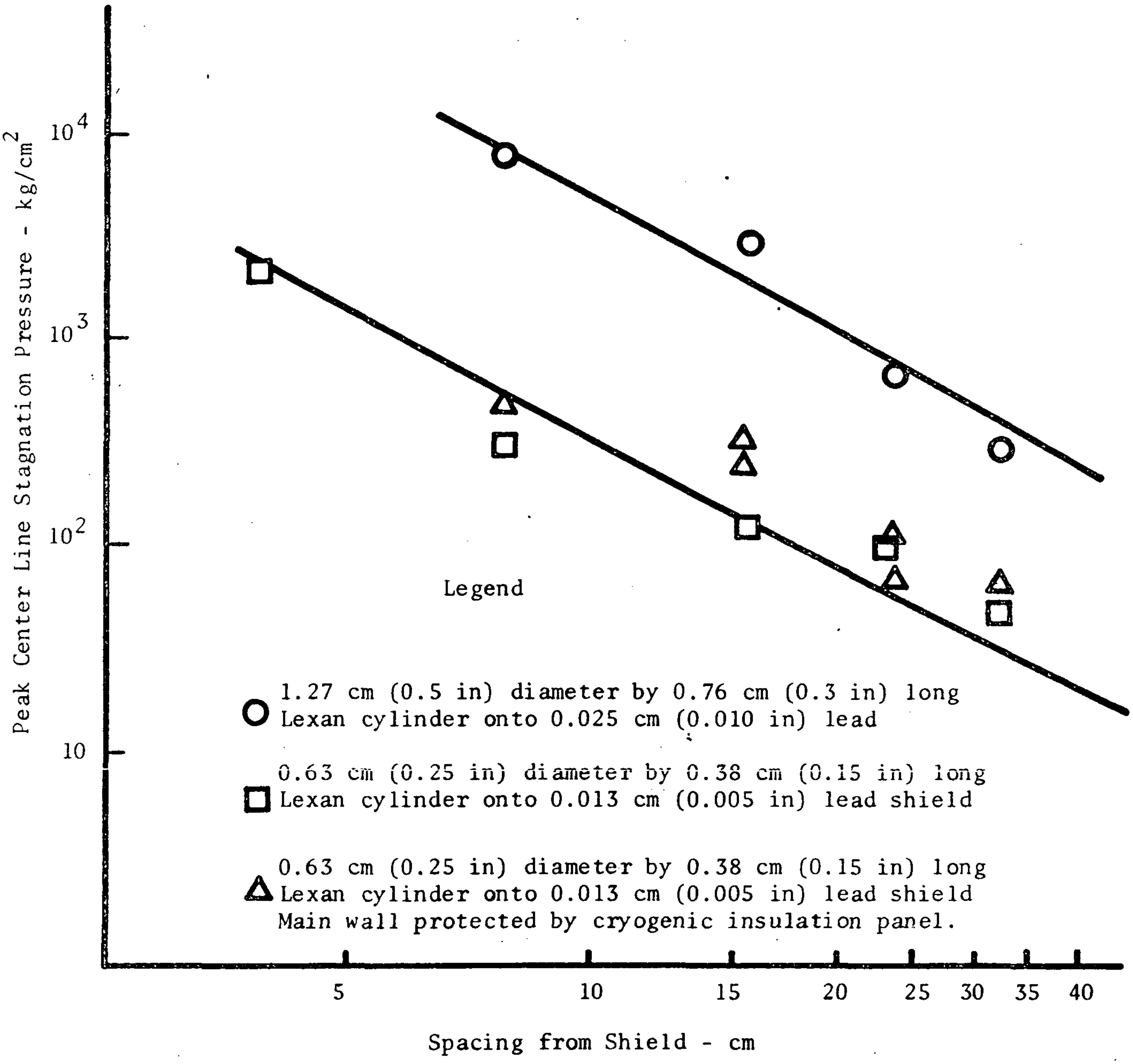

Figure 4.4 Peak center line stagnation pressure versus spacing from shield for impacts at 7.6 km/sec (25,000 ft/sec) nominal, showing the effect of having a cryogenic insulation panel mounted on the main wall.

complete, however, to permit a definition of the ballistic limit thickness.

4.1 Design Charts for Cryogenic Panels in Near-Earth Meteoroid Environment

At the specific request of the NASA Lewis technical monitor, the data available from tests performed in this investigation were extrapolated into design charts. No analysis was made of the shield requirements. It was assumed that a shield would be provided so as to substantially vaporize all meteoroids encountered during a given mission. Thus the extrapolation was based only on the measured pressure distributions. It should also be borne in mind that no cognizance has been taken of particulate penetration of the insulation panel although such effects will be present at all velocities and shield to panel spacings.

If we attempt to correlate the nominal no damage threshold spacing of figure 4.3 with the peak axial pressure, we find from figure 4.4 that S = 22.9 cm (9 in) corresponds to a pressure of ∿ 63.5 kg/cm^2 (900 psi) when the 0.63 cm (0.25 in) diameter projectile is used. Further, if d is the diameter of the projectile, the data of figure 4.4 indicate that

$$P_{max} \propto S^{-2} d^{3.8}$$

In section 6.0 of this report, we present data for the Grid-Bumper which indicate a linear dependence of peak pressure on velocity. Further it is assumed that P_{max} has a linear dependence on projectile density. Hence we write

$$P_{max} = A\rho V S^{-2} d^{3.8} \qquad (4.1)$$

where P_{max} = peak center line pressure in kg/cm^2

ρ = density of projectile in gm/cm^3

V = velocity of projectile in km/sec.

S = spacing between shield and main wall in cm

d = projectile diameter in cm

A = constant of proportionality

We may determine A by reference to a point on either of the curves of figure 4.4. We have

$$P_{max} = 63.5\ kg/cm^2$$

$$\rho = 1.2\ gm/cm^3$$

$$V = 7.6\ km/sec.$$

$$S = 22.9\ cms$$

$$d = 0.625\ cms$$

so that $A = 21,800$

We represent the particle mass in the form

$$M = \frac{\pi\rho}{6} d^3$$

where M is in gms.

Then, using equation (4.1)

$$M = \frac{\pi\rho}{6} \left(\frac{P_{max}}{A\rho V}\right)^{0.79} S^{1.58} \tag{4.2}$$

Equation (4.2) specifies the largest particle mass of known density and velocity which will be defeated by a panel spaced S cms from a shield. To select a spacing which will provide a given mission success probability, we require information about the meteoroid environment.

From reference 36, the design environment is represented by the cumulative flux shown in figure 4.5 together with the conditions

$$\begin{aligned} \rho &= 0.5 \text{ gm/cm}^3 \ (0.0181 \text{ lbm/in}^3) \\ V &= 20 \text{ km/sec. } (66{,}500 \text{ ft/sec.}) \end{aligned} \tag{4.3}$$

We represent the flux distribution of figure 4.5 by the equations

$$N = \begin{cases} 5.75 \times 10^{-9} M^{-0.32} & M \leq 10^{-7} \text{ gm} \\ 3.98 \times 10^{15} M^{-1.2} & M \geq 10^{-7} \text{ gm} \end{cases} \tag{4.4}$$

Substituting $P_{max} = 63.5 \text{ kg/cm}^2$ and ρ and V as specified in equation (4.3) into equation (4.2) yields

$$M = 0.45 \times 10^{-3} S^{1.58} \tag{4.5}$$

Equation (4.5) may be substituted into equation (4.4) to determine the number of particles per meter^2-sec which will substantially or completely penetrate an insulation panel spaced a distance S from a shield

$$N = \begin{cases} 6.79 \times 10^{-8} S^{-0.505} & S \leq 4.72 \times 10^{-3} \text{ cm} \\ 4.16 \times 10^{-11} S^{-1.9} & S \geq 4.72 \times 10^{-3} \text{ cm} \end{cases} \tag{4.6}$$

Then, if E is the mission area-time product in meter^2 - sec, EN(S), where N(S) is defined by equation (4.6), represents the expected number of particles sufficiently large to damage the insulation system spaced a distance S from the shield. We fit the distribution to a Poisson form with mean $\mu = EN$.

$$\text{i.e.} \quad P(n) = \frac{\mu^n e^{-\mu}}{n!} \tag{4.7}$$

gives the probability that n punctures will occur. The probability of zero punctures (n = o) is given by

$$P(o) = e^{-\mu} = e^{-EN} \tag{4.8}$$

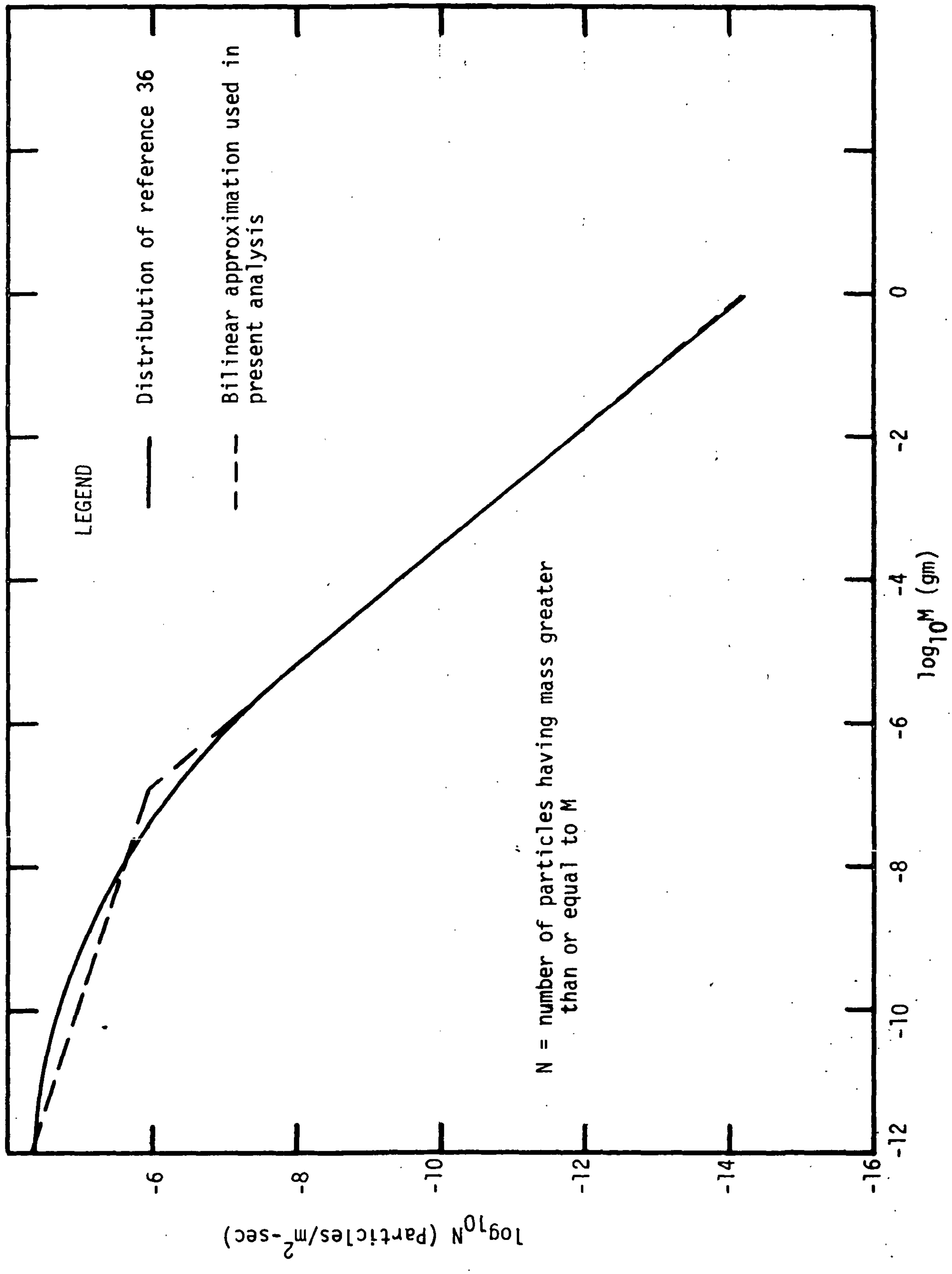

Figure 4.5 Cumulative Particle Flux in Near-Earth Environment

For the 90%, 99% and 99.9% probabilities of mission success, we put P(o) = 0.9, 0.99 and 0.999 respectively. From equation (4.8) we have

$$\log_{10}P(o) = -EN \log_{10}e$$

$$N = \frac{1}{E}\left(-\frac{\log_{10}P(o)}{\log_{10}e}\right) \tag{4.9}$$

But equation (4.6) may be written as

$$\log_{10}N = \begin{cases} -7.169 - 0.505 \log_{10}S, & S \leq 4.72 \times 10^{-3} \text{ cm} \\ -10.381 - 1.9 \log_{10}S, & S \geq 4.72 \times 10^{-3} \text{ cm} \end{cases} \tag{4.10}$$

Hence, combining equations (4.9) and (4.10) we have

$$-\log_{10}E + \log_{10}\left\{-\frac{\log_{10}P(o)}{\log_{10}e}\right\} = \begin{cases} -7.169 - 0.505 \log_{10}S, & S \leq 4.72\text{x}10^{-3} \text{ cm} \\ -10.381 - 1.9 \log_{10}S, & S \geq 4.72\text{x}10^{-3} \text{ cm} \end{cases} \tag{4.11}$$

The graphs generated with P(o) = 0.9, 0.99 and 0.999 are shown in figure 4.6 in log-log form.

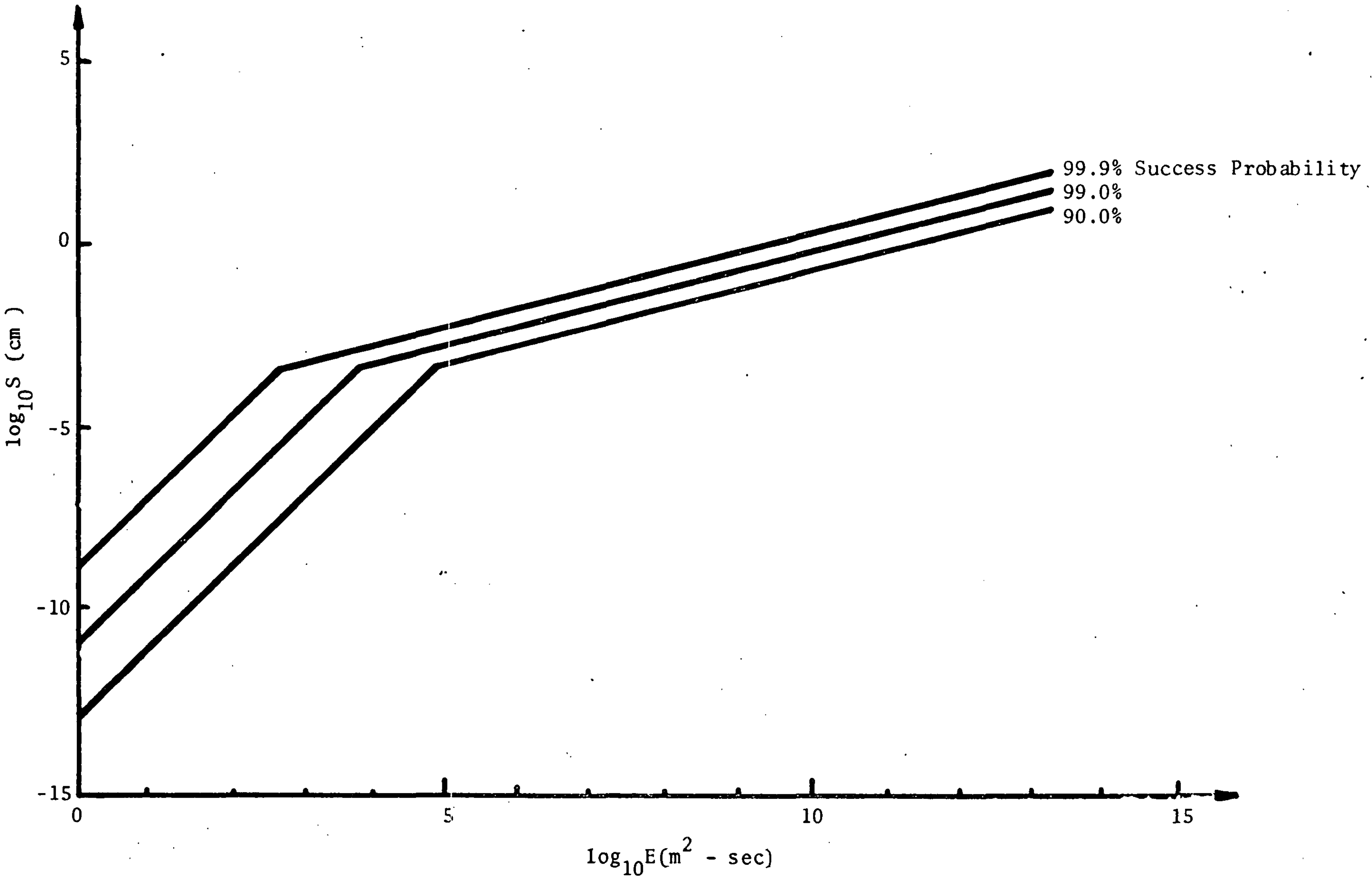

Figure 4.6 Required Spacing of Insulation Panel from Shield vs Mission Area Time Product for Three Success Probabilities.

5.0 DIRECT IMPACTS ONTO WATER FILLED TANKS

In the early phases of the experimental program, some firings were performed using an unprotected, water-filled tank. This phase of the program was subsequently deleted in order to provide more firings against protected tanks. The tank utilized was the same as that illustrated in figure 3.19 and used for the protected shots. The tank was instrumented with pressure gauges, and for one shot a pressure record was obtained 7.6 cm (3 in) from the point of impact. The probes were located as in figure 5.1 below.

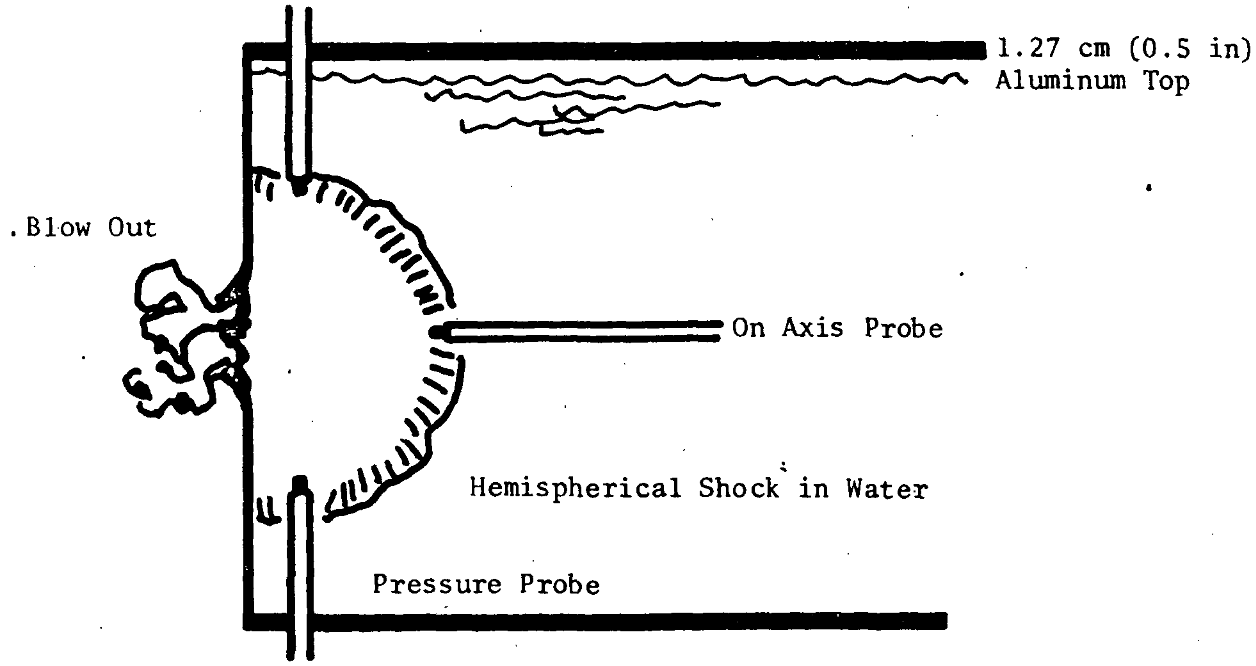

Figure 5.1 Arrangement of Pressure Probes Within Water Tank

It was assumed, in placing the probes in the indicated manner, that the blast due to impact of the projectile would be hemispherical in nature. Evidence to support this expectation was found in Stepka et al (reference 13). The subsequent similarity of the gauge records also verified the anticipated spherical symmetry of the shock wave. It was therefore decided to use an existing computer code to predict the pressure at the shock front on the basis of a spherically symmetric flow field and to compare the theoretical results with the experimental datum.

5.1 Analysis of Decaying Blast Wave

The flow behind the blast front is assumed to be governed by the equations reflecting conservation of mass, momentum and energy in an inviscid fluid. The Eulerian representation of these equations is:

$$\frac{\partial\rho}{\partial t} + u\frac{\partial\rho}{\partial r} + \rho\frac{\partial u}{\partial r} + j\frac{\rho u}{r} = 0 \qquad (5.1)$$

$$\frac{\partial u}{\partial t} + u\frac{\partial u}{\partial r} + \frac{1}{\rho}\frac{\partial p}{\partial r} = 0 \qquad (5.2)$$

$$\frac{\partial e}{\partial t} + u\frac{\partial e}{\partial r} + p\frac{\partial 1/\rho}{\partial t} + pu\frac{\partial 1/\rho}{\partial r} = 0 \qquad (5.3)$$

where $\rho = \rho(r,t)$ = density of the fluid

$u = u(r,t)$ = particle velocity

$p = p(r,t)$ = pressure

$e = e(r,t)$ = internal energy

r = radial position

t = time

and $$j = \begin{cases} 0 \text{ for planar symmetry} \\ 1 \text{ for cylindrical symmetry} \\ 2 \text{ for spherical symmetry} \end{cases}$$

We have the equation of state

$$e = e(p,\rho) \tag{5.4}$$

In the analysis of strong blast waves, one may assume self-similarity of the flow to obtain solutions which agree well with the early time response of the fluid (reference 18, 37, 38, 39). In the event that the shock wave decays in time, self-similarity is not observed. We attempt a "quasi-similarity" description due to Oshima (reference 40) and modified slightly by Rae (reference 12). The decaying blast wave has also been examined in references 41, 42, 43, and 44.

Let $R_s(t)$ be the position of the shock front at time t. $R_s(0) = 0$. Let $\xi = r/R_s$ be the usual similarity variable. We transform equations (5.1) to (5.4) from (r,t) space to (ξ,R_s) space and we introduce non-dimensional variables by:

$$u = \dot{R}_s\phi(\xi,R_s) \tag{5.5}$$

$$\rho = \rho_o\psi(\xi,R_s) \tag{5.6}$$

$$p = \rho_o\dot{R}_s^{\,2} f(\xi,R_s) \tag{5.7}$$

$$e - e_o = \dot{R}_s^{\,2} g(\xi,R_s) \tag{5.8}$$

Equations (5.1) - (5.3) become:

$$(\phi-\xi)\frac{\partial\psi}{\partial\xi} + \psi\frac{\partial\phi}{\partial\xi} + j\frac{\phi\psi}{\xi} = -R_s\frac{\partial\psi}{\partial R_s} \tag{5.9}$$

$$(\phi-\xi)\frac{\partial\phi}{\partial\xi} + \frac{R_s\ddot{R}_s}{\dot{R}_s^{\,2}}\phi + \frac{1}{\psi}\frac{\partial f}{\partial\xi} = -R_s\frac{\partial\phi}{\partial R_s} \tag{5.10}$$

$$(\phi-\xi)\frac{\partial g}{\partial\xi} + 2\frac{R_s\ddot{R}_s}{\dot{R}_s^{\,2}}g - \frac{f}{\psi^2}(\phi-\xi)\frac{\partial\psi}{\partial\xi} = \frac{f}{\psi^2}R_s\frac{\partial\psi}{\partial R_s} - R_s\frac{\partial g}{\partial R_s} \tag{5.11}$$

The boundary conditions at the shock front are the usual Rankine-Hugoniot relations. We write them in dimensional form as:

$$\rho_o \dot{R}_s = \rho_1(\dot{R}_s - u_1) \qquad (5.12)$$

$$p_o + \rho_o \dot{R}_s^{\,2} = p_1 + \rho_1(\dot{R}_s - u_1)^2 \qquad (5.13)$$

$$e - e_o = \frac{1}{2}(p_1 + p_o)\left(\frac{1}{\rho_o} - \frac{1}{\rho_1}\right) \qquad (5.14)$$

where the subscript o refers to conditions in the undisturbed medium and 1 refers to conditions directly behind the shock wave. In terms of the non-dimensional variable, equations (5.12) through (5.14) become

$$\psi_1(1 - \phi_1) = 1 \qquad (5.15)$$

$$f_1 = \frac{p_o}{\rho_o \dot{R}_s^{\,2}} + \phi_1 \qquad (5.16)$$

$$g_1 = \frac{1}{2}\left(f_1 + \frac{p_o}{\rho_o \dot{R}_s^{\,2}}\right)\left(1 - \frac{1}{\psi_1}\right) \qquad (5.17)$$

We now introduce the shock wave Mach Number

$$M_s = \dot{R}_s / c_o \qquad (5.18)$$

where c_o is the speed of sound in the undisturbed medium. We restrict the discussion, henceforth, to media which may be described by the ideal gas equation of state

$$e = \frac{p}{\rho}\,\frac{1}{\gamma - 1} \qquad (5.19)$$

It is recognized that water is well described by (5.19) with $\gamma = 7$ (reference 18). Thus we write

$$g = \frac{f}{\psi}\,\frac{1}{\gamma - 1} \qquad (5.20)$$

We note that $e_o^2 = \gamma p_o/\rho_o$ so that the term $p_o/(\rho_o \dot{R}_s^2)$ in equations (5.16), (5.17) may be written as:

$$\frac{p_o}{\rho_o \dot{R}_s^2} = \frac{1}{\gamma \dot{R}_s^2} c_o^2 = \frac{1}{\gamma M_s^2} \tag{5.21}$$

We now write the boundary conditions as:

$$\phi(1,M_s) = \frac{2}{\gamma+1}\left(\frac{M_s^2-1}{M_s^2}\right) \tag{5.22}$$

$$f(1,M_s) = \frac{2\gamma M_s^2-(\gamma-1)}{\gamma M_s^2(\gamma+1)} \tag{5.23}$$

$$\psi(1,M_s) = \frac{(\gamma+1)M_s^2}{(\gamma-1)M_s^2+2} \tag{5.24}$$

In order to solve equations (5.9) through (5.11) we transform them into a set of ordinary differential equations by means of the Oshima assumption:

"$\frac{1}{(f,\phi,\psi)} \frac{\partial}{\partial R_s}(f,\phi,\psi)$ is independent of ξ, $0 \leq \xi \leq 1$"

We note that

$$R_s \frac{\partial}{\partial R_s} = \frac{R_s \ddot{R}_s}{\dot{R}_s^2} M_s \frac{\partial}{\partial M_s} \tag{5.25}$$

and introduce the notation

$$\frac{R_s \ddot{R}_s}{\dot{R}_s^2} = \alpha \tag{5.26}$$

We refer to α as the "decay coefficient". Hence the derivatives in R_s may be evaluated at the boundary by means of equations (5.22) through (5.26). The values at interior points are determined by means of the Oshima assumption which simply requires that the derivative be proportional to the quantity itself. Now noting that equation (5.20) implies:

$$\frac{\partial g}{\partial \xi} = \frac{1}{\gamma-1}\left[\frac{\psi \frac{\partial f}{\partial \xi} - f \frac{\partial \psi}{\partial \xi}}{\psi^2}\right] \tag{5.27}$$

We have the governing equations for the fluid behind the shock front:

$$(\phi-\xi)\psi' + \psi\phi' = -\left[\frac{4\alpha\psi}{2+(\gamma-1)M_s^2} + j\frac{\psi\phi}{\xi}\right] = \beta_1 \tag{5.28}$$

$$(\phi-\xi)\phi' + f'/\psi = -\left[\frac{M_s^2+1}{M_s^2-1}\right]\alpha\phi = \beta_2 \tag{5.29}$$

$$\begin{aligned}(\phi-\xi)f' - (\phi-\xi)\frac{\gamma f}{\psi}\psi' &= -\left[2 + \frac{2(\gamma-1)}{2\gamma M_s^2-(\gamma-1)} - \frac{4\gamma}{2+(\gamma-1)M_s^2}\right]\alpha f \\ &= \beta_3(\phi-\xi)\end{aligned} \tag{5.30}$$

where the prime indicates differentiation with respect to ξ and we have introduced variables β_1, β_2, β_3. On solving equations (5.28) through (5.30) for the derivatives we have:

$$\psi' = \frac{(\phi-\xi)\beta 1 - \psi\beta 2 + \beta 3}{(\phi-\xi)^2 - \gamma f/\psi} \tag{5.31}$$

$$f' = \frac{\gamma f/\psi(\phi-\xi)\beta_1 - \gamma f\,\beta_2 + (\phi-\xi)^2\beta_3}{(\phi-\xi)^2 - \gamma f/\phi} \tag{5.32}$$

$$\phi' = \frac{-\frac{\gamma f}{\psi^3}\beta_1 + (\phi-\xi)\beta_2 - \frac{(\phi-\xi)}{\psi}\beta_3}{(\phi-\xi)^2 - \gamma f/\psi} \tag{5.33}$$

We now turn to the problem of evaluating the decay coefficient α. We use an iterative technique due to Rae (reference 12). The method of solution is as follows:

1) Choose a series of values of M_s

2) For each M_s calculate the boundary values at $\xi = 1$ from equations (5.22) to (5.24).

3) Assume a value of α and integrate numerically (using Runge-Kutta and/or a predictor corrector technique) equations (5.31) through (5.33) back to $\xi = 0$. If ϕ does not tend to zero at the origin, change α and repeat.

The solution is completed by determining the shock front trajectory. The energy integral is given by:

$$E_o = \int_o^{R_s} \rho\frac{u^2}{2} + \frac{p}{\gamma-1}\ k_j r^j dr - \int_o^{R_s} \frac{p_o}{(\gamma-1)} k_j r^j dr \qquad (5.34)$$

$$= k_j \rho_o \dot{R}_s^{\,2} R_s^{\,j+1} I - \frac{p_o}{(\gamma-1)} k_j \frac{R_s^{\,j+1}}{(j+1)} \qquad (5.35)$$

where

$$k = \begin{cases} 1 & \text{if } j = 0 \\ 2\pi & \text{if } j = 1 \\ 4\pi & \text{if } j = 2 \end{cases}$$

We introduce a characteristic length:

$$R_o^{\,j+1} = E_o/k_j p_o \qquad (5.36)$$

Then equation (5.35) may be written as:

$$\left(\frac{R_o}{R_s}\right)^{j+1} = \gamma M_s^{\,2} I^* - \frac{1}{(j+1)(\gamma-1)} \qquad (5.37)$$

where

$$I^* = \int_o^1 \left(\frac{\psi\phi^2}{2} + \frac{f}{\gamma-1}\right)\xi^j d\xi \qquad (5.38)$$

Thus the position of the shock front corresponding to a given Mach number may be established from equations (5.37) and (5.38). The corresponding time is given by:

$$\frac{c_o}{R_o} = \int_o^{R_s/R_o} \frac{d(R_s/R_o)}{M_s} \tag{5.39}$$

5.2 Comparison of Numerical and Experimental Results

Apart from a series of Mach Numbers, the computer program requires values of γ and j. As indicated in the previous section, water is well described by $\gamma = 7$. We set $j = 2$ to reflect spherical symmetry. The program then provides master curves in non-dimensional form. Reference to specific cases is then made by identification of values for ρ_o, c_o and E_o.

The value of ρ_o was taken from a handbook, while the ambient pressure is determined from

$$p_o = \frac{\rho_o c_o^2}{\gamma} \tag{5.40}$$

in which ρ_o, γ and c_o are presumed known. With $\gamma = 7$ we find $p_o = 3020$ kg/cm^2 (43,000 psi). Since the blast is produced by a projectile colliding with a thin wall we take the energy release E_o to be the kinetic energy of the projectile. Also, we assumed the blast to be confined to a half space by the inertia of the wall, we further multiply the kinetic energy by a factor of two. Hence

$$E_o = MV^2 \tag{5.41}$$

In figure 5.2 we present the non-dimensional trajectory of the blast wave. It is appropriate to the description of a spherical blast in any fluid medium characterized by ratio of specific heats $\gamma = 7$. In figure 5.3 we present graphs of non-dimensional static and stagnation pressures versus distance.

As we indicated in section 5.0, a pressure datum was obtained in one round. The impact involved a Lexan cylinder weighing 0.155 gm impacting at 8.25 km/sec (27,000 ft/sec). From equation (5.41) we find that

$$E_o = 1.19 \times 10^3 \text{ kg m}^2/\text{sec}^2$$

Hence it is found from equation 5.36 that

$$R_o = 1.42 \text{ cm } (0.56 \text{ in})$$

Then from figure 5.3 we find that the stagnation overpressure 7.6 cm (3 in) from the point of impact is given by

$$\frac{p_{TOT}}{p_o} - 1 = 0.273$$

Hence the theoretical peak pressure reading is 824 kg/cm^2 (11.7 kpsi) which is in good agreement with the experimentally determined maximum 774 kg/cm^2 (11.0 kpsi). In figure 5.4 we present some Beckman and Whitley photographs of the blast wave in a water filled tank due to impact by a Lexan projectile.

Because of the good agreement, further substantiation of the theoretical curve was desired. A body of data is available in reference 13.

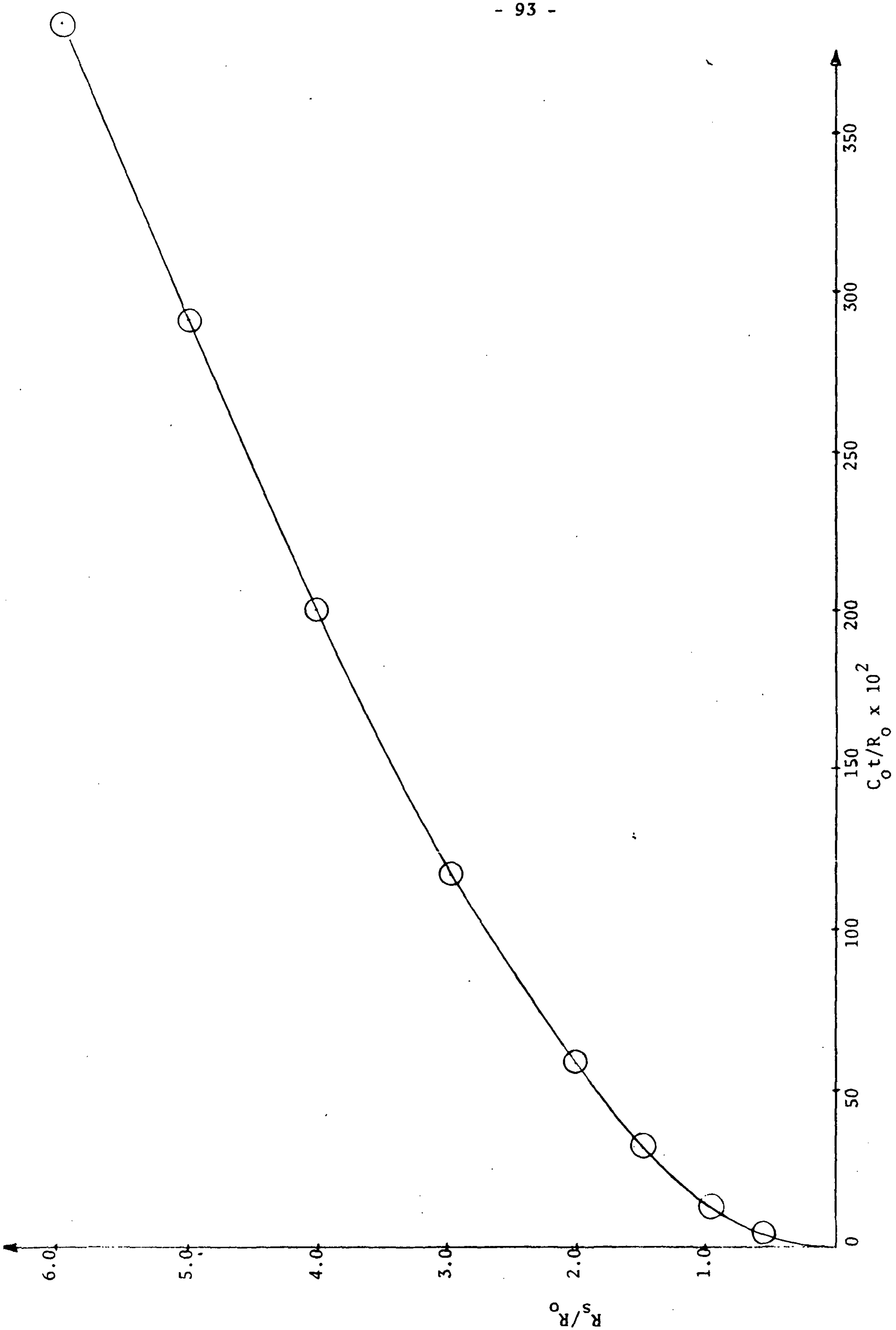

Figure 5.2 Non-dimensional trajectory of spherical blast wave in water.

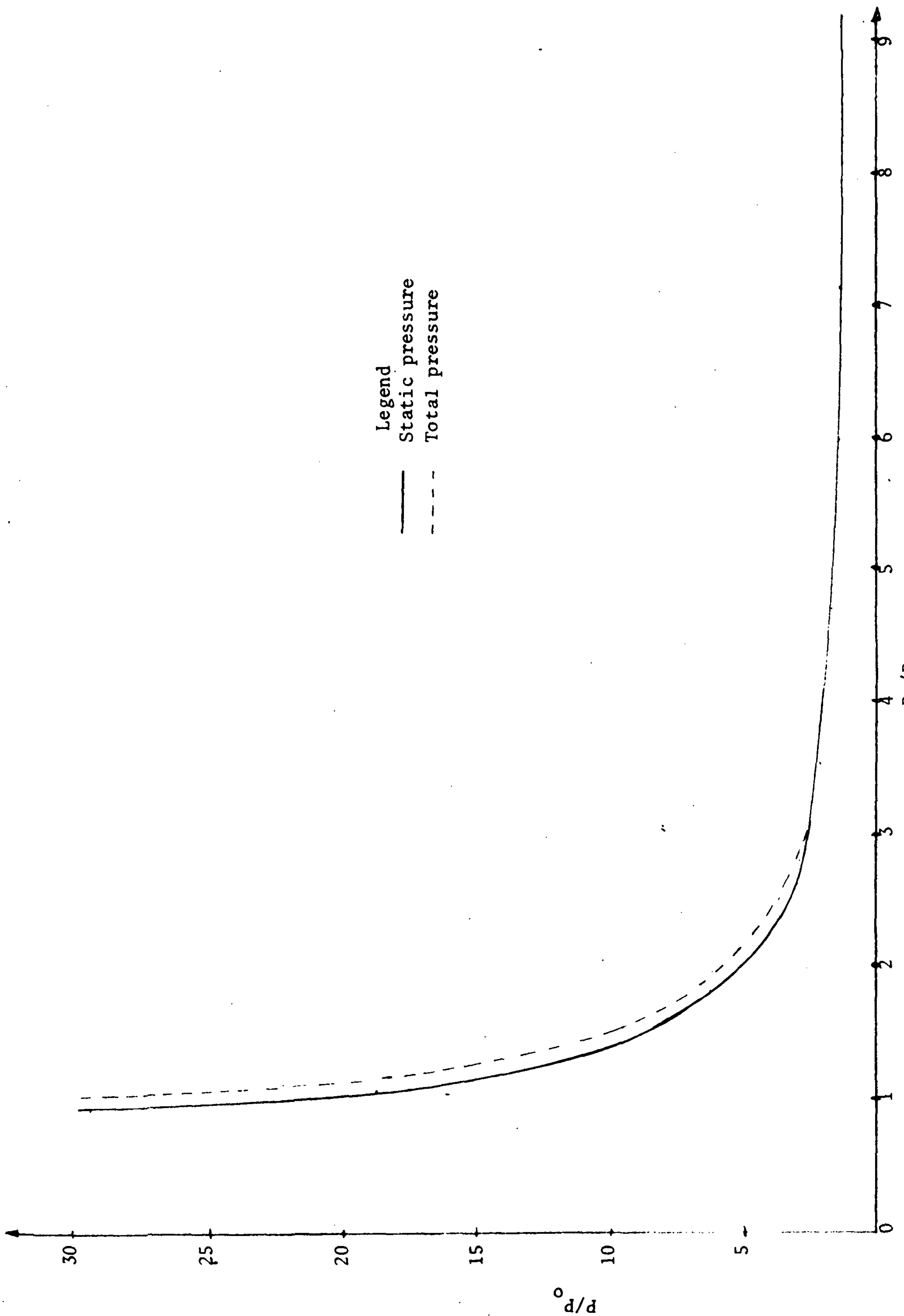

Figure 5.3 Pressure behind spherical blast wave in water versus non-dimensional distance from center.

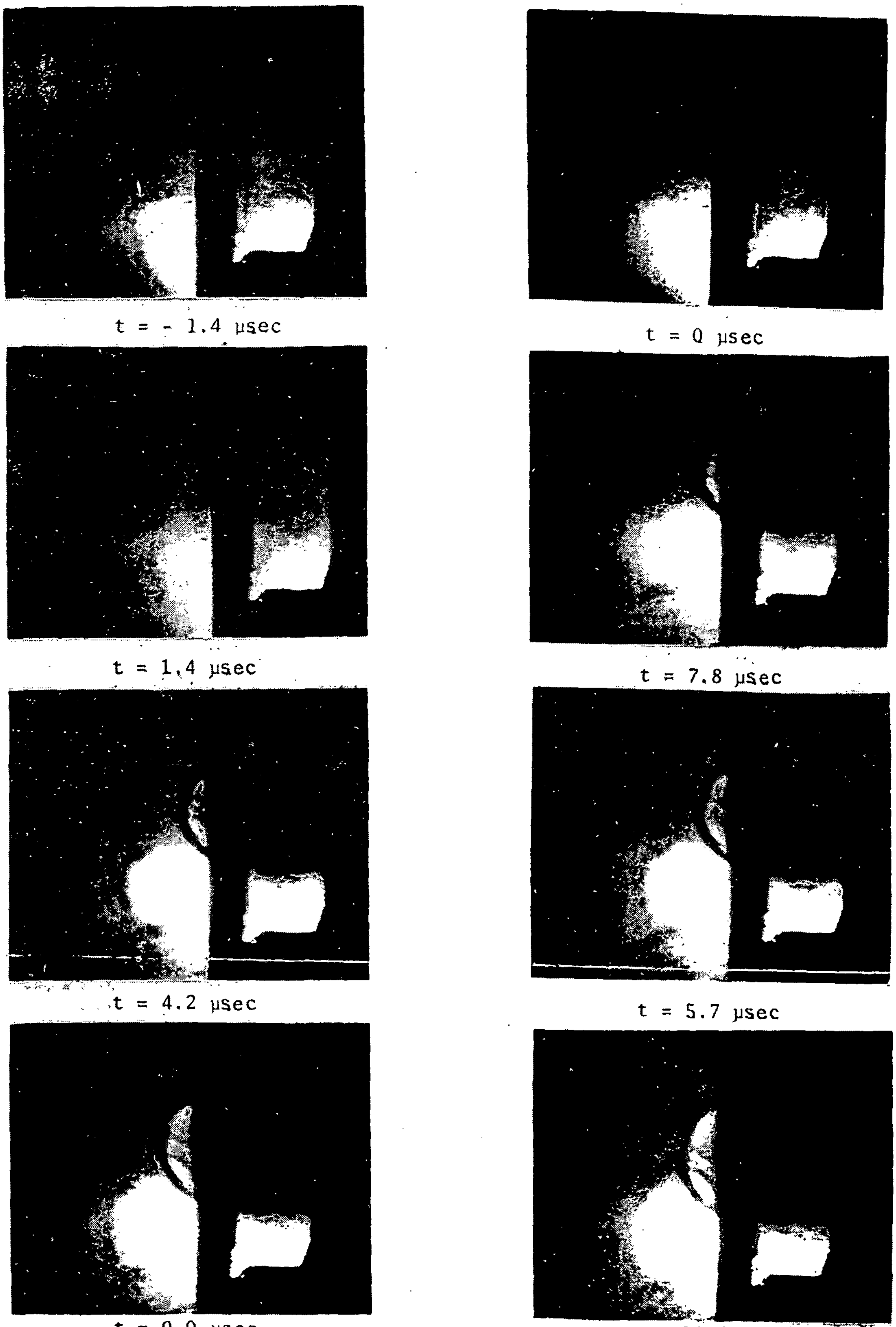

t = - 1.4 μsec

t = 0 μsec

t = 1.4 μsec

t = 7.8 μsec

t = 4.2 μsec

t = 5.7 μsec

t = 9.9 μsec

t = 11.4 μsec

Figure 5.4 Direct impact of 0.63 cm (0.25 in) dia by 0.76 cm (0.3 in) long Lexan projectile onto .159 cm (0.063 in) aluminum cover of water tank. Impact velocity was 8.5 km/sec (27,800 ft/sec). Photo coverage by Beckman and Whitley with framing rate 7.05 x 10^5 frames/sec. Times are referenced to impact

Figure 5.4 (Cont'd)

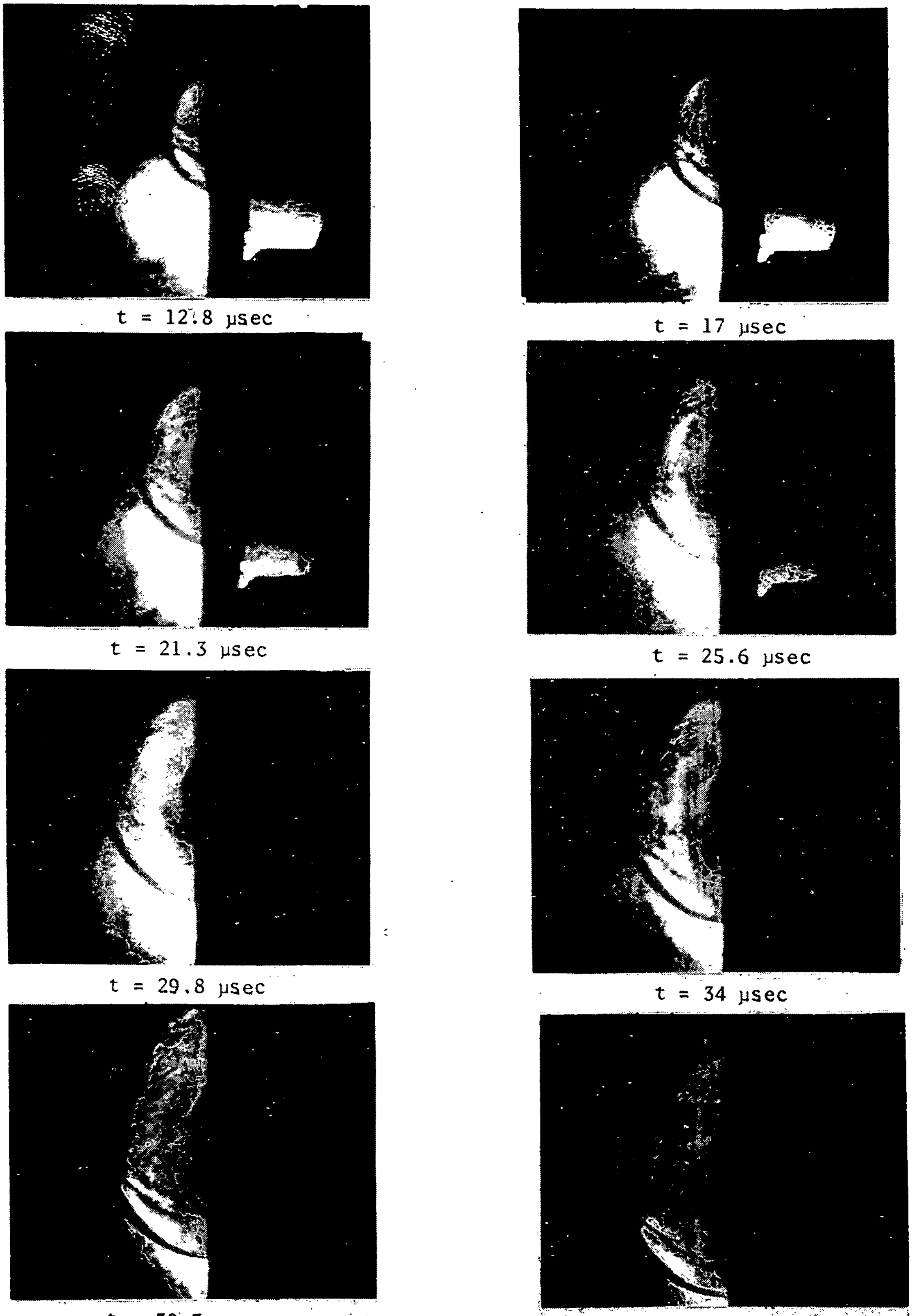

t = 12.8 μsec

t = 17 μsec

t = 21.3 μsec

t = 25.6 μsec

t = 29.8 μsec

t = 34 μsec

t = 38.3 μsec

t = 41.1 μsec

In figure 5.5 we have plotted the data of reference 13 against non-dimensional distance in order to effect a comparison with the theoretical curve (the solid curve). As may be seen, the theoretical curve is in good agreement with much of the data, especially at larger spacings. It is to be understood that the theory does not apply for values of R comparable to the dimensions of the projectile. Further sources of error may be found in a failure of the projectile to yield all its kinetic energy instantaneously (deceleration curves are plotted in reference 13) and premature blow out of the wall.

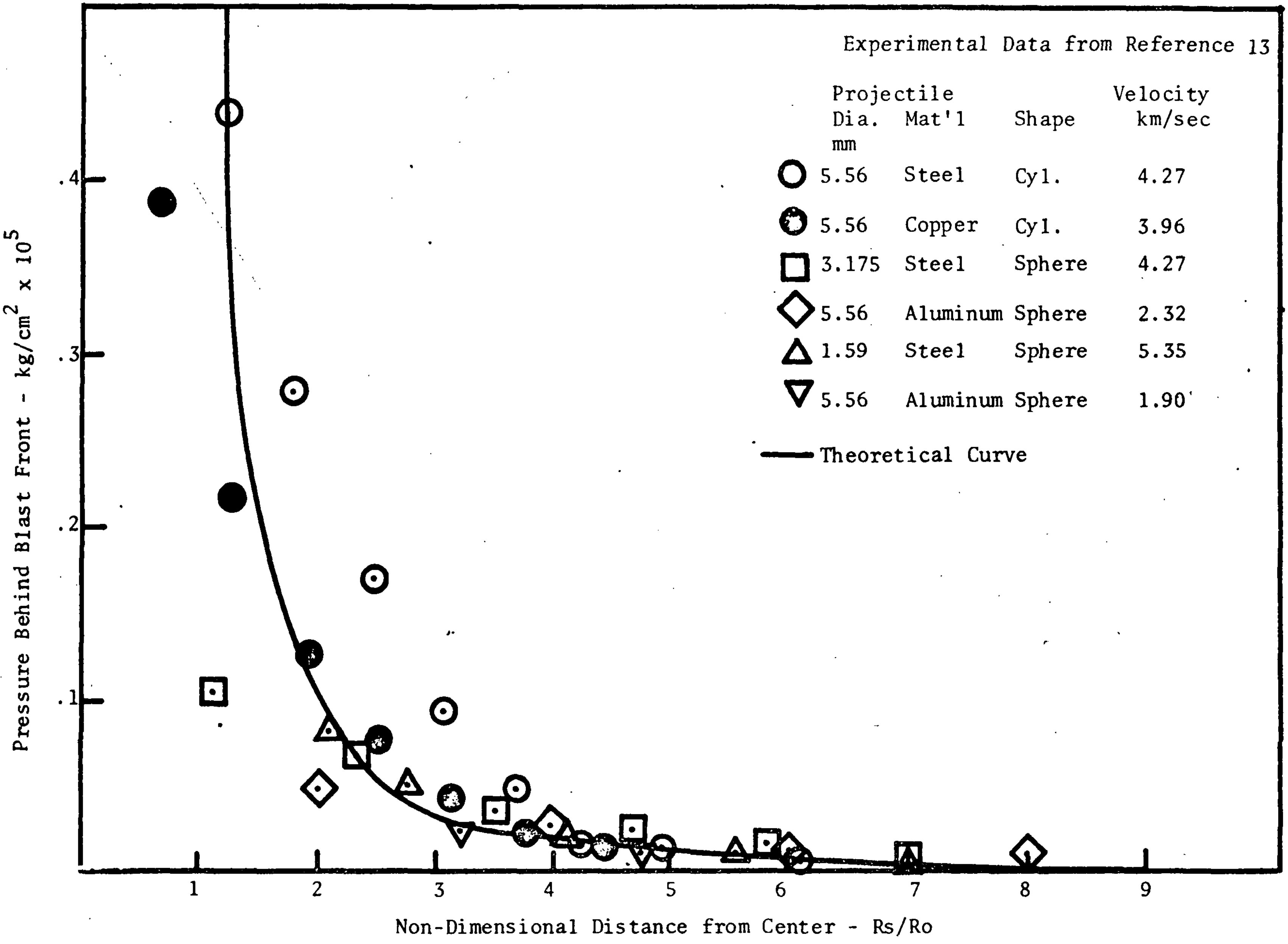

Figure 5.5 Comparison of Theoretical Pressure Behind Spherical Blast in Water With Data of Reference 13

6.0 EVALUATION OF IMPACT CHARACTERISTICS OF THE GRID-BUMPER

An area of concern in the application of solid shields to the protection of space vehicles against meteoroids has been the interference of the shield with the radiative environment. The Grid-Bumper, described in reference 3, was suggested as a possible solution. It is apparent that the presence of interstitial gaps in the Grid-Bumper will alleviate, to some extent, the interference of the shield with the radiation. It also seems reasonable to expect good protection against projectiles which are large compared to the apertures in the grid. Consequently, an experimental program has been conducted in order to gain further insight into the impact characteristics of a Grid-Bumper.

The evaluation of the Grid-Bumper has included two different, but related approaches. In the first approach, measurements of the debris cloud expansion velocities (radial & axial) and internal pressure distribution have been compared with results obtained using an equivalent weight per unit frontal area solid bumper. In addition, the relative protection afforded by the grid and solid shields have been compared by determining the ballistic limit thicknesses of 2024-T3 aluminum alloy witness sheets at two spacings (15.2 cm and 22.9 cm) downstream of the shield.

The bulk of the tests performed has involved Grid-Bumpers constructed of lead wire in such a manner as to have the same mass per unit frontal area as a solid lead shield 0.25 mm (0.010 in) in thickness. This standard Grid-Bumper consisted of two orthogonal layers of lead wire, 0.38 mm (0.015 in) in diameter, spaced 0.51 mm (0.020 in) apart. In figure 6.1 we present some photographs of the debris cloud due to the impact of a Lexan cylinder onto a Grid-Bumper. It will be observed that the debris cloud is quite different in appearance from that due to a solid shield (figure 3.20, for example). A number of firings was used to obtain a map of the dependence of the peak

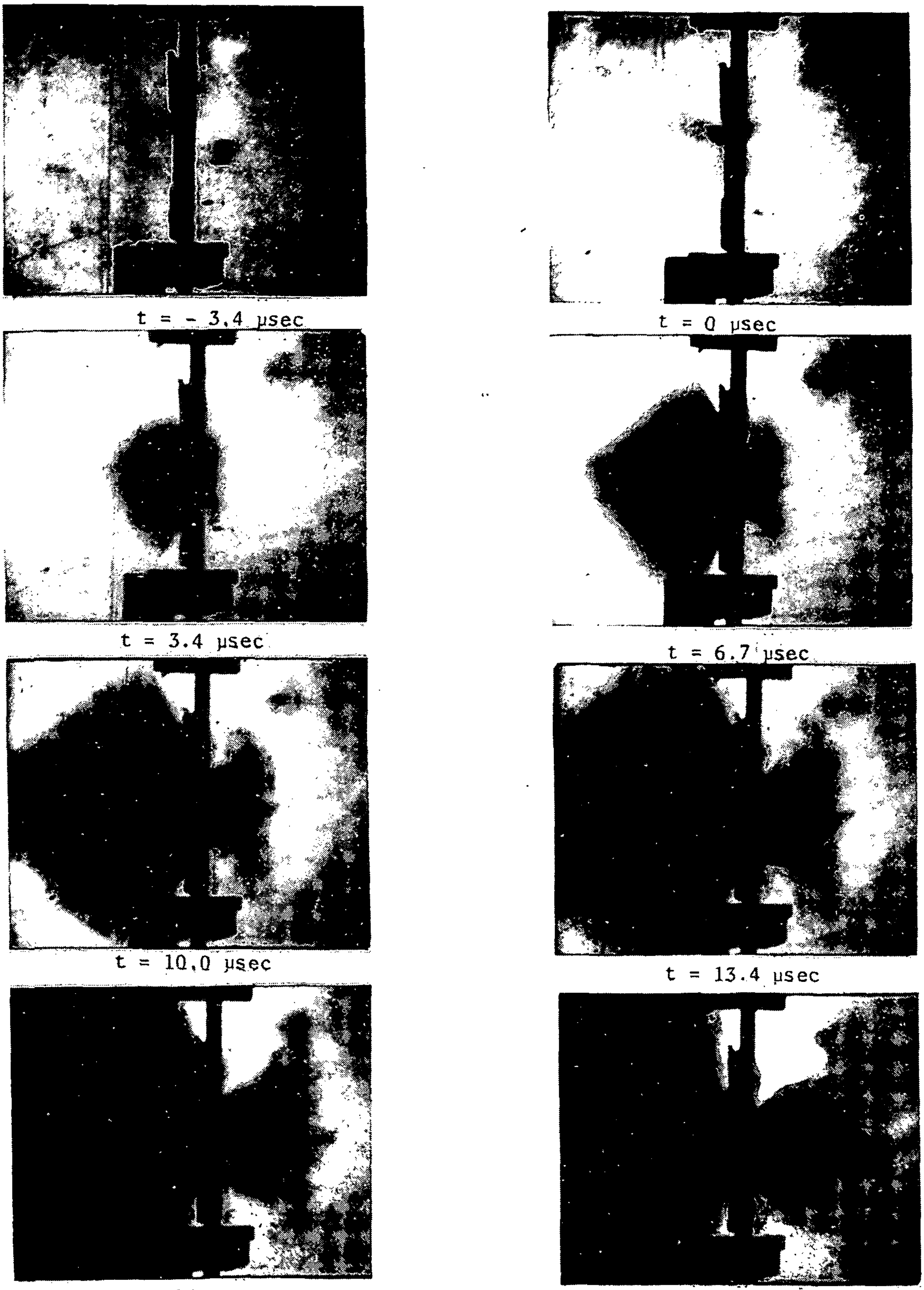

t = - 3.4 μsec

t = 0 μsec

t = 3.4 μsec

t = 6.7 μsec

t = 10.0 μsec

t = 13.4 μsec

t = 16.7 μsec

t = 20.0 μsec

Figure 6.1 Beckman and Whitley coverage of the impact of a 1.27 cm (0.5 in) diameter by 0.76 cm (0.3 in) long Lexan cylinder onto a lead wire grid at 9.45 km/sec (31,000 ft/sec). The grid is constructed of two orthogonal layers of wire 0.38 mm (0.015 in) in diameter, spaced 0.51 mm (0.020 in) apart

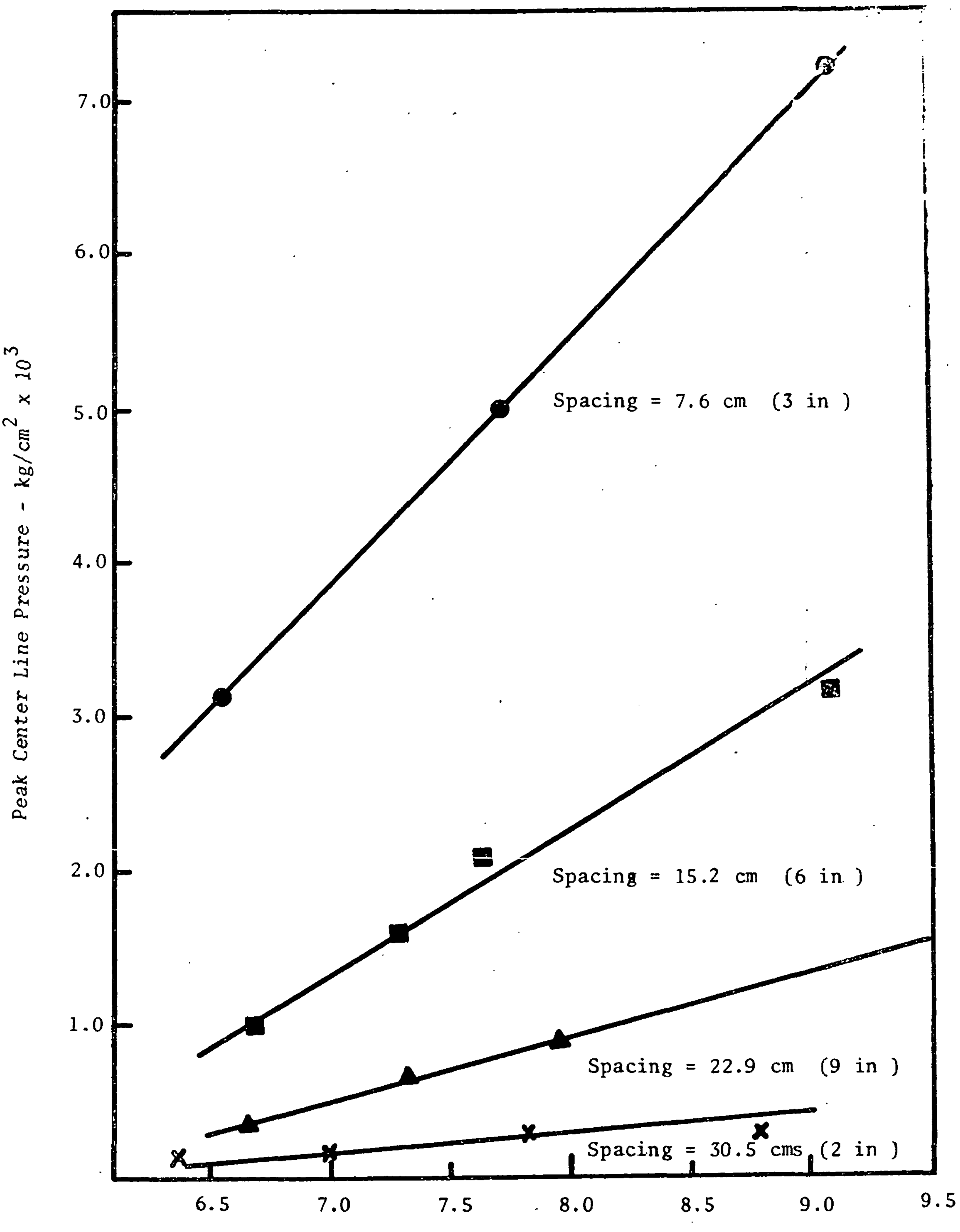

Figure 6.2 Peak center line pressure recorded on rigid witness plates loaded by debris from the impact of a 1.27 cm (0.5 in) diameter by 0.76 cm (0.3 in) onto a Grid-Bumper. The grid was constructed of two orthogonal layers of lead, 0.38 mm (0.015 in) diameter, spaced 0.51 mm (0.020 in) apart.

cloud pressure on impact velocity and distance downstream of the shield. The results are summarized in figure 6.2.

The first comparison between the grid and solid shields involved measurements of the rate of expansion of the debris cloud. Consider figure 6.3 in which the debris cloud is indicated at two points in time, T_1 and T_2.

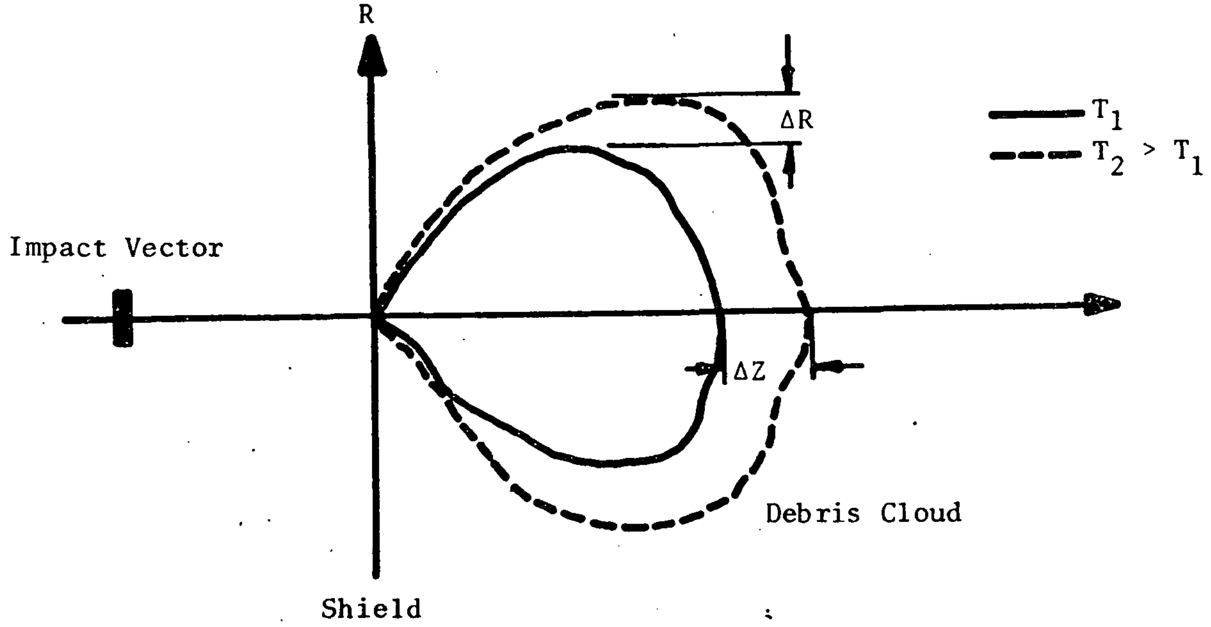

Figure 6.3 Sketch of Debris Cloud at Two Points in Time

We define

$$U_{esc,\,r} = \frac{\Delta R}{T_2 - T_1}$$

$$U_{esc,\,z} = \frac{\Delta Z}{T_2 - T_1}$$

From Beckman and Whitley photographic coverage of the impact event, it was possible to determine the radial and axial escape velocities of several debris clouds. In figure 6.4 we have indicated the ratio of Uesc, z to impact velocity, V, versus impact velocity. The full line indicates measurements made on debris clouds formed by impacts of 1.27 cm (0.5 in) diameter by 0.76 cm (0.3 in) long Lexan pellets onto Grid-Bumpers and the dashed line which represents impacts on the equivalent weight solid shield (0.25 mm thickness) is taken from reference 2. It may be seen that the value of Uesc, z/V is in all cases substantially higher for the grid than for the solid shield. It also appears that the value of Uesc, z/V is tending towards a limiting value of 1.75 for the grid as compared with a uniform value of 1.4 for the solid shield.

In figure 6.5 a comparison is made between the lateral expansion rate of the debris cloud for shots at approximately the same velocity onto grid and equivalent weight solid shields. It is clear that the escape velocities are very close for the two cases.

The second comparison made between the grid and solid shields involved the pressure distribution internal to the cloud. Figure 6.6 indicates the peak pressures determined from a number of impacts of 1.27 cm (0.5 in) diameter by 0.76 cm (0.3 in) long Lexan pellets onto 0.25 mm (0.010 in) lead shields and equivalent weight Grid-Bumpers at 7.6 km/sec (25,000 ft/sec). The indication is that at the close spacings (∿15 cm) pressures are generally lower in the grid generated cloud than in the cloud produced by the solid shield. At larger spacings (∿22 cm), however, the pressures are fairly close although the grid appears to be somewhat higher. In all cases, the pressure was measured by probes flush-mounted in a rigid witness sheet. Hence, figure 6.6 is a representation of the peak total pressure in the clouds at various radial and axial spacings.

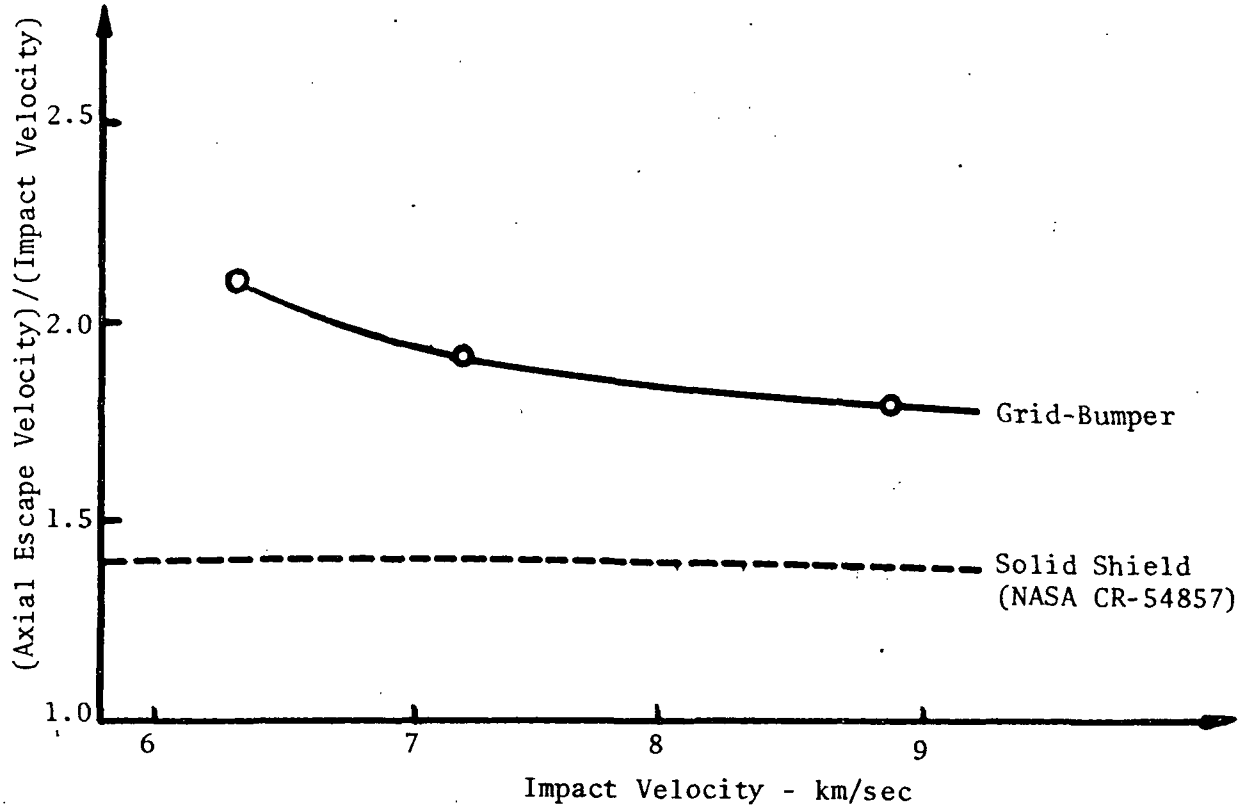

Figure 6.4 Ratio of Axial Escape Velocity to Impact Velocity vs Impact Velocity

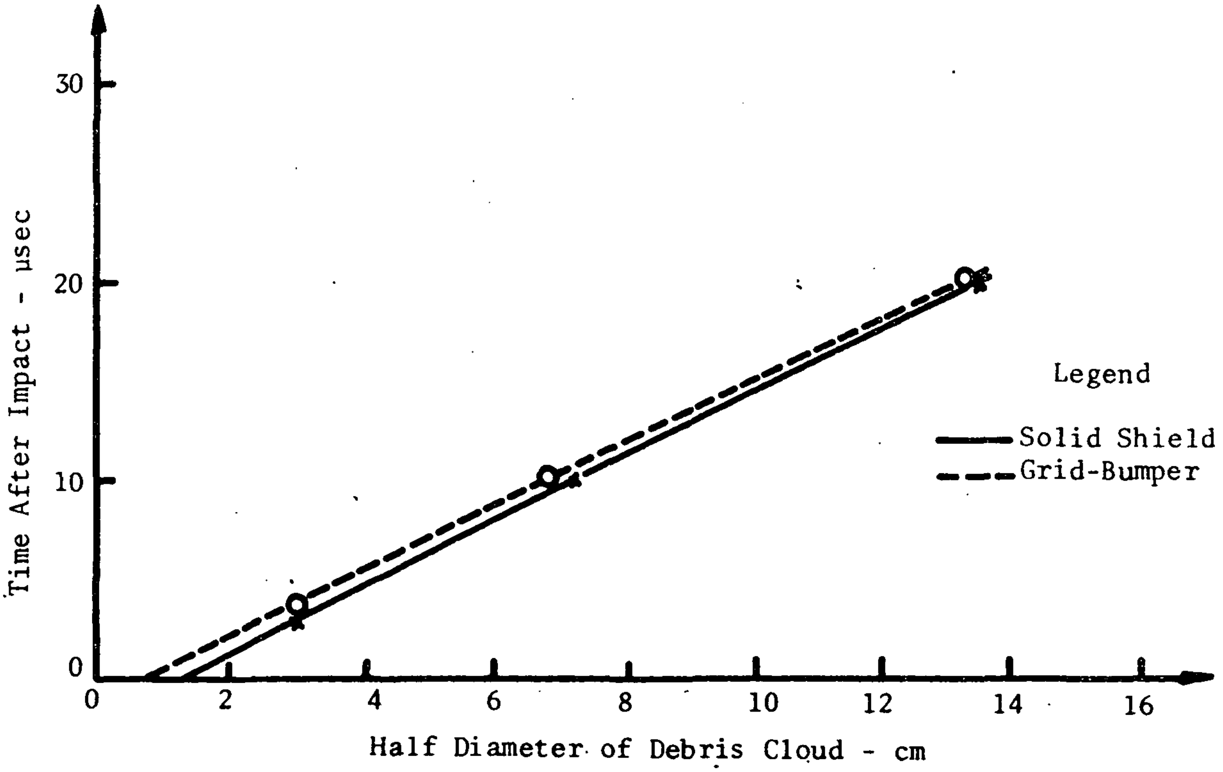

Figure 6.5 Radial expansion of debris clouds produced by impacts of 1.27 cm (0.5 in) diameter by 0.76 cm (0.3 in) long Lexan cylinders onto 0.25 mm (0.010 in) thick solid lead shield and equivalent weight Grid-Bumper at 8.7 km/sec (28,500 ft/sec).

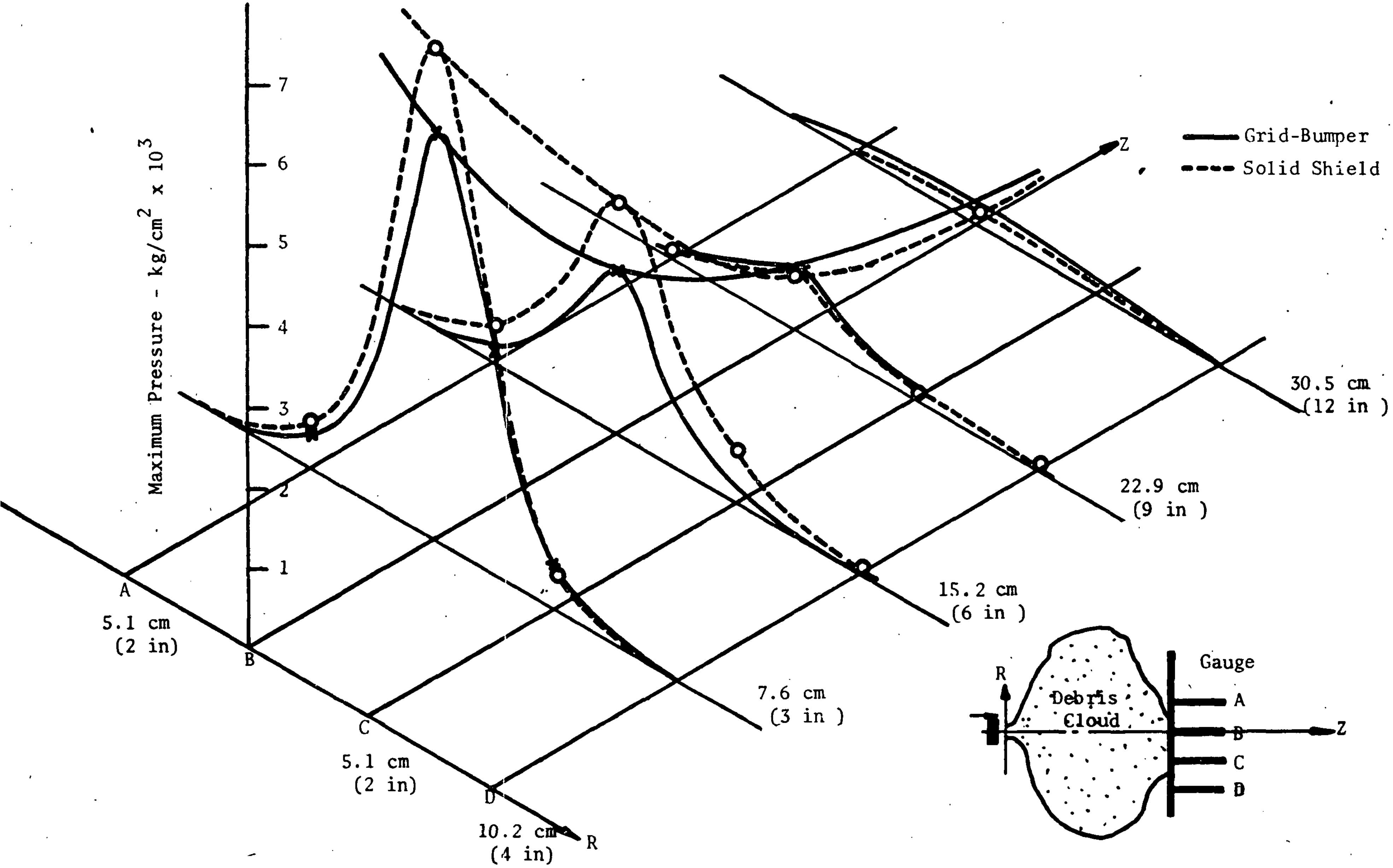

Figure 6.6 Comparison of peak total pressure in debris clouds produced by the impact of 1.27 cm (0.5 in) diameter by 0.76 cm (0.3 in) long Lexan cylinders onto 0.25 mm (0.010 in) lead shields and equivalent weight Grid-Bumpers, at 7.6 km/sec (25,000 ft/sec).

It is interesting to compare the peak pressure data of figure 6.6 with some ballistic limit results.

TABLE 6.1

Comparison of Ballistic Limit Thickness of 2024-T3 Aluminum Witness Plate When Protected by 0.25 mm (0.010 in) Solid Lead and Equivalent Weight Grid-Bumper. Projectile is 1.27 cm (0.5 in) Diameter by 0.76 cm (0.3 in) Long Lexan Cylinder Impacting at 7.6 km/sec (25,000 ft/sec).

Spacing		Ballistic Limit Thickness	
cm	in	Grid-Bumper	Solid Shield
15.2	6.0	$0.190 \text{ cm} < h_{BL} < 0.195 \text{ cm}$ (0.049 in) (0.050 in)	$0.185 \text{ cm} < h_{BL} < 0.195 \text{ cm}$ (0.047 in) (0.050 in)
22.9	9.0	$0.125 \text{ cm} < h_{BL} < 0.160 \text{ cm}$ (0.032 in) (0.040 in)	$0.102 \text{ cm} < h_{BL} < 0.125 \text{ cm}$ (0.026 in) (0.032 in)

From this limited amount of data, it appears that there is no significant difference in protection at 15.2 cm whereas at 22.9 cm, the solid shield seems slightly superior to the Grid-Bumper. This apparent gain in protection with the solid shield at larger spacings is qualitatively in agreement with the peak pressure data of figure 6.6.

One should not, however, expect a good correlation between the dependence on spacing of peak pressure and ballistic limit as the center line pulses are quite different for the two types of shields. One expects to find a better correlation between the total center line impulse (i.e. the integral of the center line pressure pulse with respect to time) and the ballistic limit of the witness sheet. If one is considering the hazard associated with clouds having similar pulse shares in time, then the peak total pressure becomes a suitable quantity to correlate with damage. This, however, is not the case when dealing with clouds as dissimilar as those produced by impacts onto Grid-Bumpers and solid shields.

In figure 6.7 we have indicated the center line pressure pulses associated with the impacts of a 1.27 cm (0.5 in) diameter by 0.76 cm (0.3 in) long Lexan cylinder at 7.6 km/sec (25,000 ft/sec) onto a 0.25 mm (0.010 in) thick solid lead shield and an equivalent weight Grid-Bumper. It must be noted that two peaks are present for each curve. The presence of the second peak in the solid shield pressure distribution has been previously explained as particulate debris.

This explanation does not appear satisfactory for the Grid-Bumper pressure distribution. If, in fact, the second (i.e. the larger peak occurring at ∿ 11 μsec) is due to particulate debris, we should expect it to travel more slowly than the gaseous pulse associated with the solid shield. It is found for impacts onto solid lead shields that the peak of the gaseous pressure travels at approximately the impact velocity while the peak of the particulate debris pressure pulse travels at roughly one half the impact velocity. From figure 6.7 we see that the time for the leading edge of the debris cloud produced by an impact at 7.6 km/sec (25,000 ft/sec) onto a Grid-Bumper to reach a probe spaced 15.2 cm (6.0 in) downstream is given by

$$T_1 = \frac{15.2 \times 10^{-5}}{1.9 \times 7.6} = 10.5 \ \mu\text{sec}$$

Again from figure 6.2 we see that the time required for the leading edge of the debris cloud produced by the impact onto the solid shield to reach a probe spaced 15.2 cm (6.0 in) downstream of the shield is given by

$$T_2 = \frac{15.2 \times 10^{-5}}{1.3 \times 7.6} = 15.4 \ \mu\text{sec}$$

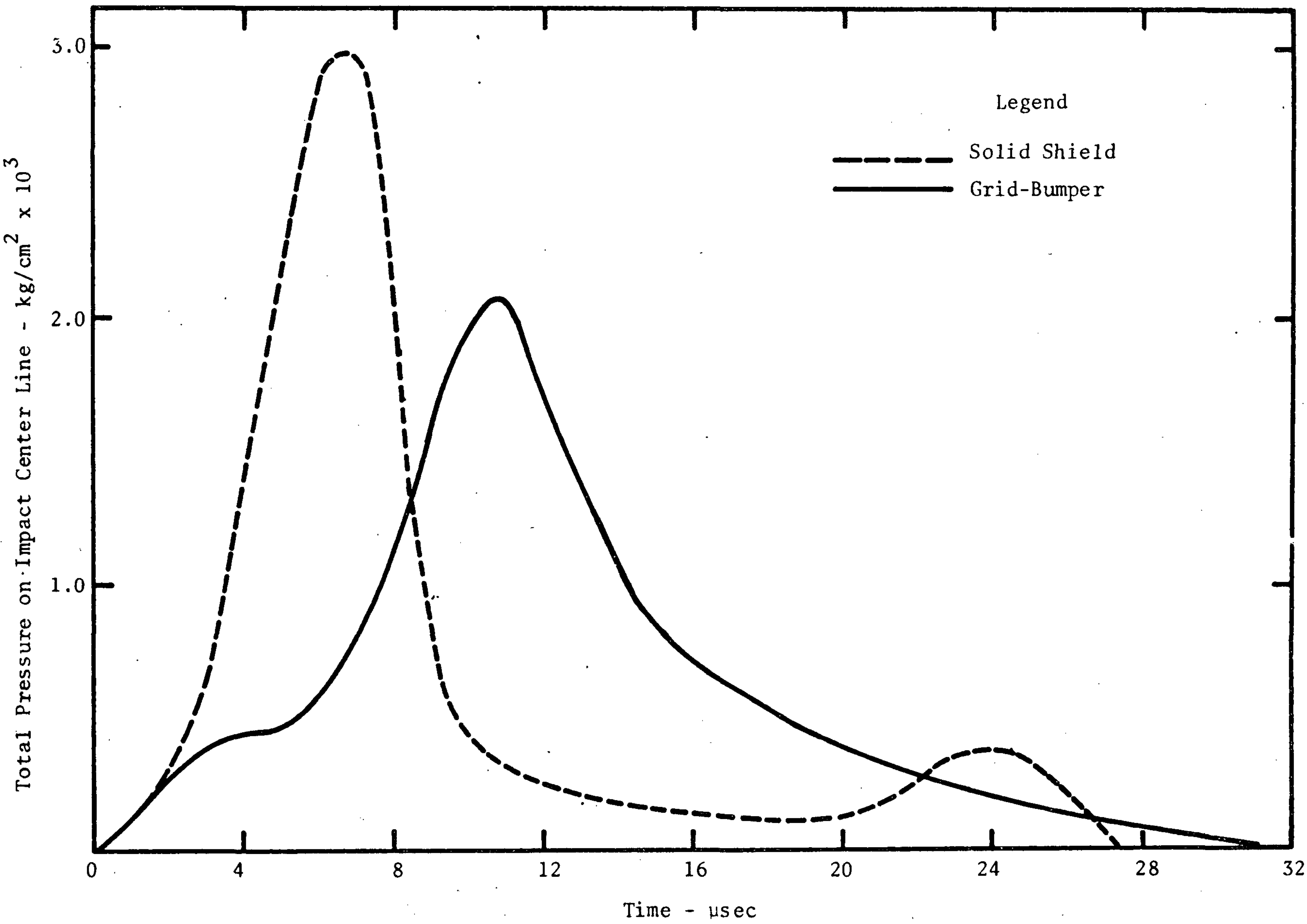

Figure 6.7 Total pressure on center line vs time for impacts of 1.27 cm (0.5 in) diameter by 0.76 cm (0.3 in) long Lexan cylinders onto 0.25 mm (0.010 in) solid lead shield, and equivalent weight Grid-Bumper at 7.6 km/sec (25,000 ft/sec). Gauge flush-mounted in rigid main wall spaced 15.2 cms (6 in) downstream of shield.

Now the primary peak of the solid profile of figure 6.7 occurs at a time 6.8 μsec after the leading edge of the cloud reaches the probe, i.e. at a time equal to 15.4 + 6.8 = 22.2 μsec after impact. Thus the velocity associated with the gaseous pulse is given by 15.2 cm/27.2 μsec = 6.9 km/sec (22,600 ft/sec), or slightly less than impact velocity. A similar calculation applied to the secondary pulse of the Grid-Bumper pressure profile indicates that the velocity associated with the peak is given by 15.2/(10.5 + 11) cm/μsec = 7.1 km/sec (23,300 ft/sec). The closeness of the two velocities suggests that the secondary pulse of the Grid-Bumper pressure profile is associated with a gaseous phenomenon. Further, the primary pulse in the Grid-Bumper profile is travelling faster than the secondary pulse so that it seems reasonable to associate it with gaseous debris.

In figure 6.8 we have indicated the center line pressure profiles for impacts onto Grid-Bumpers at similar velocities and for center line pressure probes located 15.2 and 30.6 cm (6.0 and 12.0 in) downstream of the shield. At the impact velocities involved (9.2 km/sec (30,200 ft/sec) at 15.2 cm (6.0 in) and 8.76 km/sec (28,800 ft/sec) for the 30.6 cm (12.0 in) case respectively), the equivalent weight per unit area solid shield would have totally vaporized the projectile so that only one pressure pulse, the gaseous pulse, would have appeared.

It is clear, however, in figure 6.8 that two peaks are present. In the case of the 15.2 cm (6.0 in) spacing, the primary pulse is partially merged in the secondary pulse. At 30.6 cm (12.0 in), the pulses are separate and distinct.

We summarize the comparative study of the solid shield and the equivalent weight per unit area Grid-Bumper as follows:

1. At a given impact velocity, the debris cloud associated with

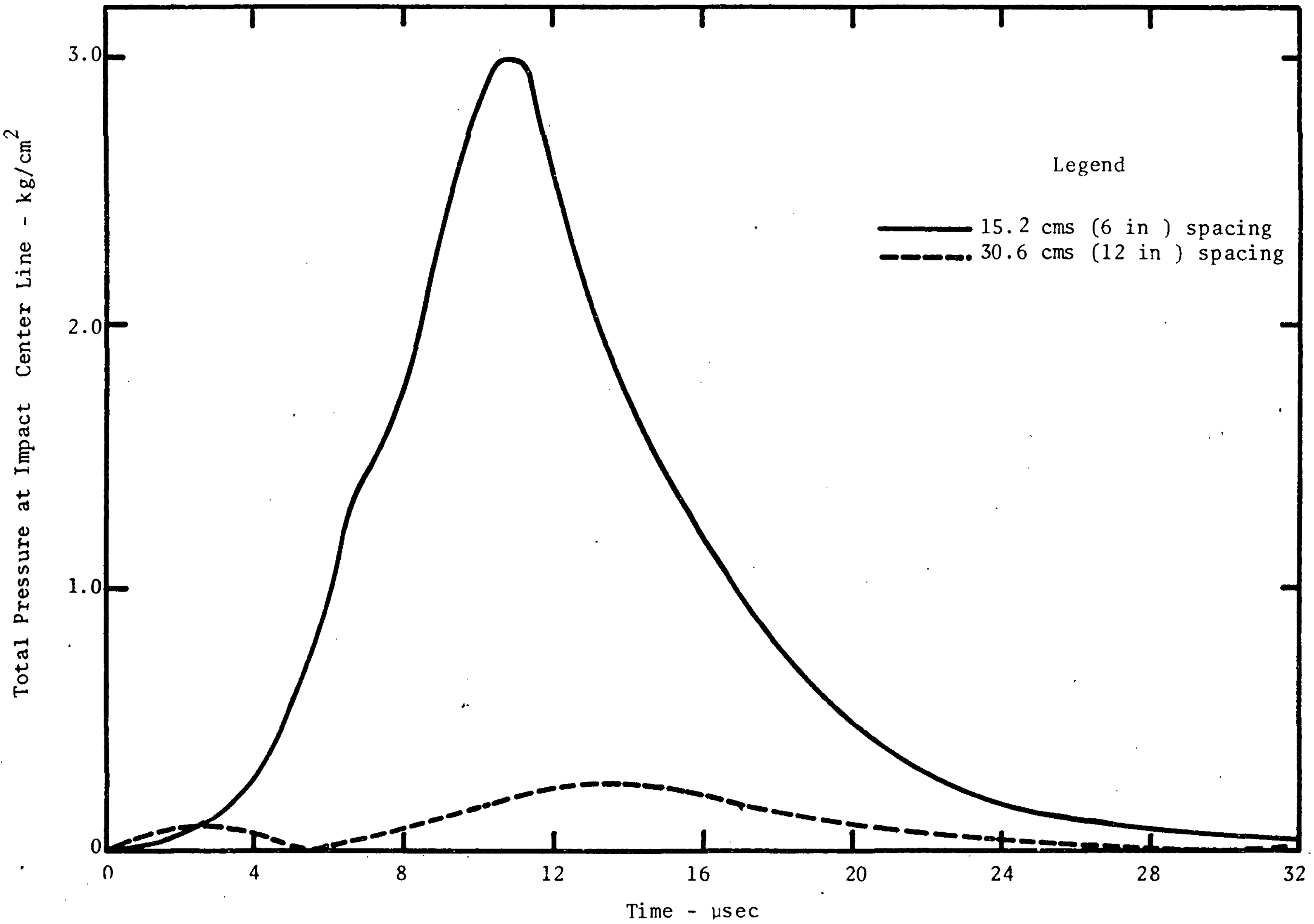

Figure 6.8 Total pressure on center line vs time for impacts of 1.27 cm (0.5 in) diameter by 0.76 cm (0.3 in) long Lexan cylinders onto Grid-Bumpers. The 15.3 cms spacing measurement corresponds to velocity of 9.2 km/sec (30,200 ft/sec) and 30.6 cm spacing to an impact velocity of 8.8 km/sec (28,800 ft/sec). Grid has weight-per-unit area equal to that of 0.25 mm (0.010 in) solid shield and is made of 0.38 mm (0.015 in) diameter lead wires spaced 0.51 mm (0.020 in) apart.

the Grid-Bumper is characterized by an axial escape velocity substantially in excess of that associated with the solid shield while the radial expansion rates are quite close for the two.

2. At close spacings, the peak total pressure in the Grid-Bumper debris cloud is lower than in the solid shield debris cloud while at larger spacings, the reverse is true.
3. No appreciable difference in protection is observed at close spacings while at larger spacings, the Grid-Bumper appears to be slightly less effective than the solid shield.
4. Two peaks are observed in the center line pressure profile associated with the Grid-Bumper debris cloud. The peaks resolve themselves at a spacing of about 30 cm (12 in). Both peaks appear to be associated with gaseous debris.

The second approach has been devoted to an investigation of the very early time impact characteristics of the grid in order to obtain an explanation of differences observed in the comparative study of the first approach. It is suggested that an interaction of material jetting through the interstitial gaps in the grid might be responsible for the very high axial velocity. It is in any case clear that a directed, non-isotropic phenomenon is occurring as the high axial velocities (relative to the solid shield) are not accompanied by similarly high radial velocities. Further, the presence of two separate peaks indicates that the first peak might be identified with jetted material while the second peak would correspond to normal expansion of shocked material.

The impact model, tentatively suggested is indicated in figure 6.9(a) through (d). For simplicity, the projectile is depicted as impacting an array of parallel wires, rather than a Grid. The extension of the model to the case of a Grid can then be performed later. In figure 6.9(a) we see the configuration at the instant of contact. The wires are considered to be normal to the page. Shortly after impact, an array of cylindrical waves is observed in the projectile (figure 6.9(b)). These waves will expand and interact with the free surfaces between the wires. The highly compressed plasma will then escape around the wires in the form of a cylindrical jet. Note that in figures 6.9(a) to 6.9(d), the shocked material is represented by darkened areas. The jet formed in this way when a cylindrical or spherical surface impacts on a plane is well known (references 45, 46, 47,). At a still later time, we expect adjacent pairs of jets to interact and, by symmetry, combine to an axially directed jet (figure 6.9(c)). It is the combined, axially directed jet which

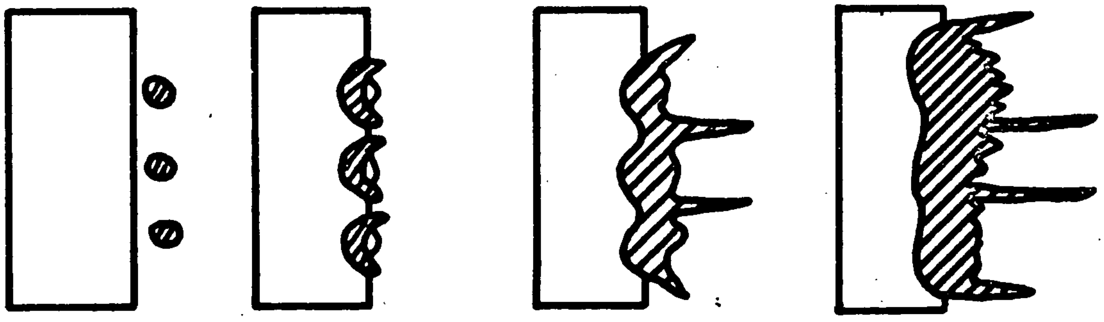

Figure 6.9 Schematic of Impact Onto Parallel Wires at Impact and Several Times Shortly Thereafter

is responsible for the high axial escape velocity. This effect is analogous to the Munroe effect well known in explosives (reference 48).

In the meantime, we expect the expanding cylindrical waves in the target to interact and to form an essentially planar wave (figure 6.9(d)). It now becomes possible to visualize the debris cloud formed by the impact onto a Grid-Bumper as consisting of material processed in two different manners. The front part of the cloud would consist of material involved in the jet interaction, possibly travelling at higher velocities than these obtained with a solid shield. The latter portion of the cloud would resemble a solid shield debris cloud, having been processed by an essentially planar wave.

In order to evaluate this model of the Grid-Bumper, we performed a series of firings in which 1.27 cm (0.5 in) diameter by 0.75 cm (0.3 in) long Lexan cylinders were impacted onto single and double strands of 0.32 cm (0.125 in) diameter lead wire. The experimental configuration is shown in figure 6.10.

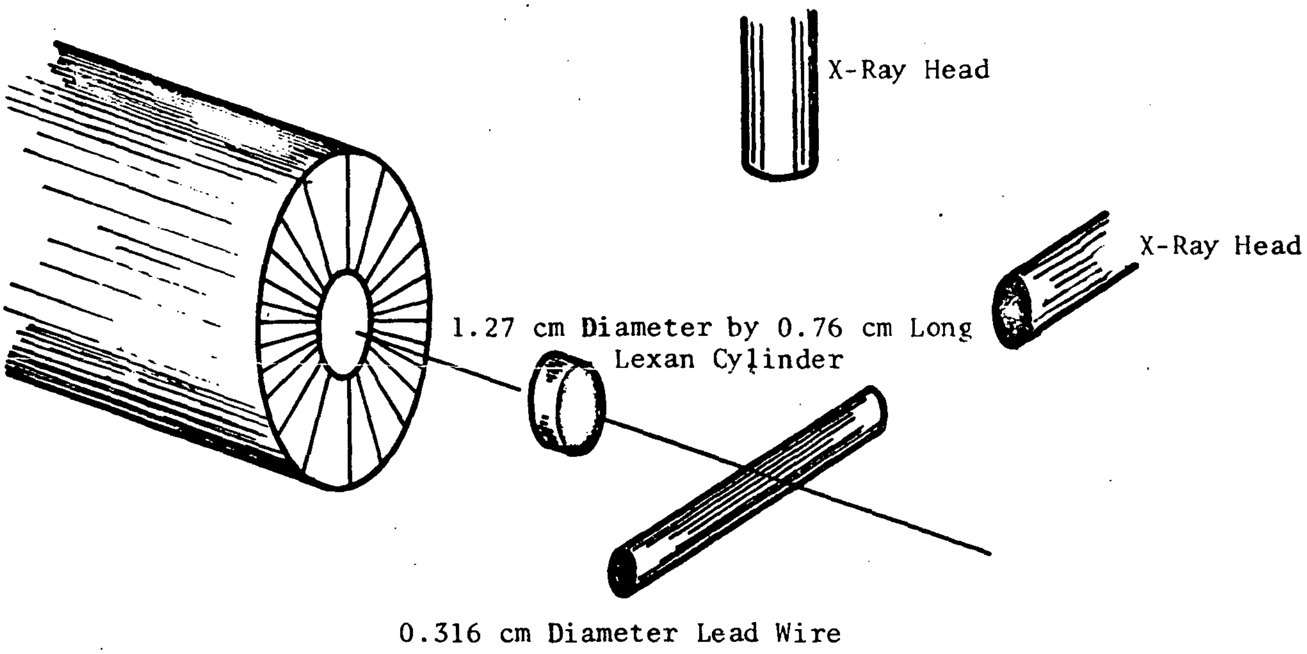

Figure 6.10 Schematic of Experimental Configuration

The target wire (or wires) was located quite close to the muzzle to assure accurate alignment. Since the x-ray heads were used to obtain radiograms of the shocked debris, it was not possible to obtain confirmation of the velocity. Gun parameters suitable to the desired velocity were chosen and this velocity was assumed to have been realized. In practice, it must be understood that the velocity is observed to scatter by ± 0.3 km/sec (1,000 ft/sec) about the nominal velocity.

In figure 6.11 we show radiograms taken just after the impact of a Lexan cylinder onto a single lead strand. Figure 6.11(a) is a view along the axis of the wire while figure 6.11(b) is a view normal to the plane containing the wire and projectile flight axis.

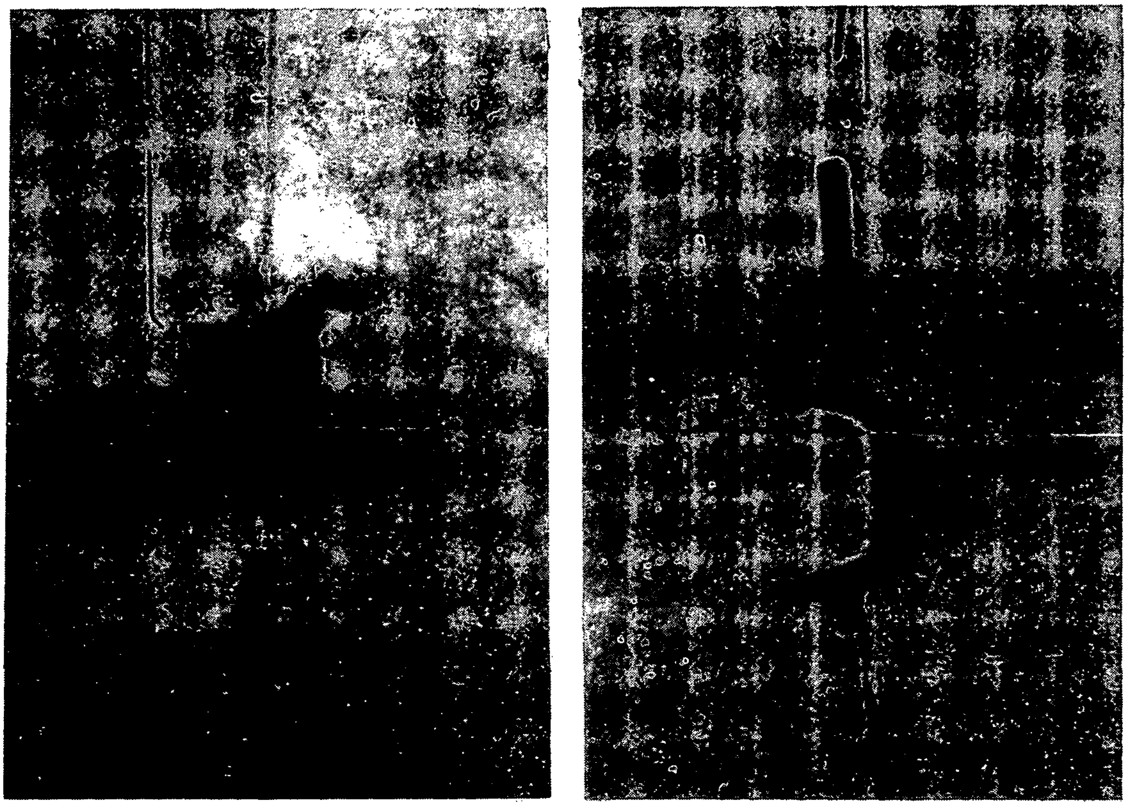

(a) (b)

Figure 6.11 Radiograms of the Impact of a Lexan Cylinder onto a Lead Wire at Approximately 7.0 km/sec (23,000 ft/sec).

The impact velocity is approximately 7.0 km/sec (23,000 ft/sec). From the two orthogonal views of the event, one may construct a sketch of the debris cloud (figure 6.12).

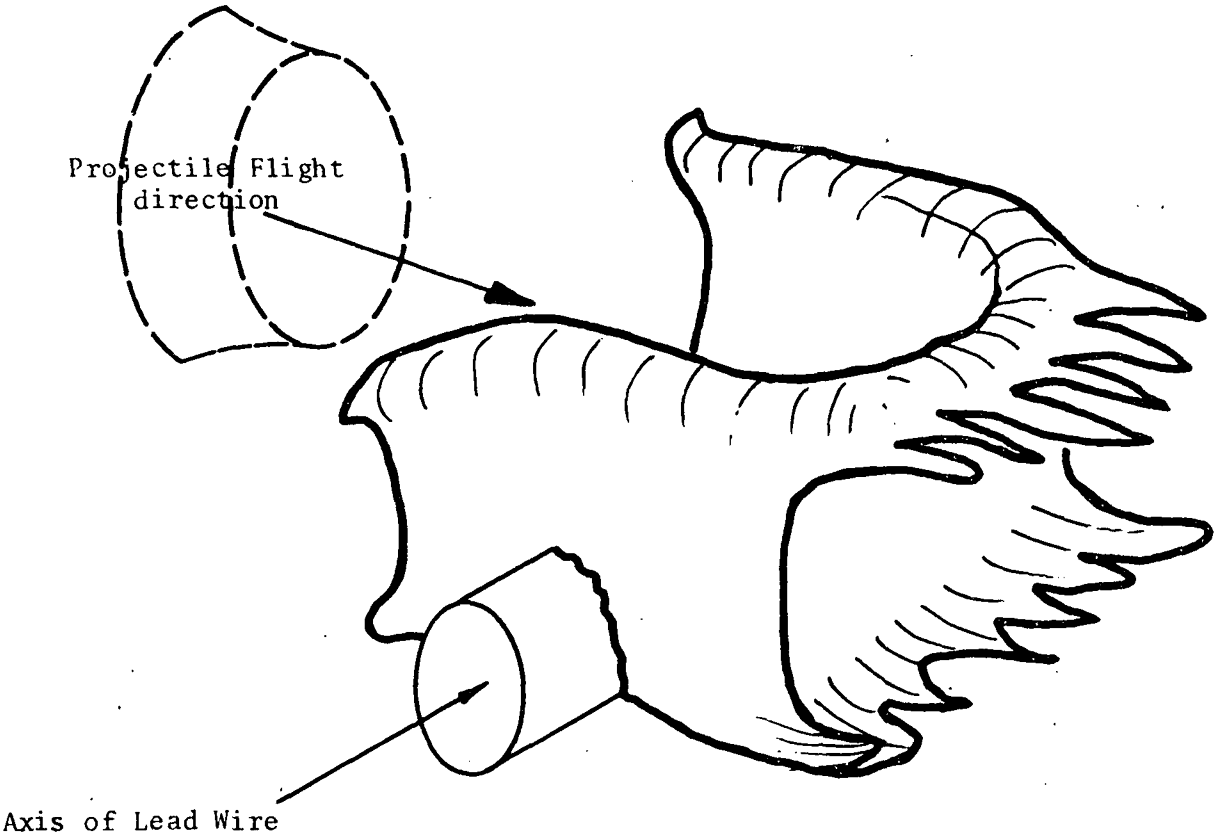

Figure 6.12 Sketch of Debris Cloud Constructed from Radiograms of figure 6.11.

In order to determine whether the form of the debris was due to the low impact velocity, we chose gun parameters suitable to an impact velocity of 8.5 km/sec (28,000 ft/sec). In figure 6.13 we show the radiograms of the impact of a single wire shortly after impact. The views are as in figure 6.11. The radiograms are very similar to these presented in figure 6.11 in which the impact velocity is considerably lower. As in figure 6.11(b), the view from above(figure 6.13(b)) appears to represent the debris cloud as being hollow.

Such a conclusion has been reached by Swift (reference 49). However, x-rays of a Lexan on Lexan impact failed to register any photographic impression of the cloud. It is likely, therefore, that the projectile has dispersed sufficiently to be completely transparent to the x-rays.

In figures 6.14(a) and 6.14(b) we have radiograms of an impact onto a pair of wires. The lines of sight are again as in figures 6.11(a) and 6.11(b). Figure 6.14(a) provides good substantiation of the jetting aspect of the proposed impact model. At the center of the photograph, we may see quite clearly the interacting jets. The center jet is evidently moving more rapidly than the peripheral jets as it has progressed further from the point of impact.

Figures 6.15(a) and 6.15(b) represent views along the axis of a pair of wires (0.32 cm (0.125 in) diameter spaced 0.51 cm (0.2 in) apart). The radiogram of 6.15(a) was taken 1.7 μsec after that in figure 6.15(b). Knowing the time between x-rays, one may measure the distance that the central jet has moved. The velocity determined in this manner is found to be ∿ 16.5 km/sec (54,000 ft/sec).

From figure 6.4 one finds that the axial escape velocity for an impact onto a Grid-Bumper at 8.5 km/sec (28,000 ft/sec) is given by 1.8 x 8.5 km/sec = 15.3 km/sec (50,300 ft/sec). The closeness of these two velocities tends to substantiate further the idea that jet-interaction is responsible for the high axial velocity associated with the Grid-Bumper.

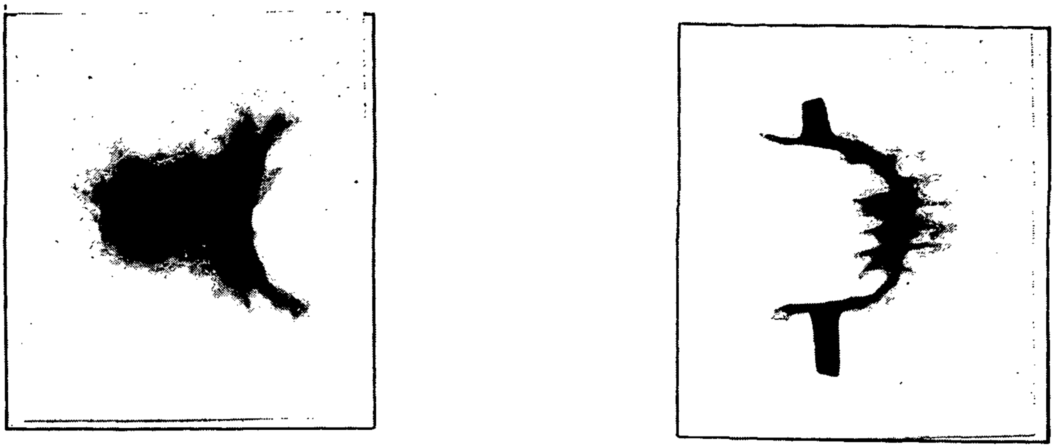

(a) (b)

Figure 6.13 Radiograms of impact of 1.27 cm (0.5 in) dia by 0.76 cm (0.3 in) long Lexan cylinder onto 0.32 cm (0.125 in) dia lead wire at 8.5 km/sec (28,000 ft/sec). Figure (a) is view along axis of wire. Figure (b) is view normal to wire axis and impact direction.

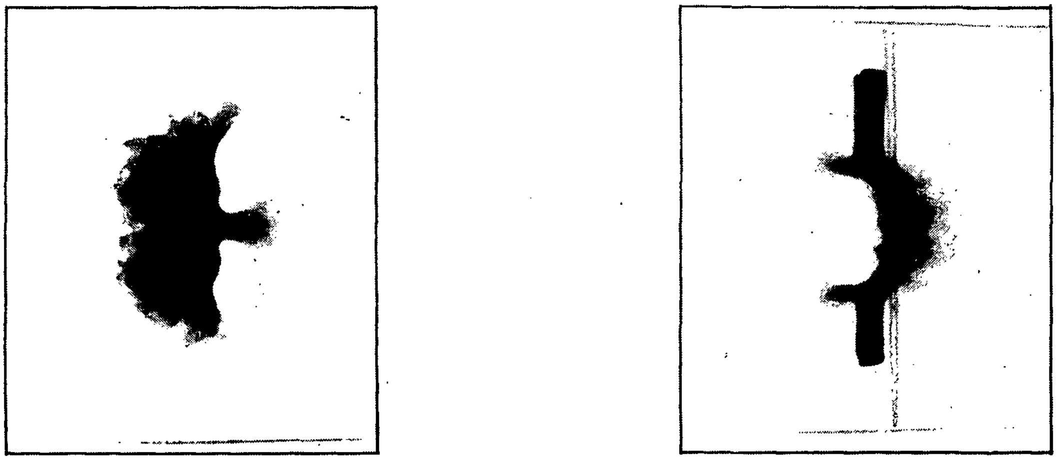

(a) (b)

Figure 6.14 Radiograms of impact of 1.27 cm (0.5 in) dia by 0.76 cm (0.3 in) long Lexan cylinder onto two 0.32 cm (0.125 in) dia lead wires spaced 0.51 cm (0.200 in) apart at 8.5 km/sec (28,000 ft/sec). Figure (a) is view along axis of wire. Figure (b) is view normal to wire axis and impact direction.

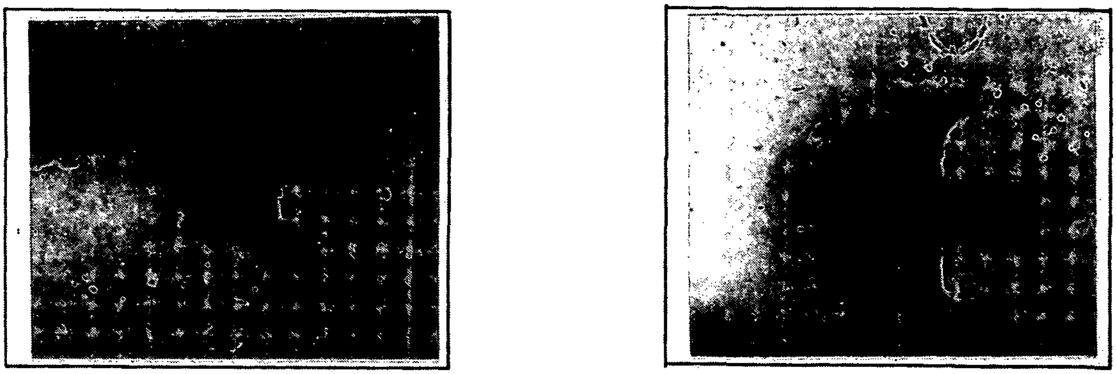

(a) (b)

Figure 6.15 Radiograms of impact of 1.27 cm (0.5 in) dia by 0.76 cm (0.3 in) long Lexan cylinder onto two 0.32 cm (0.125 in) dia lead wires spaced 0.51 cm (0.200 in) apart at 8.5 km/sec (28,000 ft/sec) both views along axis of wires.

7.0 CONCLUSIONS AND RECOMMENDATIONS

1. The Hugoniot for Lexan has been determined using Lexan targets instrumented with several shock wave sensors. The data indicate that it is not necessary to use very thin impact specimens as shock decay is not visible over a distance comparable to the diameter of the target. From the known Hugoniot for lead, we have determined the initial pressures created by the impact of Lexan projectiles onto lead shields.

2. Multigauge measurements of the pressure distribution imposed on a rigid witness plate by a debris cloud reveal that neither the peak pressure nor the total impulse are well described by a radial Gaussian dependence.

3. Beckman and Whitley photo-coverage of the response of witness sheets, whose thicknesses are close to the ballistic limit thickness, to the load imposed by a debris cloud indicate that the plate moves a distance of the order of its own thickness during the time in which the load is applied. For ductile specimens, however, this distance is small compared with the deflection to fracture. Fracture, when it occurred, occurred in a time comparable to the loading time. All the fractures observed involved a rupture at the center of the witness plate and were accompanied by petalling.

4. From ballistic limit tests, it appears that the ballistic limit thickness of a witness plate of a given material is proportional to the center line impulse due to the gaseous debris. This may be understood by balancing the mechanical energy loaded into the plate with the strain energy in plastic deformation.

5. Beckman and Whitley coverage of the response of a water backed main wall loaded by the debris cloud indicated that the displacements were too small to be detected. This was in qualitative agreement with the theoretical conclusion of reference 23. The support of the water permitted the ballistic limit thickness of the plate to be approximately half that of an unsupported wall, similarly loaded.

   Failure, when it occurred, occurred in the same manner as for unsupported plates. Fracture occurred at the center and petals were formed. In some tests, the plate was subsequently blown away from the water tank by the pressure wave in the water.

6. The resistance of SEMI and aluminized mylar cryogenic insulation panels to vaporous debris loading has been defined. Damage to the fragile panels was considerable at close spacings (∿15 cm (∿6 in) when the debris was formed by a Lexan cylinder 0.63 cm (0.25 in) in diameter). At approximately 20 cm (∿9 in), however, the damage reduced to tearing of the outermost one or two layers of the panel. This amount of damage was observed even at much larger spacings (∿60 cm) and was defined to be a nominal "no-damage" condition. Considerable numbers of pin holes were observed at all spacings due to the presence of particulate debris in the cloud. No definition was made of the hazard due to particulate debris.

7. From the determined resistance of the cryogenic insulation to vaporous debris, we have computed design data showing the required spacing of the panel from the shield versus mission area-time product for success

probabilities of 90%, 99% and 99.9%.

8. A theoretical calculation of the pressure behind the blast created in a body of water by the impact of projectile has been effected. Good agreement was obtained with an experimentally determined datum. The theoretical calculations have been compared with a body of data due to Stepka et al (reference 13). The agreement was found to be quite good at larger spacings.

9. An investigation of the debris cloud formed by the impact of a projectile onto a Grid-Bumper having the same mass per unit frontal area as a reference solid bumper has revealed that no significant difference in protection may be expected. Thus the interference of a meteoroid screen with the radiation balancing of a space vehicle can be reduced without sacrificing protection and with no additional weight penalty.

10. The differences between the debris clouds formed by solid shields and Grid-Bumpers are apparently attributable to the jetting of material through the apertures of the grid during the early stages of the impact.

11. Two areas of uncertainty in the Grid-Bumper involve the interaction with particles whose size is comparable to the aperture and the interaction with the radiation field. It is recommended that these areas be investigated.

12. There exists no quantitative understanding of the effects of particulate debris nor of the generation of such debris. Apart from the resolution of uncertainties in the extrapolation of data obtained

in the laboratory to meteoroid velocities, the question of particulate debris may be considered the area in greatest need of experimental and theoretical investigation in order that the meteoric risk to space vehicles be thoroughly understood.

REFERENCES

1. Whipple, F.L.
"Meteoritic Phenomena and Meteorites"
Physics and Medicine of the Upper Atmosphere
University of New Mexico Press
Albuquerque,1952, pp. 137-170

2. Friend, W.H., C.L. Murphy and I. Shanfield
"Review of Meteoroid-Bumper Interaction Studies at McGill University
NASA CR-54857, August 1966

3. Friend, W.H., C.L. Murphy and P.S. Gough
"Review of Meteoroid Bumper Interaction Studies at McGill University
NASA CR-54858, Sept. 1969

4. Al'tshuler, L.V., K.K. Krupnikov and M.I. Brazhnik
"Dynamic Compressibility of Metals Under Pressures from 400,000 to 4,000,000 Atmospheres"
JETP (U.S.S.R.) 34, 886-893, April 1958

5. Al'tshuler, L.V., K.K. Krupnikov, B.N. Ledenev, V.I. Zhuchikhin and M.I. Brazhnik
"Dynamic Compressibility and Equation of State of Iron Under High Pressures"
JETP (U.S.S.R.) 7, 606-614, 1958

6. McQueen, R.G. and S.P. Marsh
"Equation of State for Nineteen Metallic Elements from Shock-Wave Measurements to Two Megabars"
J. Appl. Phys. 31, 1253-1269, 1960

7. Walsh, J.M., M.H. Rice, R.G. McQueen and F.L. Yarger
"Shock Wave Compressions of Twenty-Seven Metals. Equations of State of Metals"
Phys. Rev. Vol. 108, 196-216, 1958

8. Walsh, J.M. and R.H. Christian
"Equation of State of Metals from Shock Wave Measurements"
Phys. Rev. Vol. 97, 1544-1556, 1955

9. Rice, M.H., R.G. McQueen and J.M. Walsh
"Compression of Solids by Strong Shock Waves"
Solid State Physics, Advances in Research and Applications,
Academic Press, 1958

10. Zel'dovitch, Ya.B.and Yu.P. Raizer
"Physics of Shock Waves and High Temperature Hydrodynamic Phenomena", Vol. II, Academic Press, 1967

REFERENCES CONT'D

11. Murphy, C.L.
"An Integral Model for the Similar Expansion of a Gas Cloud into a Vacuum"
NASA CR-54412, January 1966

12. Rae, William, J.
"Analytical Studies of Impact-Generated Shock Propagation - Survey and New Results"
Cornell Aeronautical Laboratory Inc.
CAL. No. AI-2456-A-1, June 1968

13. Stepka, F.S., C.R. Morse and Robert P. Dengler
"Investigation of Characteristics of Pressure Waves Generated in Water Filled Tanks Impacted by High-Velocity Projectiles"
NASA TND-3143, December 1965

14. Bull, G.V.
"On the Impact of Pellets with Thin Plates
McGill T.N. 1 - 10/61, October 1961

15. Mott-Smith, H.M.
"The Solution of the Boltzman Equation for a Shock Wave"
Phys. Rev. 82, 885-892, 1951

16. Becker, R.
"Stosswelle und Detonation"
Z. Physik 8, 321-362, 1922

17. Benedek, G.B.
"Deduction of the Volume Dependence of the Cohesive Energy of Solids from Shock Wave Compression Measurements"
Phys. Rev. Vol. 114, No. 2, April 1959

18. Courant, R. and K.O. Friedrichs
"Supersonic Flow and Shock Wave Theory"
Interscience, 1948

19. M. Van Thiel, Ed
"Compendium of Shock Wave Data", Vol. II, Lawrence Radiation Laboratory Report UCRL-50108, June 1966

20. Bradley, R.S.
"High Pressure Physics and Chemistry", Vol. II, Academic Press, New York

21. Kraak, G.W.
"Hugoniot Data for Lexan"
M. Sc. Thesis Dept. Mech. Eng. McGill University, April 1970

REFERENCES CONT'D

22. Heitler, W.
"Quantum Theory of Radiation"
Oxford University Press, 2nd Edition, 1947

23. Chou, Pei Chi and Paul Gordon
"Hypervelocity Impact of Bumper Protected Fuel Tanks"
AIAA Paper 69-369, May 1969

24. Weidman, Deene J.
"Response of a Plastic Circular Plate to a Distributed Time Varying Loading"
Ph.D. Thesis, Virginia Polytechnic Institute, June 1968

25. Becker, Karl R, R.W. Watson and Frank C. Gibson
"Hypervelocity Impact Phenomena"
Bur. Mines, U.S. Dept. Interior, April 5, 1962

26. Riney, T.D., and Heyda, J.F.
"Hypervelocity Impact Calculations and Their Correlation with Experiment"
Tech. Inform. Ser. No. R645D64 (Contract No. AF 08(635)-3781), Missile Space Division, Gen. Elec. Co., September 1964

27. Thompson, R.G.
"Plastic Behaviour of Circular Plates Under Transverse Impulse Loadings of Gaussian Distribution"
NASA TR-R-29, January 1968

28. Hill, R.
"Mathematical Theory of Plasticity"
Oxford, 1964

29. Green, S.J., Babcock, S.G. and R.D. Perkins
"Final Report - Fundamental Material Behaviour Study"
Technical Report TR67-07, Vol. 1, February 1967
Prepared by General Motors Corporation

30. Swift, H.F., Lt. J.M. Carson and A.K. Hopkins
"Ballistic Limits of 6061-T6 Aluminum Bumper Systems"
AFML-TR-67-324, October 1967

31. Alfaro-Bou, Emilio and Robert G. Thompson
"Ballistic Limit of Aluminum Plates Determined by an Exploding Foil Gun Technique"
NASA TND-4259, December 1967

32. Nysmith, C. Robert
"An Experimental Impact Investigation of Aluminum Double-Sheet Structures"
AIAA Paper 69-375, May 1969

REFERENCES CONT'D

33. Madden, Richard
"Ballistic Limit of Double-Walled Meteoroid Bumper Systems"
NASA TND - 3916, April 1967

34. McMillan, A.R.
"Experimental Investigations of Simulated Meteoroid Damage to
Various Spacecraft Structures", NASA CR-915, January 1968

35. Johnson, W.E.
"Oblique Impact Calculations Using a 3D Eulerian Code"
AIAA Paper 69-353, May 1969

36. "Meteoroid Environment Model 1969 Near Earth to Lunar Surface"
NASA SP8013
March 1969

37. Sedov, L.I.
"Similarity and Dimensional Methods in Mechanics"
Academic Press, 1959

38. Stanyukovitch, K.P.
"Unsteady Motion of Continuous Media"
Pergamon Press, 1960

39. Taylor, G.I.
"The Formation of a Blast Wave by a Very Intense Explosion"
Ministry of Home Security, R.C. 210 (II-5-153), 1941

40. Oshima, K.
"Quasi-Similar Solutions of Blast Waves"
Aeronautical Research Institute, University of Tokyo
Report No. 386, March 1964

41. Porzel, F.B.
"Height of Burst for Atomic Bombs, 1954. Part I, The Free Air Curve"
Los Alamos Scientific Laboratory Report LA-1664, May 1954

42. Zaker, T.A.
"Point Source Explosion in a Solid"
Armour Research Foundation, Illinois Institute of Technology
Report No. ARF 4132-6, November 1959

43. Bach, G.G. and Lee, J.H.
"Shock Propagation in Solid Media"
AIAA Paper No. 67-141, January 1967

REFERENCES CONT'D

44. Chou, Pei Chi, Robert R. Karpp and Lawrence J. Zajac
"Decay of Strong Plane Shocks in an Ideal Gas"
NASA CR-107, September 1964

45. Birkhoff, Garrett, Duncan P. MacDougall, Emerson, M. Pugh and Sir Geoffrey Taylor
"Explosives with Lined Cavities"
Journal of Applied Physics, Vol. 19, June 1948

46. Walsh, J.M., R.G. Shreffler and F.J. Willig
"Limiting Conditions for Jet Formation in High Velocity Collisions"
Journal of Applied Physics, Vol. 24, No. 1, March 1953

47. Jean, B. and T.L. Rollins
"Radiation from Hypervelocity Impact Generated Plasma"
AIAA Paper 69-364, May 1969

48. Rinehart, John S. and John Pearson
"Behaviour of Metals Under Impulsive Loads"
Dover Publications

49. Swift, H.F. and Capt. R.F. Prater
"Simulation of High Velocity Impacts on Thin Targets"
Technical Reports AFML-TR-68-88, May 1968

DISTRIBUTION LIST

Report Copies R D	Recipient
	National Aeronautics & Space Administration Lewis Research Center 21000 Brookpark Road Cleveland, Ohio 44135
1	Attn: Contracting Officer, MS 500-313
5	Liquid Rocket Technology Branch, MS 500-209
1	Techical Report Control Office, MS 5-5
1	Technology Utilization Office, MS 3-16
2	AFSC Liaison Office, 501-3
2	Library
1	Office of Reliability & Quality Assurance, MS 500-111
1	D.L. Nored, Chief, LRTB, MS 500-209
3	G.T. Smith Project Manager, MS 500-209
1	E.W. Conrad, MS 500-204
1	R.H. Kemp, MS 49-1
1	R.H. Knoll, MS 501-2
1	H.H. Vallentine, MS 501-2
2	Chief, Liquid Experimental Engineering, RPX Office of Advanced Research & Technology NASA Headquarters Washington, D.C. 20546
2	Chief, Liquid Propulsion Technology, RPL Office of Advanced Research & Technology NASA Headquarters Washington, D.C. 20546
1	Director, Launch Vehicles & Propulsion, SV Office of Space Science & Applications NASA Headquarters Washington, D.C. 20546
1	Chief, Environmental Factors & Aerodynamics Code RV-1 Office of Advanced Research & Technology NASA Headquarters Washington, D.C. 20546
1	Chief, Space Vehicles Structures Office of Advanced Research & Technology NASA Headquarters Washington, D.C. 20546

Report Copies		Recipient	Designee
R	D		
1		Director, Advanced Manned Missions, MT Office of Manned Space Flight NASA Headquarters Washington, D.C. 20546	
6		NASA Scientific & Technical Information Facility P.O. Box 33 College Park, Maryland 20740	
1		Director, Technology Utilization Division Office of Technology Utilization NASA Headquarters Washington, D.C. 20546	
1		National Aeronautics & Space Administration Ames Research Center Moffett Field, California 94035 Attn: Library	Hans M. Mark Mission Analysis Division
1		National Aeronautics & Space Administration Flight Research Center P.O. Box 273 Edwards, California 93523 Attn: Library	
1		National Aeronautics & Space Administration Goddard Space Flight Center Greenbelt, Maryland 20771 Attn: Library	Merland L. Moseson, Code 620
1		National Aeronautics & Space Administration John F. Kennedy Space Center Cocoa Beach, Florida 32931 Attn: Library	Dr. Kurt H. Debus
1		National Aeronautics & Space Administration Langley Research Center Langley Station Hampton, Virginia 23365 Attn: Library	E. Cortwright Director
1		National Aeronautics & Space Administration Manned Spacecraft Center Houston, Texas 77001 Attn: Library	J.G. Thiobodaux, Jr. Chief, Propulsion & Power Division
1		National Aeronautics & Space Administration George C. Marshall Space Flight Center Huntsville, Alabama 35812 Attn: Library	R.J. Nauman Hans G. Paul Leon J. Hastings James Thomas

Report Copies R D	Recipient	Designee
		Dale Burrows I.G. Yates Clyde Nevins J. Blumrich
1	Jet Propulsion Laboratory 4800 Oak Grove Drive Pasadena, California 91103 Attn: Library	Henry Burlage, Jr. Duane Dipprey John Howard
1	Defense Documentation Center Cameron Station Building 5 5010 Duke Street Alexandria, Virginia 22314 Attn: TISIA	
1	Office of the Director of Defense Research and Engineering Washington, D.C. 20301 Attn: Office of Asst. Dir. (Chem. Technology)	
1	RTD (RTNP) Bolling Air Force Base Washington, D.C. 20332	
1	Arnold Engineering Development Center Air Force Systems Command Tullahoma, Tennessee 37389 Attn: Library	Dr. H.K. Doetsch
1	Advanced Research Projects Agency Washington, D.C. 20525 Attn: Library	
1	Aeronautical Systems Division Air Force Systems Command Wright-Patterson Air Force Base Dayton, Ohio Attn: Library	S.L. Schmidt Code ARSCNC-2
1	Air Force Missile Test Center Patrick Air Force Base, Florida Attn: Library	L.J. Ullian
1	Air Force Systems Command Andrews Air Force Base Washington, D.C. 20332 Attn: Library	Capt. S.W. Bowen SCLT

Report Copies		Recipient	Designee
R	D		
1		Air Force Rocket Propulsion Laboratory (RPR) Edwards, California 93523 Attn: Library	
1		Air Force Rocket Propulsion Laboratory (RPM) Edwards, California 93523 Attn: Librart	
1		Air Force FTC (FTAT-2) Edwards Air Force Base, California 93523 Attn: Library	Donald Ross
1		Air Force Office of Scientific Research Washington, D.C. 20333 Attn: Library	SREP, Dr. J.F. Masi
1		Space & Missile Systems Organization Air Force Unit Post Officw Los Angeles, California 90045 Attn: Technical Data Center	
1		Office of Research Analyses (OAR) Holloman Air Force Base, New Mexico 88330 Attn: Library RRRD	
1		U.S. Air Force Washington, D.C. Attn: Library	Col. C.K. Stambaugh Code AFRST
1		Commanding Officer U.S. Army Research Office (Durham) Box CM, Duke Station Durham, North Carolina 27706 Attn: Library	
1		U.S. Army Missile Command Redstone Scientific Information Center Redstone Arsenal, Alabama 35808 Attn: Document Section	Dr. W. Wharton
1		Bureau of Naval Weapons Department of the Navy Washington, D.C. Attn: Library	J. Kay Code RTMS-41
1		Commander U.S. Naval Missile Center Point Mugu, California 93041 Attn: Technical Library	

Report Copies		Recipient	Designee
R	D		
1		Commander U.S. Naval Weapons Center China Lake, California 93557 Attn: Library	
1		Commanding Officer Naval Research Branch Office 1030 E. Green Street Pasadena, California 91101 Attn: Library	
1		Director (Code 6180) U.S. Naval Research Laboratory Washington, D.C. 20390 Attn: Library	H.W. Carhart J.M. Krafft
1		Picatinny Arsenal Dover, New Jersey 07801 Attn: Library	I. Forsten
1		Air Force Aero Propulsion Laboratory Research & Technology Divison Air Force Systems Command United States Air Force Wright-Patterson AFB, Ohio 45433 Attn: APRP (Library)	R. Quigley C.M. Donaldson
1		Electronics Division Aerojet-General Corporation P.O. Box 296 Azusa, California 91703 Attn: Library	W.L. Rogers
1		Space Division Aerojet-General Corporation 9200 East Flair Drive El Monte, California 91734 Attn: Library	S. Machiawski
1		Aerojet Ordnance and Manufacturing Aerojet-General Corporation 11711 South Woodruff Avenue Fullerton, California 90241 Attn: Library	
1		Aerojet Liquid Rocket Company P.O. Box 13222 Sacramento, California 95813 Attn: Technical Library 2484-2015A	R. Stiff

Report Copies		Recipient	Designee
R	D		
1		Aeronautronic Division of Philco Ford Corp. Ford Road Newport Beach, California 92663 Attn: Technical Information Department	Dr. L.H. Linder
1		Aerospace Corporation 2400 E. El Segundo Blvd. Los Angeles, California 90045 Attn: Library-Documents	J.G. Wilder V.C. Frost
1		Arthur D. Little, Inc. 20 Acorn Park Cambridge, Massachusetts 02140 Attn: Library	A.C. Tobey
1		Astropower Laboratory McDonnell-Douglas Aircraft Company 2121 Paularino Newport Beach, California 92163 Attn: Library	
1		ARO, Incorporated Arnold Engineering Development Center Arnold AF Station, Tennessee 37389 Attn: Library	
1		Beech Aircraft Corporation Boulder Facility Box 631 Boulder, Colorado Attn: Library	
1		Bell Aerosystems, Inc. Box 1 Buffalo, New York 14240 Attn: Library	T. Reinhardt W.M. Smith
1	1	Bendix Systems Division Bendix Corporation 3300 Plymouth Street Ann Arbor, Michigan Attn: Library	John M. Brueger
1		Bellcomm 955 L'Enfant Plaza, S.W. Washington, D.C. Attn: Library	H.S. London

Report Copies		Recipient	Designee
R	D		
1	1 1 1	Boeing Company Space Division P.O. Box 868 Seattle, Washington 98124 Attn: Library	J.D. Alexander C.F. Tiffany J.E. Erickson
1		Boeing Company 1625 K Street, N.W. Washington, D.C. 20006	
1		Boeing Company P.O. Box 1680 Huntsville, Alabama 35801	Ted Snow
1		Chemical Propulsion Information Agency Applied Physics Laboratory 8621 Georgia Avenue Silver Spring, Maryland 20910	Tom Reedy
1		Chrysler Corporation Missile Division P.O. Box 2628 Detroit, Michigan Attn: Library	John Gates
1		Chrysler Corporation Space Division P.O. Box 29200 New Orleans, Louisiana 70129 Attn: Librarian	
1		Cornell Aeronautical Laboratory, Inc. Buffalo, N.Y. Attn: W.J. Rae	
1		Curtiss-Wright Corporation Wright Aeronautical Division Woodridge, New Jersey Attn: Library	G. Kelley
1		University of Denver Denver Research Institute P.O. Box 10127 Denver, Colorado 80210 Attn: Security Office	
1		Fairchild Stratos Corporation Aircraft Missiles Division Hagerstown, Maryland Attn: Library	

Report Copies		Recipient	Designee
R	D		
1		Research Center Fairchild Hiller Corporation Germantown, Maryland Attn: Library	Ralph Hall
1		Republic Aviation Fairchild Hiller Corporation Farmington, Long Island New York	
1		General Dynamics/Convair P.O. Box 1128 San Diego, California 92112 Attn: Library	Frank Dore R. Tatro
1		Missiles and Space Systems Center General Electric Company Valley Forge Space Technology Center P.O. Box 8555 Philadelphia, Pa. 19101 Attn: Library	A. Cohen F. Schultz
1		Grumman Aircraft Engineering Corporation Bethpage, Long Island, New York Attn: Library	Joseph Gavin
1		Hercules Powder Company Allegheny Ballistics Laboratory P.O. Box 210 Cumberland, Maryland 21501 Attn: Library	
1		Honeywell Inc. Aerospace Division 2600 Ridgeway Road Minneapolis, Minnesota Attn: Library	
1		IIT Research Institute Technology Center Chicago, Illinois 60616 Attn: Library	C.K. Hersh
1		Ling-Temco-Vought Corporation P.O. Box 5907 Dallas, Texas 75222 Attn: Library	

Report Copies		Recipient	Designee
R	D		
1		Lockheed Missiles and Space Company P.O. Box 504 Sunnyvale, California 94087 Attn: Library	W.H. Sterbentz
1		Lockheed Propulsion Company P.O. Box 111 Redlands, California 92374 Attn: Library, Thackwell	H.L. Thackwell
1		Marquardt Corporation 16555 Saticov Street Box 2013 - South Annex Van Nuys, California 91409	L.R. Bell, Jr.
1		Martin-Marietta Corporation (Baltimore Division) Baltimore, Maryland 21203 Attn: Library	
1		Denver Division Martin-Marietta Corporation P.O. Box 179 Denver, Colorado 80201 Attn: Library	Dr. Morganthaler F.R. Schwartzberg
1		Orlando Division Martin-Marietta Corporation Box 5827 Orlando, Florida Attn: Library	J. Fern
1		Western Division McDonnell Douglas Astronautics 5301 Bolsa Avenue Huntington Beach, California 92647 Attn: Library	R.W. Hallet G.W. Burge P. Klevatt M. Scherb
1		McDonnell Douglas Aircraft Corporation P.O. Box 516 Lambert Field, Missouri 63166 Attn: Library	R.A. Herzmark
		Rocketdyne Division North American Rockwell Inc. 6633 Canoga Avenue Canoga Park, California 91304 Attn: Library, Department 596-306	Dr. R.J. Thompson S.F. Lacobellis

Report Copies			
R	D	Recipient	Designee
1		Space & Information Systems Division North American Rockwell 12214 Lakewood Blvd. Downey, California Attn: Library	
1		Northrop Space Laboratories 3401 West Broadway Hawthorne, California Attn: Library	Dr. W. Howard
1		Purdue University Lafayette, Indiana 47907 Attn: Library (Technical)	Dr. Bruce Reese
1		Radio Corporation of America Astro-Electronics Products Princeton, New Jersey Attn: Library	
1		Rocket Research Corporation Willow Road at 116th Street Redmond, Washington 98052 Attn: Library	F. McCullough, Jr.
1		Stanford Research Institute 333 Ravenswood Avenue Menlo Park, California 94025 Attn: Library	Dr. G. Marksman
1		Thiokol Chemical Corporation Redstone Division Huntsville, Alabama Attn: Library	John Goodloe
1		TRW Systems Inc. 1 Space Park Redondo Beach, California 90278 Attn: Tech. Lib. Doc. Acquisitions	D.H. Lee
1		TRW TAPCO Division 23555 Euclid Avenue Cleveland, Ohio 44117	P.T. Angell
1		United Aircraft Corporation Corporation Library 400 Main Street East Hartford, Connecticut 06108 Attn: Library	Dr. David Rix Erle Martin Frank Owen Wm. E. Taylor

Report Copies		Recipient	Designee
R	D		
1		United Aircraft Corporation Pratt & Whitney Division Florida Research & Development Center P.O. Box 2691 West Palm Beach, Florida 33402 Attn: Library	R.J. Coar Dr. Schmitke
1		United Aircraft Corporation United Technology Center P.O. Box 358 Sunnyvale, California 94038 Attn: Library	Dr. David Altman
1		Vickers Incorporated Box 302 Troy, Michigan	
1		Vought Astronautics Box 5907 Dallas, Texas Attn: Library	
1		University of Cincinnati Cincinnati, Ohio Attn: H.F. Swift	
1		Wright-Patterson Air Force Base, Ohio 45433 Attn: AFML (MAAE)	
1		Wright-Patterson Air Force Base, Ohio 45433 Attn: AFML (MAAM)	R.E. Headrick (Code MANE)
1		Commanding Officer Ballistic Research Laboratories Aberdeen Proving Ground, Maryland 21005 Attn: AMXBR-L	
1		Department of the Army U.S. Army Material Command Washington, D.C. 20315 Attn: AMCRD-RC	
1		Bureau of Naval Weapons Department of the Navy Washington, D.C. 20360 Attn: DLI-3	

Report Copies			
R	D	Recipient	Designee
1		Bureau of Naval Weapons Department of the Navy Washington, D.C. 20360 Attn: RMMP-2	
1		Bureau of Naval Weapons Department of the Navy Washington, D.C. 20360 Attn: RMMP-4	
1		Bureau of Naval Weapons Department of the Navy Washington, D.C. 20360 Attn: RRRE-6	
1		Commander U.S. Naval Ordnance Laboratory While Oak Silver Spring, Maryland 20910 Attn: Library	
1		Chemical Propulsion Information Agency Applied Physics Laboratory 8621 Georgia Avenue Silver Spring, Maryland 20910	
1		The Garrett Corporation 20545 Center Ridge Road Cleveland, Ohio, 44116	
1		Grumman Aircraft Engineering Corporation Bethpage Long Island, New York	
1		General Dynamics/Convair P.O. Box 1128 San Diego, California 92112 Attn: Library and Information Services (128-00)	
1		B.F. Goodrich Company Aerospace & Defense Products 500 South Main Street Akron, Ohio, 44311	
1		Goodyear Aerospace Corporation 1210 Massilon Road Akron, Ohio 44306	
1		Hamilton Standard Corporation Windsor Locks, Connecticut 06096 Attn: Library	

Report Copies		Recipient	Designee
R	D		
1		ABL, Division of Hercules Powder Company Cumberland, Maryland 21502 Attn: Thomas Bates	
1		IIT Research Institute Technology Center Chicago, Illinois 60616 Attn: C.K. Hersh, Chemistry Division	
1		Martin-Marietta Company Denver, Colorado 80201 Attn: A. Feldman	
1		North American Aviation, Inc. Space & Information Systems Division 12214 Lakewood Blvd. Downey, California 90242 Attn: Technical Information Center D/096-722 (A-J01)	
1		Hercules Powder Company Chemical Propulsion Division 910 Market Street Wilmington, Delaware 19804	
1		Narmco Research & Development Co. Whittaker Corporation 131 N. Ludlow Street Dayton, Ohio 45402	
1		Plastics Technical Evaluation Center Picatinny Arsenal Dover, New Jersey 07801	
1		Rohr Corporation Department 145 Chula Vista, California 91312	
1		Sandia Corporation Sandia Base Albuquerque, New Mexico 87115 Attn: H.E. Montgomery	
1		Thiokol Chemical Corporation Wasatch Division P.O. Box 524 Brigham City, Utah 84302 Attn: Library Section	

Report Copies R D	Recipient	Designee
1	U.S. Rubber Company Mishawaka, Indiana, 46544	
1	General Electric Company Apollo Support Department P.O. Box 2500 Daytona Beach, Florida 32015 Attn: C. Day	
1	Aerojet-General Corporation Park West Building - Suite 227 20545 Center Ridge Road Cleveland, Ohio 44116 Attn: W. Snapp	
1	Marine Engineering Laboratory NSRDC ANNADIC Annapolis, Maryland 21402 Attn: Karl H. Keller, Code 560	
1	Brunswick Corporation Defense Products Division P.O. Box 4594 43000 Industrial Avenue Lincoln, Nebraska 68504 Attn: J. Carter	
1	Celanese Corporation Box 1000 Summit, New Jersey 07901 Attn: J.D. Lassiter	
1	Superintendent U.S. Naval Postgraduate School Monterey, California 93900	
1	Commanding Officer U.S. Naval Weapons Laboratory Dahlgren, Virginia 22448 Attn: Technical Library	
1	E.I. duPont deNemours and Company Eastern Laboratory Gibbstown, New Jersey 08027 Attn: Library	

Report Copies		Recipient	Designee
R	D		
1		Esso Research and Engineering Company Special Projects Unit P.O. Box 8 Linder, New Jersey 07036 Attn: Library	D.L. Beader
1		Institute for Defense Analyses 400 Army-Navy Drive Arlington, Virginia 22202 Attn: Classified Library	
1		Minnesota Mining and Manufacturing Company 900 Bush Avenue St. Paul, Minnesota 55106 Attn: Library	H.C. Zeman
1		Thiokol Chemical Corporation Elkton Division Elkton, Maryland 21921 Attn: Librarian	
1		Thiokol Chemical Corporation Elkton Division Elkton, Maryland 21921 Attn: Librarian	
1		Thiokol Chemical Corporation Rocket Operations Center P.O. Box 1640 Ogden, Utah 84401 Attn: Librarian	
1		Thiokol Chemical Corporation Wasatch Division P.O. Box 524 Brigham City, Utah 84302 Attn: Library Section	
1		General Electric Company Apollo Support Department P.O. Box 2500 Daytona Beach, Florida 32015 Attn: Library	C. Day
1		FMC Corporation Chemical Research and Development Center P.O. Box 8 Princeton, New Jersey 08540 Attn: Security Officer	

Report Copies		Recipient	Designee
R	D		
1		Carnegie Institute of Technology Department of Civil Engineering Pittsburgh, Pennsylvania Attn: Library	R.B. Anderson
1		Westinghouse Research Laboratories Buelah Road, Churchill Boro Pittsburgh, Pennsylvania 15235 Attn: Library	G.O. Sankey J.H. Bitler
1		Cornell University Department of Materials,Science & Engineering Ithaca, New York 14850 Attn: Library	H.H. Johnson
1		Director Special Projects Office Department of the Navy Washington, D.C. 20360	
1		Goodyear Aerospace Corporation 1210 Massillon Road Akron, Ohio Attn: Library	Clem Shriver Dept. 481
1		Union Carbide Corporation Linde Division P.O. Box 44 Tonawanda, New York 14152 Attn: Library	
1		New York University University Heights New York, New York Attn: Library	P.F. Winternitz
1		General Dynamics P.O. Box 748 Fort Worth, Texas 76101 Attn: Library	D.E. Westerheide
1		Cryonetics Corporation Northwest Industrial Park Burlington, Mass. Attn: Library	J.F. Howlett
1		Institute of Aerospace Studies University of Toronto Toronto 5, Ontario Attn: Library	Dr. I.I. Glass

Report Copies		Recipient	Designee
R	D		
1		Commanding Officer U.S. Naval Underwater Ordnance Station Newport, Rhode Island 02844 Attn: Library	W.W. Bartlett
1		Sandia Corporation P.O. Box 969 Livermore, California 94550 Attn: Technical Library	H. Lucas
1		Sandia Corporation Sandia Base Albuquerque, New Mexico Attention: Library	John L. Lodman W. Herrmann W.K. Cox
1		Marino Engineering Laboratory NSRDC ANNADIC Annapolis, Maryland 21402 Attn: Library	Karl H. Keller Code 560
1		Brunswick Corporation Defense Products Division P.O. Box 4594 43000 Industrial Avenue Lincoln, Nebraska Attn: Library	J. Carter
1		Garrett Corporation Air Research Division Los Angeles, California Attn: Library	Linwood Wright
1		Brown University Providence, Rhode Island Attn: Technical Library	Dr. P.F. Maeder
1		Case Western Reserve University 100900 Euclid Avenue Cleveland, Ohio 44115 Attn: Technical Library	Dr. E. Rishatko
1		Pennsylvania State University State College, Pennsylvania Attn: Library	
1		Iowa State University Ames, Iowa Attn: Library	

Report Copies		Recipient	Designee
R	D		
1		California Institute of Technology Pasadena, California Attn: Library (Technical)	
1		Massachusetts Institute of Technology Cambridge, Mass. Attn: Library	
1		Hydronautics Incorporated Pindell School Road Laurel, Maryland	
1		Ford Motor Company American Road Dearborn, Michigan	M. Ference, Jr.
		Atomic Energy Commission Division of Reactor Development & Technology Washington, D.C. 20767	N. Grossman
		Naval Ship Research & Development Center Annapolis Division Annapolis, Maryland 21402	W.V. Smith
		Naval Ship Systems Command Washington, D.C. 20360	J.E. Dray (SNHIP 6148)
		U.S. Army Aviation Materials Lab Ft. Bustis, Virginia 23604	J.N. Danials SAVFE-AS
1		Battelle Memorial Institute Columbus Laboratories 505 King Avenue Columbus, Ohio 43201 Attn: Library	C.M. Allen
1		Franklin Institute Research Labs Benjamin Franklin Parkway Philadelphia, Pa. 19103 Attn: Library	
1		Mechanical Technology Incorporated 968 Albany-Shaker Blvd. Latham, New York 12110 Attn: Library	
		Industrial Tectonic Inc. 18301 Santa Fe Avenue Compton, California 90024	H. Hanau

Report Copies		Recipient	Designee
R	D		
1		National Science Foundation Engineering Division 1800 G. Street N.W. Washington, D.C. 20540 Attn: Library	
		Office of Naval Research Washington, D.C. 20360	
1		Sunstrand Denver 2480 West 70th Avenue Denver, Colorado 80221 Attn: Library	
1		Naval Ship Research and Development Center Code 526 Washington, D.C. 20007	Dr. W.B. Morgan
1	1	AEC-NASA Space Nuclear Propulsion Office, NPO NASA Headquarters Germantown, Maryland	F.C. Schwenk N.J. Gerstein